UNIVERSITY OF NAPLES FEDERICO II

Nanoparticle-Induced Morphologies in Multiphase Polymer Systems

Andrea Causa

PhD in *Materials and Structures Engineering* (XXVII Cycle)

Department of Chemical, Materials and Industrial Production Engineering

---

PhD Supervisor: Dr. Giovanni Filippone
PhD Coordinator: Prof. Giuseppe Mensitieri

April 2015

Abstract

Nanoparticle-Induced Morphologies in Multiphase Polymer Systems

Andrea Causa

Introducing nanoscale fillers into polymer matrices has recently emerged as a simple, cost-effective way to enhance the performances of the host materials. A mere capitalization of the filler properties to produce "nano-filled polymers", however, appears rather reductive. An undoubtedly more ambitious goal is the design of "genuine nanocomposites", based on a clever use of nanoparticles to impart new physical characteristics and behaviors that are absent in the unfilled matrix. In the present dissertation, the opportunity of pursuing such an approach to manipulate the phase-separated morphology of immiscible polymer blends is investigated from both a fundamental and a technological point of view.

Due to the thermodynamic immiscibility of most polymers, phase separation typically occurs in polymer blending processes, such as melt compounding and solvent casting. The resulting segregated morphologies are determined by the mutual interactions experienced by the different fluid and solid phases during processing. In the first part of the study, the physical mechanisms that govern the melt-state microstructural evolutions of polymer blends in the presence of nanoparticles are elucidated through the combination of viscoelastic measurements and morphological analyses. It is highlighted that, when the mobility of the nanoparticles is inhibited due to their anchoring at a polymer/polymer interface, the assembly of the filler is hindered until interface saturation happens. Above this threshold, the same dynamics as in monophasic melts are recovered. Even so, plate-like particles provided with sufficient bending stiffness are found to induce bulk morphological modifications without the need of interfacial jamming. Among others, the stabilization of irregularly-shaped polymer domains and clustering phenomena, which affect the phase inversion of the blend, have been observed.

The second part of the study is focused on the formation of films of semi-crystalline polymers through solvent casting. The precipitation and crystallization of the polymers and, eventually, the surface morphology and texture of the resulting flat systems are governed by a complex interplay among wetting, solvent evaporation and, in case of polymer blends, phase separation processes. In addition, all these phenomena are ultimately related to the interactions among the constituents of the starting polymer solution and the casting substrate. Incorporating nanoparticles to the pristine solution significantly affects the evolution of the polymer phases and the final blend morphology, the filler assembly dynamics being in turn influenced by the changing properties of the suspending medium during solvent evaporation. Nanoparticles can induce either a coarsening or a refinement of the phase domains, depending on their state of dispersion in the solution and the structures they form in the course of the casting process.

The acquired fundamental knowledge on the nanoparticle-induced morphological modifications in multiphase systems is ultimately capitalized for technologically relevant targets, such as the production of heat-resistant formulations based on recycled plastics and of biodegradable and biocompatible polymer films with prescribed topography and texture.

Contents

1 Introduction

This chapter outlines the research activity that is described in the present dissertation. After shedding light on the rationale and objectives of the work (§1.1), which is shaped around the possibility of using nano-sized particles to obtain multiphase materials with prescribed morphology and properties, the structure of the thesis is summarized (§1.2). The paper consists of two main parts, whose focuses reflect the double front of the performed investigations: bulk morphologies of melt-compounded systems and surface morphologies of solvent-cast films.

1.1 Motivation

The human endeavor to explore new materials has always been stimulated by the ambition to search for better performances and new functionalities. On the route toward the technological and industrial development, a fundamental scientific issue is represented by the assessment of the connections among the raw constituents, processing conditions and ultimate properties of a specific material. Indeed, the know-how acquirable by addressing such a question allows to overcome a restrictive trial-and-error approach, enabling the target-motivated design of products with desired characteristics [Wang and Pan, 2008].

In most of the engineering materials, the deliberate incorporation of additional components for performance improvement is commonplace; typical examples are metal alloys and fiber-reinforced composites. Such heterogeneous systems are widely used in several technological fields, but their behavior is quite challenging to be explained since the presence of additives (as well as of defects and contaminants inherently embedded in the material) has a relevant impact on the internal system structure. The latter, indeed, is strictly related to the interactions established among the various constituents once they are compounded. Furthermore, several properties may exhibit variations in correspondence of the interfacial regions, especially between constituents that are at different phase states. Some multiphase materials extensively used for technologically relevant purposes

are shown in Figure 1.1: (a) an open-cell foam, i.e. a two-phase system of solid and void that is widely employed in advanced aircraft design thanks to the combination of low density, high porosity and (for metal matrices) high thermal and electrical conductivity; (b) a fibrous solid/void system with the solid phase in a slender and oriented form, usually existing in biomaterials and fuel cells; (c) a functionally graded material with spatially varied phase microstructure, used in aerospace, electronics and energy storage applications.

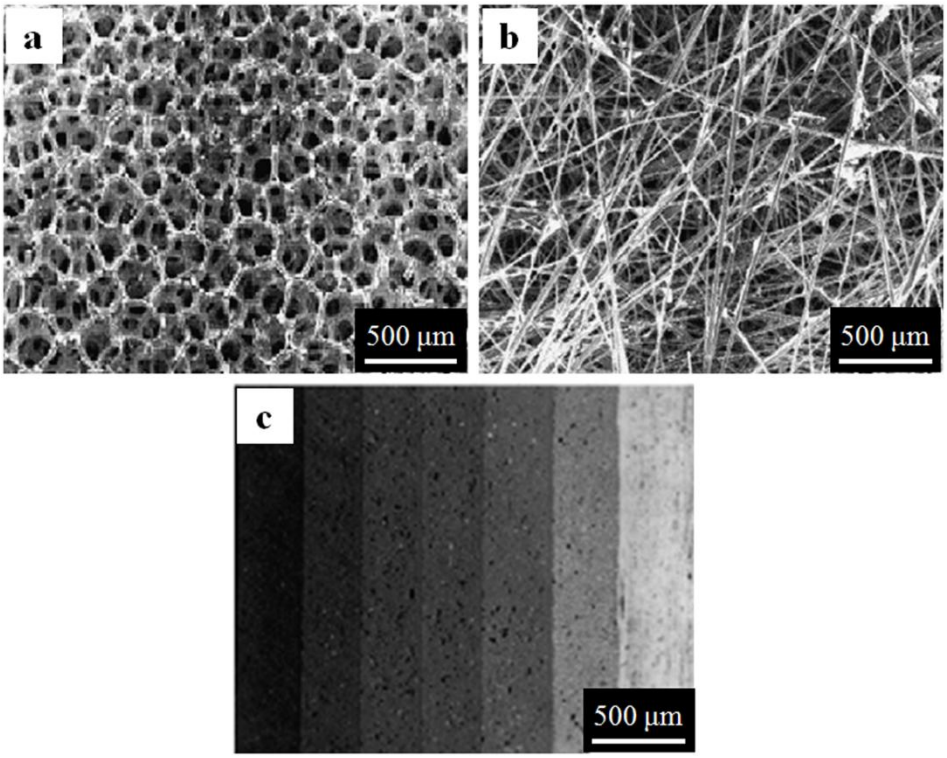

Figure 1.1 – A variety of multiphase structures: (a) an open-cell foam; (b) a fibrous layer in a fuel cell; (c) a cross section of a graded material. Reprinted from [Wang and Pan, 2008], copyright 2008, with permission from Elsevier.

Concerning plastic materials, most current applications require specific combinations of properties that cannot be provided by a single homopolymer. Hence, different approaches based on the combination of two or more phases have been pursued aiming to produce polymer-based materials with tailored characteristics. A cost-effective, traditionally employed route consists in physically

blending immiscible polymers by mixing the constituents in the melt state or dissolving them in a common solvent, which is then removed in order to induce phase precipitation [Utracki and Shi, 1998]. Melt compounding is conducted in mixers or extruders to produce multiphase materials with desired transport, optical, mechanical and thermal bulk properties. on the other hand, solvent casting is extensively performed to produce polymer blend films, whose main technological applications (electronics, optics, photovoltaics, biotechnology) require well-defined surface structure and topography [Xue et al., 2012]. In both cases, however, the thermodynamic immiscibility (due to the low mixing entropy) of most polymer pairs results in phase-separated morphologies which are determined not only by the amount and characteristics of the single components, but also by the processing history they experience. Hereinafter, unless otherwise specified, the phrase "multiphase polymer systems" will be used with unique reference to immiscible polymer blends.

Another well-established approach to improve the performances of polymer systems is the introduction of inorganic fillers into polymer matrices. In particular, nano-sized particles offer a series of advantages in comparison with conventional macro- or microscopic fillers: high specific surface area ($\sim 10^6$ cm^2 g^{-1}), high numerical density ($\sim 10^{20}$ cm^{-3}), low filler contents required for connectivity through the sample, small interparticle distances (often comparable with the size of polymer chains) and relevant mobility in the suspending medium [Romeo et al., 2009]. Furthermore, the use of nanoparticles appears particularly attractive as it is not system-specific and does not imply any alteration of the traditional melt- and solution-mixing technologies. Up to now, most of the research efforts, and almost all of the commercial examples, of polymer-based nanocomposites have revolved around incorporating nanoscale fillers to polymer matrices and merely capitalizing on the filler properties to enhance the performances of the final material [Manias, 2007]. Despite the existence of many examples of such high-performance "nano-filled polymers", when dealing with nanoparticles one should be more ambitious, aspiring to provide new physical properties and novel behaviors that are absent in the unfilled matrix. When the latter exhibits phase-separated morphology, a series of intriguing opportunities emerge to design "genuine nanocomposites" by coupling the previously described approaches for phase combination and exploiting the advantages offered by each technique. Preferential reinforcement of one phase or targeted reinforcement of the interphase, filler-induced changes in phase morphology or phase alignment, filler-induced compatibilization of immiscible phases, and changes of thermo-mechanical transitions, are only few of the

opportunities offered by a clever use of nanoparticles [Koerner et al., 2004; Bockstaller et al., 2005; Kim et al., 2006]. Figure 1.2 reports various multiphase polymer systems where a preferential positioning of the filler in a certain region (one of the phases or the interface) is promoted by a pronounced chemical affinity to one of the constituents and/or appropriate processing conditions.

The increasing interest in nanocomposites based on multiphase systems is testified by a number of publications growing five times than about single-phase nanocomposites (according to Scopus.com). An intensive research activity exists on the use of nanoparticles to manipulate the morphology of non-polymeric multiphase mediums; meaningful examples of such "soft matter" systems are low molecular weight emulsions, suspensions and foams [Clegg, 2008]. Besides understanding how to use nanofillers to guide the material morphology, many researchers are interested in the other side of the coin, i.e. how to use immiscible phases as a liquid template through which controlling the space arrangement of the nanoparticles, eventually realizing advanced nanostructures. Since these two mechanisms are closely related, elucidating how the motion of the particles influences the behavior of the fluid phases and, at the same time, how the structural evolutions of the latter in turn affect the space arrangement of the filler is an extremely delicate issue to be addressed in order to produce tailor-made materials. The need for such a fundamental understanding is particularly perceived in the field of polymer blends: for these systems, nanoparticle-induced morphological modifications have been widely reported, but most of the proposed explanations for the underlying physical mechanisms result conflicting or, at least, applicable only to the specific system considered.

The research activity reported in this thesis perfectly fits in the scenario described so far, being focused on a pondered and targeted use of nanoparticles as clever means to manipulate the morphology (as well as the final properties) of multiphase polymer systems prepared by both melt- and solution-mixing routes. The adopted methodology consists of the following main steps: (*i*) assessing the mutual chemical/physical interactions among the different phases during processing; (*ii*) elucidating how these interactions determine the morphological evolution of the system and its final structure; (*iii*) exploiting the acquired know-how to propose viable routes for the fulfillment of technological targets. Shedding light on the complex phenomena which eventually determine the morphology of multiphase systems at different length scales, the ultimate aim of this work is to understand how to govern material- and process-related parameters to produce "genuine nanocomposites" with prescribed structure and properties.

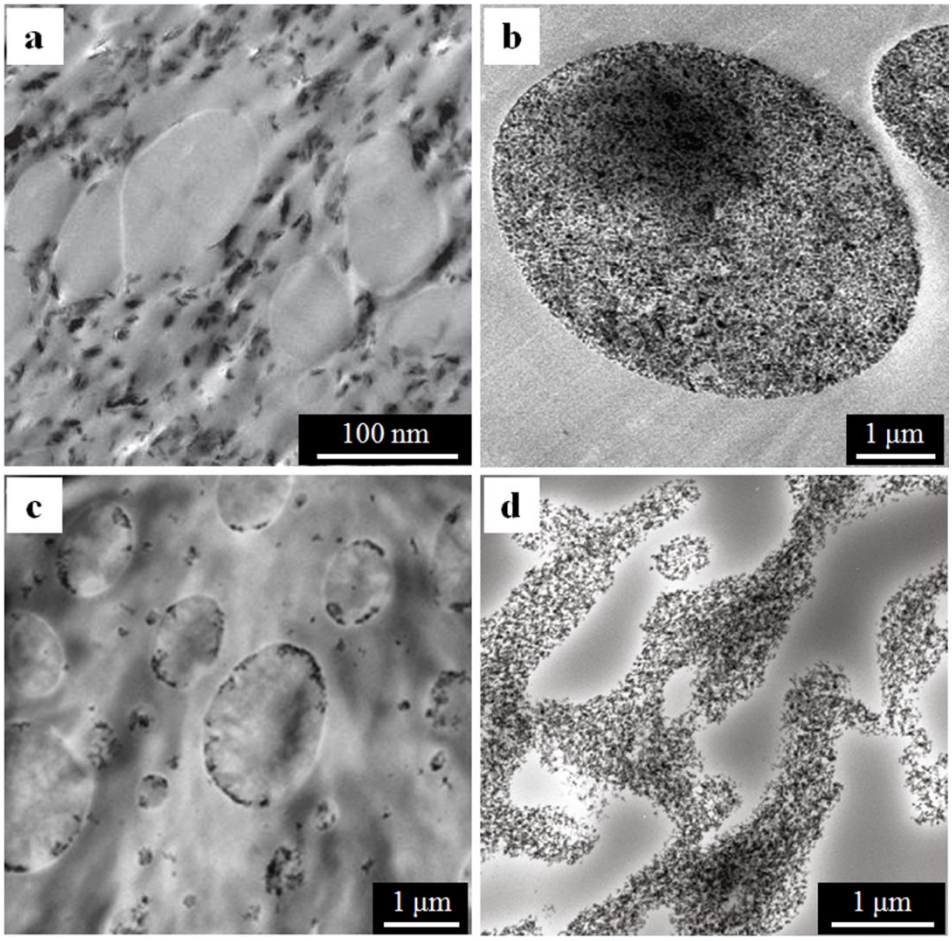

Figure 1.2 – A variety of multiphase polymer systems with selectively positioned nanoparticles. (a) Polyethylene terephtalate/polycarbonate (PET/PC) blend with layered silicates located in the PET matrix. Adapted with permission from [Kim et al., 2006], copyright 2006, American Chemical Society. (b) Polystyrene/polyamide 6 (PS/PA6) blend with titania particles located in the PA6 domains. Adapted with permission from [Cai et al., 2012], copyright 2012, Elsevier. (c) Polypropylene/poly(ethylene-vinyl acetate) (PP/EVA) blend with silica particles positioned at the polymer/polymer interface. Reproduced from [Elias et al., 2008], copyright 2008, with permission from John Wiley and Sons. (d) PS and poly(vinyl methyl ether) (PVME) blend with rod-like particles located in PVME. Adapted with permission from [Li et al., 2011], copyright 2011, American Chemical Society.

1.2 Thesis organization

The present work consists of two main parts that reflect the double track on which the research activity has been carried out. In both sections, an exhaustive overview of the state-of-the-art is provided at the beginning, then the results of the performed investigations are presented and discussed.

Part I is centered on melt-compounded multiphase polymer systems. Chapter 2 provides a background for the following issues that concern immiscible polymer blends: mechanisms of microstructural evolution; uneven nanoparticle distribution in the fluid phases and promotion of morphological modifications; relationships between nanoparticle-induced morphologies and technological properties. The similarities and differences of immiscible polymer blends with other multiphase fluid emulsions, such as low-viscosity emulsions, are also pointed out. Chapter 3 reports the outcomes of a fundamental study aimed to understand the mutual interactions between solid and fluid components in nanoparticle-filled polymer blends. Specifically, the effect of hindering the filler mobility on the development of the blend morphology is assessed. Notable attempts to capitalize such fundamental understanding for practical purposes are presented in Chapter 4, where it is shown that the use of nanoparticles to control the morphology of blends of recycled plastics can be beneficial for improving the low performances of these materials.

Solvent-cast polymer systems and their surface features are the subject matter of Part II. The literature review provided in Chapter 5 is structured as follows. First, the common techniques for polymer film production are described, highlighting the main phenomenological aspects and influential factors. After discussing the phase separation process in the presence of two or more polymers in the initial solution, the impact of nanoparticle addition on the final surface morphology and topography is pointed out. Chapter 6 reports the investigation conducted on semi-crystalline, biodegradable polymer films prepared through drop casting. The mechanism of formation and the final morphological and textural features have been preliminary studied for homopolymer-based films, aiming to assess the influence of material- and process-related parameters, and afterwards on blends at different polymer composition and kind of filler.

Concerning the final part of the thesis, in Chapter 7 a promising, alternative route to manipulate the morphology of multiphase polymer materials is briefly presented. Specifically, the potential of supercritical fluids to assist the precipitation process of polymers and drive the structure of the final materials is

highlighted showing preliminary results of currently underway investigations. Ultimately, Chapter 8 is dedicated to report the principal conclusions of the whole research activity.

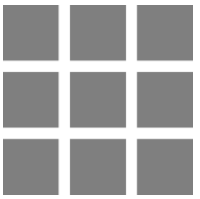

PART

I

Bulk morphologies in melt-compounded systems

2

Morphologies of multiphase polymer systems – Literature review

When two or more immiscible liquids are blended, the resulting morphology, i.e. the small-scale arrangement assumed by the different phases, is mainly dictated by the properties of the constituents and the processing history and, in turn, is crucial in determining the performances of the final material. The recent scientific literature, along the lines of pioneering studies on low molecular weight fluids, suggests the possibility of controlling the morphology of melt-blended multiphase polymer systems by filling them with solid fillers. In this chapter, after reviewing the phenomena whose occurrence and interplay determine the microstructural evolution in polymer blends (§2.1), light is specifically shed on the morphological modifications induced by nano-sized particles in these systems. The uneven spatial distribution of the filler, which tends to enrich specific regions of the blend (§2.2), is a factor commonly invoked to explain the various effects observed (and discussed in §2.3). Ultimately, meaningful examples are provided to elucidate the link between morphology and macroscopic properties of nanoparticle-containing multiphase polymer systems (§2.4).

2.1 Morphological evolution in immiscible polymer blends

Due to the generally low mixing entropy of macromolecular materials, most polymer pairs are thermodynamically immiscible. As a consequence, phase separation phenomena typically occur during the melt-blending process. The morphology development of multiphase polymer systems has been a matter of intensive investigations for more than three decades. There is now a fairly comprehensive understanding of the effect of material- and process-related parameters (blend composition, viscosity of the constituents, flow conditions) on the microstructural evolutions of these systems, as well as the corresponding structure-property relationships. A brief yet comprehensive overview of this

research, extensively collected in the literature, is presented hereinafter [Utracki and Shi, 1992; Tucker and Moldenaers, 2002].

In quiescent conditions, the factors that determine the morphology of a polymer blend are the volume fraction and viscosity of the different components. In a binary blend, immiscibility results in either dispersed or co-continuous morphologies. In the former, one of the phases is continuous and encompasses dispersed spheroidal inclusions of the other constituent; the latter, on the other hand, are obtained for intermediate compositions and are characterized by the mutual interpenetration of the phases. Complete co-continuity occurs around the so-called phase inversion point, where the original dispersed phase becomes continuous and, conversely, the original matrix turns itself into the dispersed phase. Concerning the effect of viscosity, Willemse and co-workers have highlighted that the volume fraction of minor component corresponding to the transition from dispersed to co-continuous morphology decreases as the ratio p between the viscosities of the minor and major phase, η_d and η_m respectively, decreases [Willemse et al., 1999]. This remark is in agreement with the predictions of the following semi-empirical rheological model developed by Jordhamo and co-workers

$$\frac{\eta_d}{\eta_m} \cong \frac{\phi_d}{\phi_m} \tag{2.1}$$

according to which co-continuity arises when p equals the ratio between the volume fractions of the minor and major phase, i.e. ϕ_d and ϕ_m [Jordhamo et al., 1986]. In particular, for $p \approx 1$, phase inversion occurs when the volume fraction of both the phases is 0.5.

In flow conditions, the morphological evolution of multiphase polymer systems derives from the interplay of melt-state modifications experienced by the different phases. These phenomena, basically consisting in domain breakup, coalescence and relaxation, are in turn influenced not only by the properties of the individual components, but also by their interactions and the imposed deformation rate. In dispersed morphologies, the minor phase may be present not only in the form of drops, but also of fibrils or lamellae. Concerning co-continuous morphologies, Miles and Zurek have extended the relationship between viscosity ratio and phase inversion composition expressed by Equation 2.1 to the dynamic case, implementing the model with the dependence of the viscosity of the polymers on the shear rate [Miles and Zurek, 1988]. A significant contribution to the understanding of the aforementioned mechanisms ensues from studies performed

on emulsions of Newtonian fluids [Taylor, 1932]. For polymer blends, indeed, the underlying physics is basically the same, in spite of the larger width of polymer/polymer interfaces compared with those between low molecular weight fluids [Ajji and Utracki, 1996; Jones, 1997].

In systems with dispersed morphology, the drops of the minor phase may deform, orient, and possibly break up under flow. Their response is determined by the viscosity ratio, the flow conditions (shear or elongation) and the balance between viscous stresses, which tend to deform the drops, and interfacial tension, which drives the drops to retract back to a spherical shape. The relative importance of the latter parameters is expressed by the capillary number:

$$Ca = \frac{\eta_m \dot{\gamma} R}{\alpha} \tag{2.2}$$

where η_m is the viscosity of the matrix, $\dot{\gamma}$ the deformation rate, R the radius of the drops of dispersed phase and α the interfacial tension. Ca also expresses the ratio between the interface relaxation time ($\eta_m R/\alpha$) and a characteristic time for flow-induced deformation (the inverse of the shear rate). For capillary numbers lower than a critical value, the drops attain a steady shape and orientation, the deformation being exclusively induced by the flow. Conversely, above the critical capillary number the drops eventually break up due to the prevalence of viscous stresses over the interfacial tension. The critical capillary number for Newtonian droplets has been measured as a function of p by Grace in both simple shear and planar elongation, by gradually increasing the deformation rate until breakup [Grace, 1982]. In simple shear flow, no breakup is found when $p > 4$ due to the high viscosity of the dispersed phase; an elongational flow can instead break up droplets of any viscosity ratio. Data for intermediate flows have been provided by Bentley and Leal [Bentley and Leal, 1986]. Briefly commenting on the droplet breakup mechanisms, for $Ca \ll 1$, the steady drop shape is slightly ellipsoidal, its long axis being oriented at 45° to the flow; with increasing Ca, the viscous effect also increases and the drop axis shifts toward the flow direction. When Ca is slightly greater than the critical value, the breakup mode depends on p: small droplets can be released from the end of a sigmoidal drop, or alternatively the central part of the drop can gradually neck up, giving rise to the breakup into two "daughter" drops and smaller satellite droplets. When Ca is well above the critical value, the drop stretches into a slender fibril, which subsequently breaks up by a capillary-wave Rayleigh instability. For a gradual increase of the shear rate, a

series of breakup steps takes place, bringing about the formation of smaller and smaller droplets. On the other hand, breakup for a sudden shear rate increase is a single event that causes the formation of daughter drops characterized by low values of *Ca*, hence remaining nearly spherical. The capillary number being equal, a viscoelastic drop can stretch more than a Newtonian one, hence the timescales for its breakup are much longer; for small deformations, however, the treatise described so far can be reasonably extended to non-Newtonian fluids.

When a multiphase fluid system with drop-matrix morphology is sheared at a low capillary number, the characteristic size of dispersed phase may increase due to coalescence phenomena that follow the collision of drops coming into contact. Differently from breakup, coalescence may also take place after flow cessation, due to the approaching of deformed drops that are recovering their spherical shape. After colliding, the drops develop a flat or dimpled interface over which they are separated by a thin film of matrix fluid. Hydrodynamic forces push the drops together during some finite interaction time, and the film thins due to the drainage of matrix fluid. If the film thickness falls below a critical value, estimated to be approximately 10 nm for polymer blends, then van der Waals forces become relevant, the film ruptures, and the droplets coalesce [Chesters, 1991]. Alternately, the hydrodynamic forces may reverse before the film ruptures, so that the droplets separate without coalescing. The efficiency with which the collisions result in coalescence depends on how effectively the matrix layer is drained from between the droplets. Film drainage has been modeled through various assumptions: (i) a partially mobile interface, appropriate if p is close to 1 and the main resistance to film drainage comes from viscous stresses within the droplet; (ii) a fully mobile interface, if $p << 1$ and the dispersed fluid phase provides no resistance to drainage; (iii) an immobile interface, suitable in the case of $p >> 1$ and absence of interfacial deformation in response to shear stresses in the film. Each drainage model gives a different dependence of the coalescence-limited drop size on shear rate. In any case, the growth of drop size due to coalescence (estimable through scaling relationships not discussed here) is determined by factors such as the frequency of collisions, the interaction time, and the hydrodynamic forces, which in turn depend on the volume fraction of the dispersed phase, the flow rate and the rheological and interfacial properties of the constituents. Larger drops are less likely to coalesce than smaller ones because they flatten more easily and it is more difficult to drain the matrix fluid from the film.

The dynamic interplay of breakup and coalescence phenomena is mainly governed by phase concentrations, interfacial tension and shear rate, and

determines the so-called morphological hysteresis. The minimum drop size for breakup and the maximum drop size for coalescence coincide at a critical shear rate. Above this value, the steady-state drop size is determined by a competition between breakup and coalescence and is a unique function of shear rate. Below the critical shear rate, instead, there exists a range of drop diameters that are too small to break up but are also too large to coalesce in a reasonable time.

After the cessation of the flow, further morphological evolutions ensue from the competition of two processes driven by interfacial tension: the relaxation of the deformed drops, which are not stable and tend to retract back to a spherical shape, and the formation of capillary waves that cause the breakup of large drops. The two phenomena prevails at low and high values of the drop aspect ratio, respectively. This means that slightly deformed droplets will retract back to a spherical shape, very elongated droplets will relax into a string of droplets via capillary wave instabilities, whereas droplets with intermediate aspect ratio will undergo end-pinching: the drop forms bulbous ends which pinch off into separate drops. If the drop is long enough, bulbs form again on the new ends, and the process is repeated until the remaining portion of the drop is small enough to retract back to a sphere.

The morphology of multiphase polymer materials directly reflects itself on the linear viscoelastic response of the systems, characterized by the combination of the inherent viscoelasticity of the polymeric constituents and the features of the polymer/polymer interfaces. The tendency of the latter to relax under the interfacial tension, bringing the drops back to their spherical shape, determines an excess elasticity evidenced by an increase of the elastic shear modulus G' at low frequencies; conversely, the viscous modulus G'' is not show significantly affected by the presence of the drops. If the characteristic relaxation times of the drops (typically on the order of seconds) is longer than the elastic relaxation time of the polymers, the contribution of the drops is revealed by a “shoulder” in the curve of G' versus ω, which shifts to higher frequencies with decreasing the drop size. The excess elasticity is less evident for co-continuous morphologies, G' exhibiting a power law behaviour at low frequencies; this is ascribed to the high interconnection between the phases of the systems and the consequent resistance to flow [Steinmann et al., 2002]. The linear viscoelastic moduli of a polymer blend with drop-matrix morphology can be predicted by the Palierne model (which is an extension of the theory by Oldroyd on Newtonian multiphase systems) once the interfacial tension and the drop size distribution are known [Oldroyd, 1953; Palierne, 1990; Graebling and Muller, 1990]. If the polydispersity (ratio between

volume-average and number-average drop radii) is lower than 2, the volume-average drop radius can be reasonably used in place of the drop size distribution.

To sum up, the morphology of a multiphase polymer system arises through the interplay of the deformations due to flow, retraction, coalescence and breakup phenomena, some of which are illustrated in Figure 2.1. Although the amounts and

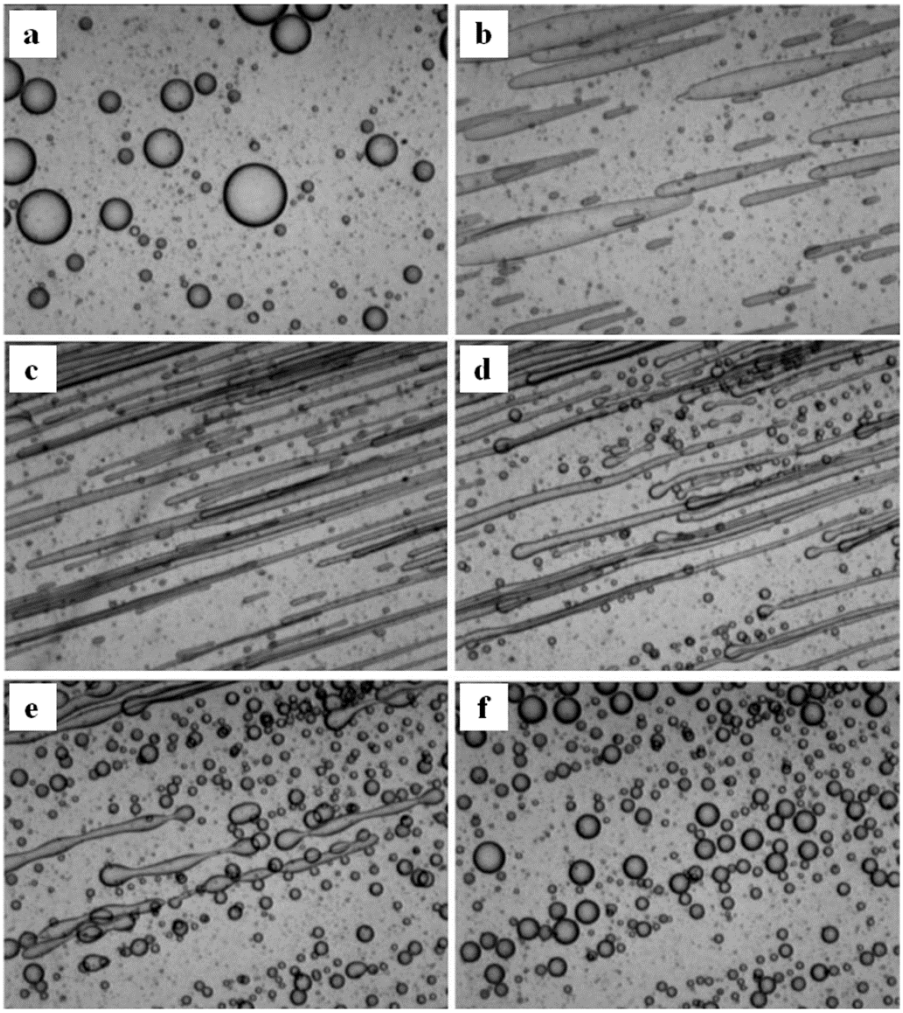

Figure 2.1 – Micrographs of a model polymer blend with initial drop-matrix morphology (a). Upon shearing, the drops stretch in the shear direction (b, c); after flow cessation, the elongated domains retract and slowly breakup (d, e). The structure resulting from such flow history is finer than the original one (f). Adapted from [Tucker and Moldenaers 2002], copyright 2002, with permission from Annual Reviews.

properties of the constituent play an important role in its determination, morphology is controlled by the deformation history and is not an intrinsic property of a blend. When solid fillers are incorporated, further complications emerge due to the varied interphase interactions, as discussed in the following sections.

2.2 Nanoparticles in immiscible polymer blends: prefatory considerations

The incorporation of fine solid particles in multiphase fluids is an expedient become popular at the beginning of last century, thanks to the discovery of the ability of colloidal particles to stabilize low-viscosity emulsions [Ramsden, 1903; Pickering, 1908]. This effect has been ascribed to the filler aptitude to self-assemble at the fluid-fluid interface and inhibit the coalescence of the drops of the minor phase. Thenceforth, intensive investigations have been conducted on both low and high molecular weight systems, such as suspensions, foams and immiscible polymer blends, containing particles that differ among them in size (from micro- to nanometric), shape (spheres, platelets, rods) and surface chemistry [Aveyard et al., 2003; Clegg, 2008]. These aspects influence the distribution of the filler in one of the fluid phases or at the interface between them and, ultimately, the morphology and properties of the final system [Fenouillot et al. 2009; Taguet et al. 2014]. Hereinafter, the issue of assessing the localization of solid fillers in multiphase polymer systems is addressed, so to provide the basis for discussing the particle-induced morphological modifications and their underlying mechanisms.

2.2.1 Uneven localization of nanoparticles: thermodynamic predictions

The localization of solid particles in a blend of immiscible liquids can be predicted by estimating the interactions among the different components. The interfacial energies are used to express the wettability parameter according to Young's equation:

$$\omega_{12} = \cos\theta = \frac{\gamma_{S2} - \gamma_{S1}}{\gamma_{12}} \tag{2.3}$$

where θ is the contact angle (defined as shown in Figure 2.2), γ_{12}, γ_{S1} and γ_{S2} are the interfacial tensions between the liquids 1 and 2, the particle and the liquid 1, and the particle and liquid 2 respectively. If $\omega_{12} > 1$ or $\omega_{12} < -1$, the particles are

present only in liquid 1 or liquid 2, respectively. Conversely, if $|\omega_{12}| < 1$ (correspondingly, $0 < \theta < 180°$), the particles accumulate at the liquid-liquid interface [Sumita et al., 1991]. The link between particle localization and polarity has been highlighted by Binks focusing on water-oil systems [Binks, 2002]. If the filler is hydrophilic, θ is lower than 90° and the accumulation of particles at the interface promotes an oil-in-water emulsion. Conversely, if the filler is hydrophobic, θ is comprised between 90° and 180° and a water-in-oil emulsion forms. The condition $\theta = 90°$ corresponds to the maximum interfacial adsorption of the particles or, alternatively, to the maximum free energy required to remove the fillers from the fluid-fluid interface. Marked hydrophilicity or hydrophobicity (i.e. θ far from 90°) respectively imply a preferential localization of the filler in the water or in the oil phase.

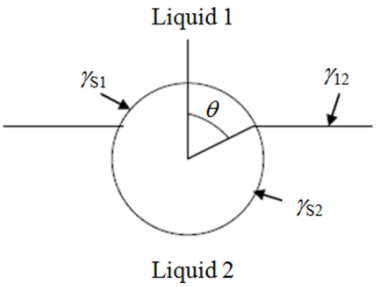

Figure 2.2 – Schematic representation of a spherical particle at the interface between liquids 1 and 2.

The wetting parameter can be also used to predict particle distribution in polymer blends, in spite of the higher viscosity and lower interfacial tensions exhibited in comparison with liquid emulsions. The polymer/polymer and polymer/particle interfacial tensions are usually estimated from experimental values of the surface energies of the single constituents, using the theoretical models expressed by the following harmonic-mean [Wu, 1987] and geometric-mean equations [Owens and Wendt, 1969]

$$\gamma_{ij} = \gamma_i + \gamma_j - 4\left[\frac{\gamma_i^d \gamma_j^d}{\gamma_i^d + \gamma_j^d} + \frac{\gamma_i^p \gamma_j^p}{\gamma_i^p + \gamma_j^p}\right] \tag{2.4}$$

$$\gamma_{ij} = \gamma_i + \gamma_j - 2\sqrt{\gamma_i^d \gamma_j^d} - 2\sqrt{\gamma_i^p \gamma_j^p} \tag{2.5}$$

where $\gamma_i = \gamma_i^d + \gamma_i^p$ is the surface tension of component *i*, being γ_i^d and γ_i^p its dispersive and polar contributions, respectively. The harmonic-mean equation is commonly used for materials having similar surface energies, such as polymers; on the other hand, the geometric-mean equation is recommended for materials with very different surface energies, and can then be used for estimating the filler/polymer interfacial tensions. Collections of surface energy data for common polymers and nanofillers have been recently reported [Fenouillot et al., 2009; Taguet et al., 2014]. In particular, a large dispersion of values has been noted for particles due to their different surface chemistries: the latter, indeed, can be varied for the same filler by adopting different chemical treatments, thereby affecting the localization in the blend.

The morphology of a ternary system composed either by three polymer phases or by two polymers and a solid filler can be also predicted from the spreading coefficients, defined on the basis of the interfacial tensions as follows:

$$\begin{aligned} \lambda_{j/i/k} &= \gamma_{jk} - \gamma_{ij} - \gamma_{ik} \\ \lambda_{i/j/k} &= \gamma_{ik} - \gamma_{ij} - \gamma_{jk} \\ \lambda_{i/k/j} &= \gamma_{ij} - \gamma_{ik} - \gamma_{jk} \end{aligned} \tag{2.6}$$

The parameter $\lambda_{i/k/j}$ shows the thermodynamic tendency of a phase *k* (polymer or particles) to spread between the other phases *i* and *j* [Steinmann et al., 2002]. In order to predict the equilibrium morphology, the complete set of spreading coefficients is required [Le Corroller and Favis, 2011]. If one of the coefficient is positive and the other two negative, complete encapsulation is observed. In the case of three negative coefficients, a partial wetting situation occurs, corresponding to a preferential particle localization at the polymer/polymer interface in a filled blend.

It is worth noting that the surface energies of polymers and particles are often measured at room temperature, while the wettability and spreading coefficients have to be estimated at the processing temperature in order to provide valuable information about the established morphologies. To this end, a linear temperature dependence of the surface energy and its polar and dispersive components is sometimes assumed, and the values are hence extrapolated at the required temperature.

Even though a correspondence between thermodynamic predictions and microscopy observations of the real morphology has been highlighted in several studies, the estimation of the interphase interactions is often not sufficient to assess

the localization of particles in multiphase polymer systems. Indeed, the selective distribution of the particles is linked to their wettability by the polymers provided that thermodynamic equilibrium is attained. This implies that the kinetic effects induced by the mixing route, which represent the subject of matter of the next section, have to be taken into account.

2.2.2 Uneven localization of nanoparticles: kinetic effects

When blending polymers with a solid filler, the final equilibrium morphology and the distribution of the particles are not immediately attained because of the high viscosity. Factors such as the sequence of mixing of the components, the viscosity evolution of the phases and the shear forces, may influence the rate of establishment of such equilibrium.

The order of addition of the components can have a strong effect on the kinetics and intensity of mixing because it has a direct influence on the medium with which the filler will be in contact during its incorporation. The simplest and most reported procedure is the simultaneous introduction of all the components in the mixing apparatus, followed by melt blending. In this route, the softening of the polymers is gradual and, if one polymer melts at a temperature significantly lower than the others, the solid particles may be incorporated into it despite showing higher affinity with other constituents. Since the obtained initial distribution will not be that corresponding to the thermodynamic equilibrium, different scenarios are then possible where the filler will have or not the opportunity to migrate to the preferred phase or to the interface. An alternative two-step procedure foresees the initial mixing of the polymers and the subsequent addition of the filler afterward, so that the particles do not see any solid medium. Moreover, it is possible to firstly incorporate the filler into one of the polymers and then add the other polymers.

Depending on these sequences of addition of the components, the filler may also have to migrate from one phase to the other to reach its equilibrium distribution. The easiest way to highlight the motion of particles inside a polymer blend is to incorporate the filler in the polymer having the lower affinity and then add the higher affinity polymers. For instance, Elias et al. have selected a silica-filled polypropylene/polystyrene (PP/PS) blend and a procedure involving the initial mixing of silica with PP and the later addition of PS [Elias et al., 2007]. They observed that all the hydrophilic silica transfers from the PP, with which it has lower affinity, towards the PS preferred phase; a few minutes mixing are sufficient for the migration to occur. Moreover, Gubbels et al. have focused on co-

continuous polyethylene/polystyrene (PE/PS) blends filled with carbon black located at the interface, prepared through two different procedures [Gubbels et al., 1998]. In the first process, PE and PS are initially mixed and the filler is added afterwards, the interfacial localization of the particles being controlled by thermodynamics. In the second process, the filler is first incorporated to PS, with which it has the lowest affinity, and PE is subsequently added. In this case, the kinetic control of the thermodynamically driven transfer of the filler from the less interacting phase (PS) toward the preferred one (PE) allows one to stop the melt blending process when most of the particles have accumulated at the interface. This implies that the melt mixing time should be controlled to maintain the filler at the interface, thereby minimizing the percolation threshold and optimize the conductivity. The kinetics of this transfer depends on the shear forces involved and the rheology of each polymer phase under the processing conditions. To summarize, the aforedescribed kinetic control, performed by quenching the multiphase system from the melt before attaining the equilibrium, can determine a particle distribution different from that the particle localization and is then exploitable to produce non-equilibrium morphologies without recurring to expensive and toxic surface treatments.

The relevance of the rheological properties (viscosity ratio) of the polymers for the determination of the final morphology has been clearly highlighted by Feng and co-workers for blends of polypropylene (PP) and poly(methyl methacrylate) (PMMA) filled with carbon black [Feng et al., 2003]. The latter can be dispersed either in the PMMA domains when the viscosity of PMMA is low, or at the interface when the viscosity of PMMA is intermediate, or in the PP matrix when the PMMA has the highest viscosity. Elias et al. have shown the influence of the molecular weight of two different kinds of poly(ethylene-vinyl acetate) (EVA) on the final morphology of PP/EVA blends filled with either hydrophobic or hydrophilic silica; all the component are compounded simultaneously [Elias et al., 2008]. The hydrophilic silica has more affinity with EVA, which is also the first polymer to melt; being located in this phase, the final morphology is the most thermodynamically stable one. Conversely, hydrophobic silica has better affinity with the PP matrix, which melts at a higher temperature than EVA; the filler migration is related to the EVA molecular weight, being easier in the case of the low-viscosity polymer. Finally, Zhou and co-workers have focused on blends of linear low-density polyethylene (LLDPE) and ethylene-methacrylic acid (EMA) filled with carbon black prepared by a one-step compounded procedure [Zhou et al., 2007]. Despite showing higher interactions with EMA, the filler is selectively

distributed in the non-polar LLDPE phase because of its lower viscosity compared to that of EMA. The authors claim that the particle/polymer interfacial tension of would be relevant just when the viscosities of the two polymers are comparable.

The mechanisms involved in the particle motion towards or through the interface have been recently reviewed [Fenouillot et al., 2009]. The shear stresses that establish during mixing are high enough to shift the adsorption/desorption equilibrium by extracting the particles from the interface. Actually, the particle movement and localization are induced by particle migration in the molten state and under shear rate. Indeed, the transfer of nanoparticles between two phases of a co-continuous systems is provided firstly by the contact between the filler and the interface, and secondly by the transfer from one phase to the other. The transport toward the interface can be provided by a combination of particle diffusion and shear-induced collisions of the particles with the blend interface. In the case of dispersed morphology, the same mechanisms are found when filler is initially located in the matrix phase; in the case of particles located in the dispersed domains, the transfer mechanism are instead still unclear. Göldel and co-workers have investigated the kinetics of transfer of carbon nanotubes between co-continuous styrene-acrylonitrile (SAN) and polycarbonate (PC) phases during melt mixing, demonstrating that the pre-mixing of the filler in one of the two polymers can be a determining factor for the final particle dispersion [Göldel et al., 2009; Göldel et al., 2012]. Indeed, the first polymer coming into contact with the nanotubes is thus adsorbed in a partially irreversible way and this adsorption can be responsible for the final blend morphology.

2.3 Nanoparticle-induced morphological modifications in immiscible polymer blends

The effectiveness of solid particles as morphological stabilizers is well known for several multiphase systems. A typical example is represented by Pickering emulsions, i.e. low-viscosity emulsions with interfacially-adsorbed colloidal particles. Moreover, if one of the fluids is air, the morphological constraint exerted by the filler leads to particle-stabilized foams and liquid drops (“dry liquids” and “liquid marbles”) [Thareja et al. 2008; Murakami and Bismarck, 2010].

Concerning immiscible polymer blends, a conventional route for the stabilization of both dispersed and co-continuous morphologies is the addition (or generation) of a compatibilizer. The latter is a block copolymer that adsorbs at the

interface between polymers and plays two main roles: (*i*) lowering the interfacial tension and hence promoting droplet breakup during processing (similarly to emulsifiers in low-viscosity emulsions); (*ii*) preventing subsequent coalescence phenomena [Sundararaj and Macosko, 1995; Van Puyvelde et al. 2001]. Unfortunately, for many polymer pairs it is very difficult, if not impossible, to synthesize the crucial compatibilizer, and further complications stem when dealing with systems comprising more than two polymer phases. A similar yet nonspecific compatibilizing effect has proven to be exerted also by nano-sized inorganic particles, whose usefulness goes then well beyond that of mere reinforcing agents. The intensive research conducted in the last two decades, whose most relevant output are here discussed, has highlighted that the selective localization of nanoparticles within a polymer blend is not only a way to increase the compatibility of polymer phases, but also to bring about a wide range of morphological modifications at different length scales.

2.2.2 Morphological modifications in dispersed systems

The compatibilizing effect of nanoparticles in multiphase polymer systems has been observed for the first time in a PE/PS blend filled with small amounts (< 5 wt%) of carbon black [Gubbels et al., 1995; Gubbels et al., 1998]. A consequence of the presence of particulate compatibilizers in polymer blends is the reduction of the size of the dispersed phase; this has been highlighted for various interfacially adsorbed nanofillers, such as silica [Vermant et al., 2004; Zhang et al., 2004; Elias et al., 2007], titanium dioxide [Li et al., 2008] and layered silicates [Khatua et al., 2004; Feng et al., 2004; Fang et al., 2007]. The latter, in particular, are able to promote drastic morphological refinements. Organoclay-filled PC/PMMA systems exhibit an apparent miscibility, evidenced by the collapse of the glass transition temperature of the polymeric constituents into one; this has been ascribed to the small size of the polymer phases and their immobilization by strong interactions with the solid filler [Si et al., 2006]. Interfacial rheology is found to play a major role in coalescence suppression: nanoparticles covering polymer/polymer interfaces can form strongly viscoelastic layers, thereby acting as interfacial mobility modifiers rather than conventional compatibilizers [Vandebril et al., 2010; Filippone et al., 2011b].

The main mechanisms proposed to explain the compatibilizing role of nanofillers in polymer blends have been recently reviewed [Fenouillot et al., 2009]: (*i*) interfacial tension reduction; (*ii*) coalescence inhibition due to the presence of a

solid barrier around the minor polymer phase; (*iii*) viscosity ratio change due to the presence of the filler in one of the polymer phases; (*iv*) formation of a physical network of particles that immobilizes one of the phases; (*v*) adsorption interaction of macromolecules at the particle surface. Regarding the first mechanism, as pointed out in §2.1, in the compounding process breakup and coalescence phenomena compete with each other, the latter being determined by the unfavorable interactions among molecular segments of the immiscible components. The interfacial modification induced by the presence of unevenly distributed particles alters the breakup/coalescence equilibrium in favor of the first phenomenon. As far as viscosity ratio changes are concerned, it is worth noting that if the filler preferentially locates within the matrix, it can be trapped in the film between two colliding drops, thereby impeding its drainage and slowing down the coalescence [Kelnar et al., 2007]. Focusing on clay-filled low-density polyethylene/polyamide 12 (LDPE/PA12) blends, Huitric et al. have ascribed the morphological refinements detected at different compositions to the different filler distributions and, ultimately, to the occurrence of various aforementioned mechanisms [Huitric et al., 2009]. When LDPE is the matrix, almost all the filler is situated at the polymer-polymer interface and the domain size reduction ensues only from coalescence inhibition due to the solid barrier effect. Conversely, when PA12 is the matrix, both the latter and the interface host the filler and a double effect emerges: on one hand, the particles located in the matrix increase its viscosity and induce drop break-up; on the other hand, coalescence is inhibited by the interfacially-adsorbed platelets. Similarly, Hong and co-workers have reported that a refinement of the morphology of clay-filled blends of PE and polybutylene terephthalate (PBT) [Hong et al., 2006]. At low filler content, the particles gather at the interface and hence suppress drop coalescence; at higher contents, they also locate in the more affine PBT phase, thereby changing the viscosity ratio and influencing drop breakup. By means of rheological analyses, Elias et al. have stated that the stabilization mechanism of silica-filled PP/PS blends is the reduction of the effective interfacial tension in the case of hydrophilic particles, and the formation of a rigid barrier preventing coalescence in the case of hydrophilic particles [Elias et al., 2007].

Similarly to that of conventional compatibilizers, the effect of adding particles to polymer blends is not symmetric [Van Hemelrijck et al., 2005; Martin and Velankar, 2007; Gong and Leal, 2012]. Indeed, a given particle may be able to prevent coalescence in an A-in-B droplet/matrix blend but not in a B-in-A blend. According to Vermant et al., fumed silica particles suppress coalescence in a

polyisobutylene/polydimethylsiloxane (PIB/PDMS) blend only if PIB forms the dispersed phase; this has been ascribed to a preferential wetting of the filler by the PDMS [Vermant et al., 2004]. Later experiments with a wider variety of fillers showed even more extreme asymmetry: a given particle type can either increase or decrease the drop size (i.e. either hinder or promote coalescence), depending on the phase that is continuous [Thareja et al., 2010]. Another asymmetry is related to the flow conditions experienced by the systems: indeed, clay particles located at the interface of a PS/PMMA blend are reported to induce a morphology refinement under intense flows and a coarsening, due to clustering phenomena of coated PMMA droplets, during slow and prolonged flows [Filippone and Acierno, 2012]. Besides the extremes of coalescence promotion and suppression, solid fillers can also induce an intermediate phenomenon, called "arrested coalescence": colliding droplets remain frozen while coalescing due to the presence of particles either interfacially adsorbed or confined inside the minor phase. The arrest ensues from a balance between the interfacial energy reduction and the elasticity increase that occur during coalescence [Pawar et al., 2011; Pawar et al., 2012].

Another remarkable effect due to nanoparticle addition in multiphase systems is the stabilization of non-spherical fluid domains. Sufficiently high amounts of interfacially-adsorbed spherical particles can jam the interface of non-polymeric systems, slowing down or even arresting the shape relaxation process [Cheng and Velankar, 2009; Pawar et al., 2011; Si et al., 2006]. The stabilization of irregularly shaped domains has also been reported when the particles selectively locate within either of the fluid phases [Pawar et al., 2012; Li et al., 2011]: in this case, the slackening of the shape relaxation and breakup is ascribable to the increased elasticity and viscosity of the host phase. When particles adsorb at two liquid-liquid interfaces simultaneously, they can bridge across drops and glue them into clusters [Thareja and Velankar, 2007; Thareja and Velankar, 2008; Vermant et al., 2008]. Such bridging phenomena occur when particles are preferentially wetted by the continuous phase and have major rheological implications, imparting a solid-like behavior to the blend [Nagarkar and Velankar, 2012].

2.2.3 Stabilization and promotion of co-continuous morphologies

As highlighted in §2.1, the range of composition where a multiphase polymer system forms a co-continuous morphology is mainly influenced by the volume fraction of the polymers, their viscosity ratio and elastic properties, and process-related parameters (shear rate during mixing, mixing time) [Pötschke and Paul,

2003]. Based on these factors, the shape of the minor phase is also claimed to play a relevant role: indeed, elongated domains exhibit a lower percolation threshold, and hence a lower onset of continuity, than spheroidal drops [Willemse et al., 1998]. The stability of elongated domains is related to the balance between the polymer/polymer interfacial tension, which drives the minor phase to recover a spherical shape or to fragment into smaller droplets, and the rheological stresses related to such morphological evolutions.

For the stabilization of co-continuous morphologies in polymer blends, like in the case of dispersed microstructures, nanoparticles have recently revealed to be a viable, more generally applicable alternative to conventional compatibilizers. One of the pioneering studies in this sense is that of Gubbels et al., who have achieved kinetic stabilization of co-continuous morphologies in PE/PS blends by adding carbon black, through both interfacial segregation and preferential location of the filler within the PE phase [Gubbels et al., 1995]. In particular, they have detected a decrease of the onset of PE continuity from 30 to 5 wt% in the presence of carbon black (4 phr). Interfacial jamming has been proposed as a viable route for co-continuity stabilization co-continuous structures: the idea is to create a "bijel", i.e. a bicontinuous morphology with a high particle coverage at the interface, so that structural coarsening can be arrested [Stratford et al., 2005]. Alternatively, one can obtain the initial bicontinuous morphology under appropriate processing conditions and then allow it to coarsen until the interface jams [Cheng, 2009]. The necessity for neutral wetting of the particles, that is stringent for interfacial jamming, can be overcome by recurring to the route described by Li et al., who have obtained kinetically trapped co-continuous polystyrene/poly(vinyl methyl ether) (PS/PVME) morphologies through the gelation (i.e. network formation) of CdSe particles inside the PVME phase [Li et al., 2011]. In agreement with the expected dependence of the filler percolation threshold on the aspect ratio, the particle concentration required for the kinetic arrest is smaller for nanorods (1-2 vol%) than for nanospheres (2-3 vol%).

The underlying mechanisms of nanoparticle-induced co-continuity in immiscible polymer blends are a matter of intensive investigation by Filippone and co-workers. Dealing with organoclay-filled high density polyethylene/polyamide 6 (HDPE/PA6) blends, they have shown that the selective localization of the filler inside the minor polyamide phase is responsible for a refinement of the globular morphology at low particle loadings, and for the transition to a co-continuous phase arrangement starting from a critical threshold (clay/PA6 weight ratio = 0.2) [Filippone et al., 2008; Filippone et al., 2010a; Filippone et al., 2010b]. In

correspondence of the latter, as revealed by rheological analysis, the blend exhibits a gel-like behaviour ascribable to the slackened melt-state dynamics of the filled PA6 phase. This suggests that the filler is able to drive the space arrangement of the preferred polymer phase: as a consequence, above a critical filler content a double percolating network forms, where the preferentially wetted phase gets continuous as it coats a space-spanning filler network. The same occurrence has been reported for polylactic acid/polyamide 11 (PLA/PA11) blends filled with clay particles, which are located inside PA11 and at the polymer/polymer interface [Nuzzo et al., 2014a]. However, the addition of other kinds of fillers, such as carbon nanotubes, may strike off the correspondence between the onsets of co-continuity and filler network formation [Nuzzo et al., 2014b]. Based on this finding, the authors suggest that, besides the kinetic arrest of the melt-state relaxation dynamics of the filled phase through the assembly of a filler network, other mechanisms take part in the promotion of co-continuity. In particular, the deformability of nanoparticles and their ability to lower the interfacial tension between the polymers are claimed to be influential factors. The comparison of blends of HDPE and poly(ethylene oxide) (PEO) containing different nanofillers has allowed to highlight the role of interfacial rheology in altering the onset of co-continuity: the most relevant effect has been found in the presence of interfacially-adsorbed clay particles and ascribed to their ability to slow down the relaxation dynamics of the interface [Filippone et al., 2011b]. Finally, concerning the impact of the processing conditions, a single-step compounding protocol has revealed to be more effective in promoting co-continuity in a clay-filled PS/PA6 blend than a multi-step procedure [Filippone et al., 2011a].

Further evidence of the influence of nanoparticle addition on the onset of co-continuity of multiphase polymer systems has been given by Xiang and co-workers, who have focused on HDPE/PA6 blends at weight ratio 50/50 [Xiang et al., 2012]. The unfilled system exhibits a dispersed morphology, PA6 forming the continuous phase; the transition to a co-continuous structure is induced upon the addition of small amounts of multiwalled carbon nanotubes (2÷5 phr), and phase inversion (dispersion of PA6 in HDPE) has been found to occur at higher filler contents (~ 10 phr). Moreover, Wu et al. have reported that the percolation threshold of carbon black decreases from 8 to 2 phr upon the addition of a preferred PA6 phase (40 wt%) to an acrylonitrile-butadiene-styrene (ABS) matrix [Wu et al., 2010a]. At that particle concentration, the so-called double percolation effect emerges: a filler-based network and a co-continuous polymer network coexist in the system. Noting that increasing the filler content determines a

decrease of the amount of PA6 needed to form an interpenetrated particle network, the authors have demonstrated that the product of the volume fractions of the filler and the minor polymer component is constant for a given system. Such a finding is widely applicable to nanoparticle-containing immiscible polymer blends and can hence be used for designing and controlling co-continuous morphologies [Taguet et al., 2014].

2.4 Morphology-property relationships

The interest in obtaining specific morphologies in multiphase materials is often driven by the motivation to attain specific combinations of properties. Hereinafter, some meaningful examples are reported regarding how the morphological modifications that ensue from the incorporation and selective localization of nanoparticles in a multiphase polymer system may impart peculiar mechanical, thermal, electrical, and flammability characteristics to the host matrix.

Elastomers are often blended with rigid polymers to increase the impact strength and toughness of the final system, and further improvements are achievable through the incorporation of clay nanoparticles. Specifically, several studies highlight that a selective localization of the filler is necessary to obtain the desired mechanical performances. High impact strengths have been detected in blends of polyamide 66 (PA66) and styrene-ethylene-butylene-styrene (SEBS) and LLDPE/EMA if the filler is located in the PA66 and EMA phase, respectively [Dasari et al., 2005; Borah et al., 2011]. Moreover, an enhanced toughness has been reported for a blend of PA6 and ethylene propylene rubber (EPR), where the localization of the clay at the interface may bring about a "core-shell" structure of the elastomeric phase, and in a polypropylene/styrene-butadiene-styrene (PP/SBS) system, which exhibits higher resistance to crack initiation and propagation than its unfilled counterpart [Kelnar et al., 2006; Li et al., 2002]. Such toughening effect has been ascribed to the possibility of varying the elastomer domain size and distance through the addition of nanoparticles, which are able to form networks around the rubber domains and increase their effective volume [Kim et al., 2007]. The addition of clay particles and natural rubber (NR) has also been used to improve the mechanical properties of a PLA matrix [Bitinis et al., 2012]. The filler, located at the polymer/polymer interface, provides a solid barrier against the coalescence of NR droplets, enhancing the blend elongation at break and stiffness.

The possibility of exploiting nanoparticle-induced co-continuity to enhance the thermal resistance of polymers is recently emerged. In a series of papers, Filippone and co-workers have shown this effect by blending polymers characterized by low melting temperatures, such as HDPE, LDPE and PLA, with small amounts of polyamide, which exhibits high melting point. The selective localization of clay particles in the minor polyamide phase (or at the interface) may bring about the formation of a continuous filled framework that acts as a scaffold for the less resistant phase [Filippone et al., 2010a; Filippone et al., 2010b; Nuzzo et al., 2014a]. The same underlying mechanism has allowed to improve the photo-oxidation resistance of a HDPE/PA6 blend [Dintcheva et al., 2010].

Focusing on the electromagnetic properties, a well-established route to render a polymer conductive is the incorporation of conductive fillers in a content high enough to reach the percolation threshold. The latter depends on the particle shape, dispersion and interaction with the matrix, as well as the viscosity of the matrix. In a multiphase system, such critical filler content can be lowered if the filler selectively distributes in one of the phases [Feng and Chan, 1998] or at the interface of a co-continuous phase arrangement [Gubbels et al., 1995; Gubbels et al., 1998; Sumita et al., 1992], as pointed out for carbon black. Concerning carbon nanotubes, Zonder et al., who have minimized the resistivity in a HDPE/PA12 blend by premixing filler and HDPE and inducing the interfacial localization of the particles; the same route has been exploited by Hwang and co-workers in a PP/PS blend [Zonder et al., 2011, Hwang et al., 2012]. PA6/Fe_3O_4 magnetic microspheres with regular shape and size have been obtained incorporating Fe_3O_4 particles in a PS/PA6 blend and subsequently extracting the major PS phase [Wu et al., 2010b].

Finally, the flammability of polymer matrices is well known to be enhanced by layered silicates, which exert a barrier effect reducing the diffusion of volatile thermo-oxidation products to the gas phase, and of oxygen to the polymer [Zanetti et al., 2002]. Organoclays may also act as a dispersant for fire retardant particles, the consequent synergy leading to enhanced thermal stability and flame retardancy [Pack et al., 2009]; this has been recently pointed out for blends of PP and polyethylene terephtalate (PET) where the filler has a propensity to locate inside the PET matrix or at the interface [Entezam et al, 2013].

The previous overview of the morphology/property relationship in nanofilled multiphase polymer systems is definitely not exhaustive. Actually, it just serves to highlight the great potential of nano-sized fillers as a vehicle to impart outstanding performances to polymer blends thanks to the ability to drive their microstructure.

3

Assembly of plate-like nanoparticles in multiphase polymer systems – Morphological implications*

In this chapter, the assembly of plate-like nanoparticles in an immiscible polymer blend is studied through the combination of morphological and rheological analyses, aiming to elucidate how the mutual interactions among the phases dictate the morphology of the system. After highlighting the benefits of such an approach and providing experimental details (§3.1), the attention is directed to a "reference" system based on a monophasic polymer matrix, assessing the initial space arrangement and melt-state assembly dynamics of the nanoparticles (§3.2). An analogous investigation is performed on the filled polymer blend, aiming to highlight how the assembly process is affected by the presence of fluid/fluid interfaces where the filler is inclined to gather (§3.3). The filler content is varied in a wide range to cover all the possible structures, from isolated flocs to continuous networks, whose peculiarities in the mono- and biphasic polymer systems are compared (§3.4). Finally, the role of nanoparticles in altering the transition from dispersed to co-continuous blend morphologies is discussed (§3.5).

3.1 Prefatory notes

Aiming to use nanoparticles as clever means to impart peculiar structure and properties to multiphase polymer materials, one cannot escape from a deep understanding of the mutual interactions among the constituents of such heterogeneous systems and their impact on the final morphology. Nonetheless, the

* Part of the results presented in this chapter has been published in Filippone G, Causa A, Salzano de Luna M, Sanguigno L, Acierno D, "Assembly of plate-like nanoparticles in immiscible polymer blends – Effect of the presence of a preferred liquid–liquid interface", Soft Matter 10, 3183-3191 (2014).

inherent abundance of scattering surfaces in multiphase systems complicates the direct visualization of their 3D morphology via optical or spectroscopic techniques. Provided the liquids and the solid phase fulfil cogent requisites in terms of characteristic sizes and refractive indices, valuable structural information can be obtained through confocal microscopy [Lee et al., 2012]. Alternatively, ex-post analyses can be performed on solidified samples (for instance, by cryogenic quenching), with the disadvantage of losing valuable information about the link between morphology and rheology [Vandebril et al., 2010]. This relationship is recovered when dealing with multiphase polymer systems. Indeed, as the high viscosity of polymer melts slows down the kinetics of particle assembly, rheology can be profitably used to appreciate even subtle microstructural changes regardless of the transparency and refractive indices of the components. Furthermore, if either of the polymers can be selectively dissolved and removed from the blend, extraction experiments can be performed to assess the variations in the 3D morphology (in particular, its transition from dispersed to co-continuous) with changing the blend composition [Galloway and Macosko, 2004].

The study presented in this chapter well fits in this scenario, as it combines morphological analyses and rheological measurements to investigate the assembly of nanoparticles in multiphase polymer systems. The ultimate goal is to elucidate how the particles govern the blend morphology and how, in turn, the structural evolutions of the fluids affect the spatial arrangement of the filler. Accordingly, model systems are prepared through a judicious selection of the materials. The main blend constituents are polystyrene (PS) and poly(methyl methacrylate) (PMMA). As both polymers are amorphous, the structures formed in the melt state can be preserved in the solid samples; otherwise, crystallization would compromise the link between melt- and solid-state morphology, making ex-post microscopic analyses unreliable. The choice of the filler is addressed by the interest in understanding the effect of preferred fluid/fluid interfaces on the particle assembly process. Organically-modified clay nanoparticles are selected due to (*i*) their plate-like shape, which well adapts to polymer-polymer interfaces, and (*ii*) their bending stiffness, high enough to overcome the interfacial elasticity of the blend and make the filler discernible via rheological analyses. The influence of nanoparticle structuring on the phase inversion of the blend is finally inspected coupling microscopic analyses and PMMA extraction tests.

The PS (Edistir® 2982 by Versalis) has glass transition temperature T_g = 100 °C and zero-shear rate viscosity $\eta_0 = 3\times10^3$ Pa s at T = 190 °C. The PMMA (Optix® CA-51 by

Plaskolite, Inc.) has T_g = 110 °C and $\eta_0 = 4\times10^4$ Pa s at T = 190°C. The filler (Cloisite® 15A by Southern Clay Products, Inc.) is a montmorillonite modified with dimethyl dihydrogenated tallow quaternary ammonium salt with an organic content of ~43%.

Two sets of samples have been prepared by adding different amounts of clay to either pure PS or PS/PMMA systems at various compositions. The constituents, dried overnight under vacuum at 90 °C, have been simultaneously loaded and melt compounded using a co-rotating twin-screw extruder (15 mL Micro Compounder, DSM Xplore). The extrusions have been performed at T = 190 °C in a nitrogen atmosphere. The screw speed is set to 150 rpm, corresponding to average shear rates of ~ 75 s^{-1}, and the residence time, accurately controlled by means of a backflow channel, is 240 s. The extrudate has been granulated, dried again and compression molded in the form of disks (diameter: 25 or 40 mm; thickness: 1.5, 3 or 4.5 mm) for the subsequent rheological and morphological analyses. The unfilled PS and PS/PMMA blends have been processed in the same conditions.

Wide angle X-ray diffractometry (WAXD) has been performed on the pristine clay and representative clay-filled samples using a Siemens D-500 diffractometer with Cu Kα radiation (λ = 0.154 nm). Scans have been taken from $2\theta = 2\div10°$ with a step size of 0.02°.

A stress-controlled rotational rheometer (AR-G2 by TA Instruments) in parallel-plate geometry (plate diameter 40 mm) has been used for the rheological analyses. Oscillatory tests have been performed at T = 190 °C in a dry nitrogen atmosphere. Specifically, low-frequency (ω = 0.1 rad s^{-1}) time sweep experiments and frequency scans ($\omega = 0.02\div200$ rad s^{-1}) have been performed in the linear viscoelastic regime, whose limit had been previously determined for each sample through strain amplitude experiments.

Thermogravimetric analyses (TGA Q5000 by TA Instruments) have been performed on each tested sample in order to accurately estimate its actual filler content. The samples have been heated at 10 °C min^{-1} in nitrogen atmosphere from room temperature up to T = 700 °C, and the residuals have been recorded at T = 600 °C.

Quantitative extraction experiments have been carried out in order to separate the polymer phases of the unfilled and filled PS/PMMA blends. Formic acid (density ρ = 1.22 g cm^{-3}, purity grade > 95 wt%, purchased from Sigma Aldrich), that is a good solvent for PMMA and a non-solvent for PS, is used for this purpose. The extraction process, performed upon three disks for each composition, has been protracted for three weeks. Before the subsequent analyses, the tested samples (all found self-supporting at the end of the extractions) have been dried under vacuum for 48 h at T = 70 °C to purge the solvent.

The morphology of the samples has been inspected through both scanning (SEM) and transmission (TEM) electron microscopy. SEM observations have been carried out using a QUANTA 200F FEG-ESEM by FEI on gold-sputtered fractured surfaces taken from samples previously subjected to extraction experiments. TEM analyses are performed with a Tecnai G2 Spirit Twin T-12 by FEI. The specimens are slices with thickness ~ 100 nm, cut at room temperature using a Leica EM UC7 ultra-microtome equipped with a diamond knife. The binarized micrographs are analyzed using the free software ImageJ®.

3.2 Assembly of nanoparticles in a monophasic polymer matrix

The morphology of the PS/clay sample at filler volume fraction Φ = 1.32% soon after the extrusion process is shown in the TEM micrographs of Figure 3.1. The filler is in the form of stacks of several layers (lateral dimension of few tens of nanometers) plus few exfoliated lamellae, randomly oriented in the polymer matrix. The uniform distribution of the filler on the micrometric scale results from the stresses experienced by the materials during mixing, which cause the pristine clay aggregates to break into smaller tactoids. The penetration of the polymer chains inside the clay galleries is responsible for the increase of the interlayer distance, leading to the intercalation/exfoliation of the platelets. This observations are corroborated by X-ray diffractometry, which reveals a moderate expansion of the basal spacing with respect to the pristine clay (see Appendix A.1).

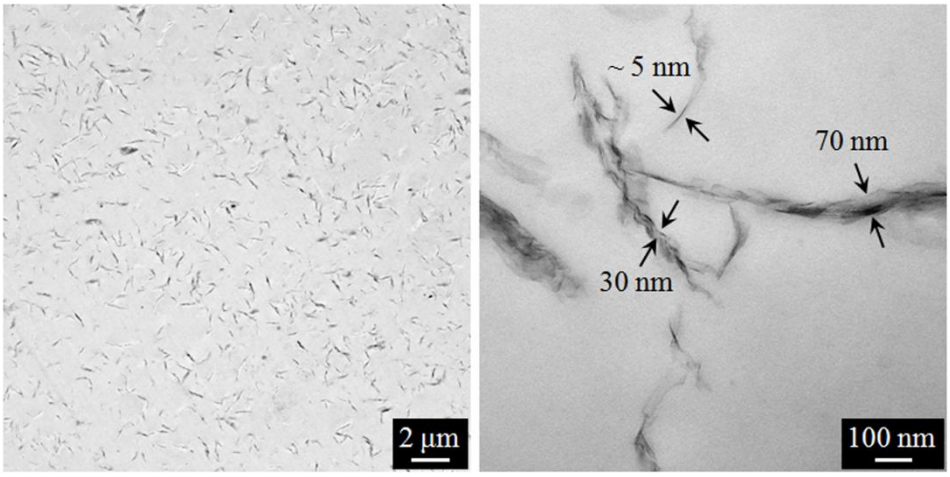

Figure 3.1 – TEM micrographs of the as-extruded PS/clay sample at Φ = 1.32%.

Once the temperature is raised up above the melting/softening point of the host polymer matrix, nano-sized particles tend to rearrange towards more stable configurations. The kinetics of this process have been assessed monitoring the time evolution of the linear elastic modulus G' at a frequency low enough to neglect the elastic contribution of the matrix. The results of time scans at 190 °C and ω = 0.1 rad s^{-1} for PS/clay samples at different filler content are shown in Figure 3.2a, where the moduli have been divided by their initial value $G'(0)$. The elasticity of

the samples grows during time at any Φ. The growth rate is faster in the earlier stages, then the elasticity approaches a time-independent value, $G'(\infty)$. As shown in Figure 3.2b, the normalized equilibrium moduli $G'(\infty)/G'(0)$ gradually scale with Φ at low filler contents, then a kind of saturation is achieved. The viscous modulus G'', not shown, remains essentially stable over time.

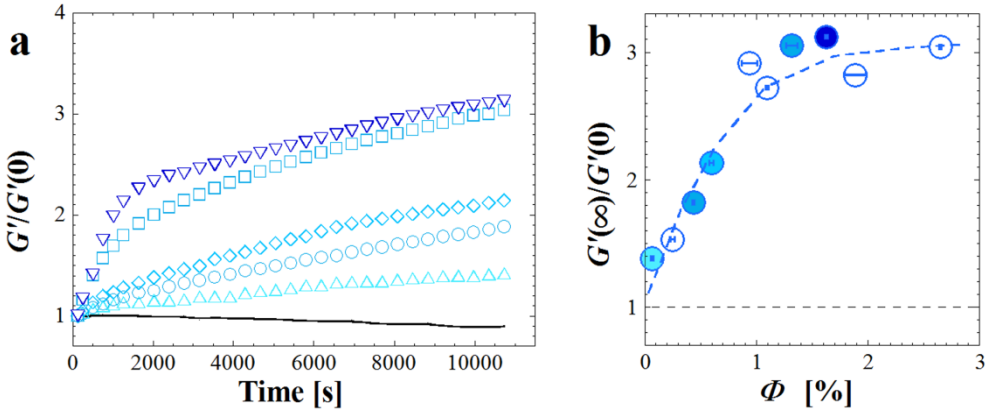

Figure 3.2 – (a) Time evolution of G' (normalized over the initial value) at ω = 0.1 rad s^{-1} for PS/clay samples at Φ = 0.07, 0.44, 0.60, 1.32 and 1.63% (from bottom to top). (b) Normalized equilibrium values of G' attained at the end of time scans; semitransparent symbols are related to the samples whose Φ is mentioned above. Adapted from [Filippone et al., 2014] with permission of the Royal Society of Chemistry.

At the end of the time scans, the shear moduli are stable enough to perform reproducible frequency scan experiments, aimed to address the effect of nanoparticle concentration over the viscoelasticity of the systems. The frequency dependence of G' and G'' is shown in Figure 3.3 for the neat PS and PS/clay samples at different filler content. The PS matrix is predominantly viscous in the investigated frequency range, exhibiting terminal Maxwellian behaviour ($G' \sim \omega^2$, $G'' \sim \omega^1$) at low ω. The relaxation spectrum radically changes in the presence of nanoparticles: both the elastic and viscous moduli monotonically increase with Φ in the whole frequency range, the effect being more pronounced on G' at low ω. Actually, the high-frequency response is dominated by the PS matrix, while the filler is responsible for a slight vertical shift of the moduli. Over longer timescales, the filler gradually slows down the relaxation dynamics. This is evidenced by the flattening of the G' plots at low ω, which reflects a gradual transition from a liquid-like behavior ($G'' > G'$) to a solid-like one ($G' > G''$ and low ω-dependence).

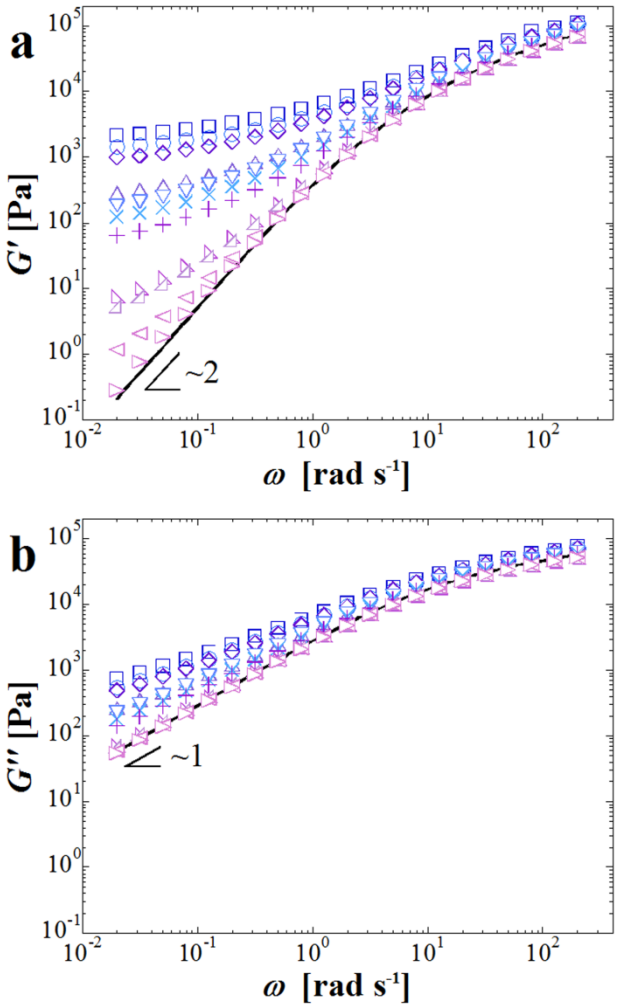

Figure 3.3 – Frequency-dependent (a) elastic and (b) viscous moduli of the neat PS (solid line) and PS/clay nanocomposites at Φ = 0.07, 0.25, 0.44, 0.60, 0.94, 1.10, 1.27, 1.32, 1.63, 1.89 and 2.65% (from bottom to top). Adapted from [Filippone et al., 2014] with permission of the Royal Society of Chemistry.

3.3 Assembly of nanoparticles in a biphasic polymer matrix

The morphology and nanoparticle assembly in the pure PS matrix have been compared with those occurring in a PS/PMMA blend at 15 wt% of PMMA. As

highlighted in §2.2, the localization of a filler in a polymer blend at thermodynamic equilibrium can be predicted through the estimation of the wettability parameter and the spreading coefficients at the processing temperature. To this end, the surface tensions γ_i of the constituents of the studied blends, namely PS, PMMA and organoclay, have been estimated at T = 190 °C assuming that they vary linearly with T and using literature data for the temperature coefficients $\partial\gamma_i/\partial T$. Then, the surface tension at high temperature is splitted in its polar and dispersive components keeping the same ratio between the two as that at room temperature. Due to the lack of surface tension data for the used filler, literature values reported for Cloisite® 10A have been employed as a first approximation. This expedient is legitimated by the similar values of the dispersive component exhibited by many organically modified layered silicates (against a greater sensitiveness of the polar part to the nature of the organo-modifier) [Picard et al., 2002]. The literature values of the surface tension and its components for the polymers and the filler at room temperature are summarized in Table 3.1 together with the corresponding temperature coefficients and the extrapolated values at T = 190 °C.

Table 3.1 – Dispersive and polar components of the surface tensions of the pure materials at room temperature (T = 20 or 25 °C) and at T = 190 °C as obtained by linear extrapolation using the reported temperature coefficients.

	Surface tensions at room T [mN m^{-1}]			**$\partial\gamma_i/\partial T$ [mN m^{-1} °C^{-1}]**	**Surface tensions at T = 190 °C [mN m^{-1}]**		
	γ_i	γ_i^d	γ_i^p		γ_i	γ_i^d	γ_i^p
PS	40.6 [a]	34.5 [a]	6.1 [a]	- 0.072 [a]	28.5	24.2	4.3
PMMA	41.1 [a]	29.6 [a]	11.5 [a]	- 0.076 [a]	28.2	20.3	7.9
Clay	45.2 [b]	33.4 [b]	11.8 [b]	- 0.136 [c]	22.9	16.9	6.0

[a] From http://www.surfacetension.de/solidsurface-energy.htm (accessed June 1st, 2012)
[b] From [Kamal et al., 2009]
[c] Estimated by [Picard et al., 2002]

Table 3.2 reports the interfacial tensions between PS and PMMA (estimated from Equation 2.4) and between the polymers and the filler (computed from Equation 2.5), as well as the wetting and spreading coefficients (calculated substituting the interfacial tension values in Equations 2.3 and 2.6 respectively).

These data indicate that the clay particles are inclined to locate at the PS/PMMA interface and have a slightly higher affinity with PMMA.

Table 3.2 – Polymer/polymer and polymer/filler interfacial tensions, wetting parameter and spreading coefficients at the operating temperature T = 190 °C.

Parameter	Value [units]
$\gamma_{PS/PMMA}$	1.48 [mN m^{-1}]
$\gamma_{PS/clay}$	0.91 [mN m^{-1}]
$\gamma_{PMMA/clay}$	0.34 [mN m^{-1}]
$\omega_{PS/PMMA/clay}$	0.39 [-]
$\lambda_{PS/PMMA/clay}$	- 2.05 [mN m^{-1}]
$\lambda_{PMMA/PS/clay}$	- 0.91 [mN m^{-1}]

The aforedescribed prediction is corroborated by morphological analyses. TEM micrographs of a representative, as extruded PS/PMMA/clay sample (Φ = 0.32%) are reported in Figure 3.4. The clay, in the form of stacks of several silicate layers with lateral dimension of few hundreds of nanometers, mostly adheres at the surface of the PMMA droplets. The tactoids, which at this composition do not saturate the available interface, do not bend to trace out the contours of the drops, whose shape, instead, adapts to the clay. In other words, the bending stiffness of the particles prevails over the interfacial tension and stabilizes non-spherical drops. According to X-ray diffractometry (see Appendix A.1), the basal spacing exhibits a slight increase in comparison with the pristine clay.

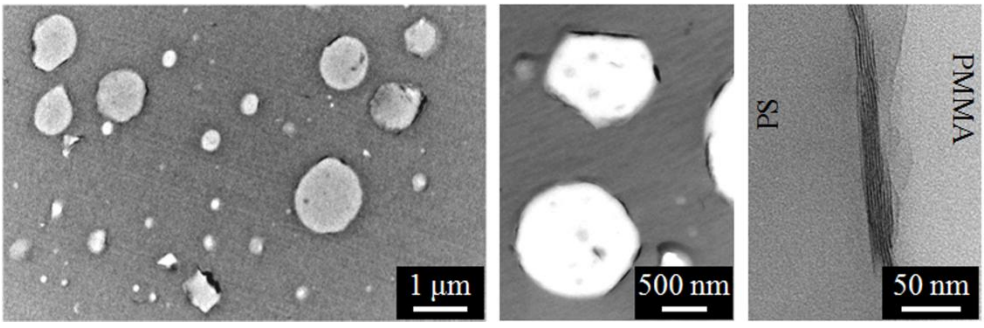

Figure 3.4 – TEM micrographs of the as-extruded PS/PMMA/clay sample at Φ = 0.32%. Adapted from [Filippone et al., 2014] with permission of the Royal Society of Chemistry.

Significant differences between the PS/clay and PS/PMMA/clay systems emerge when comparing the results of time scans shown in Figure 3.5 with those reported in Figure 3.2. The behavior of the unfilled blend, which experiences a slight increase of G' due to some thermal degradation of the continuous PS phase, is exactly retraced by the PS/PMMA/clay samples up to $\Phi < 0.93\%$. Above this threshold, the elasticity starts to grow during time, eventually reaching equilibrium values (reported in Figure 3.5b) that are lower than those of the PS/clay samples at comparable filler content.

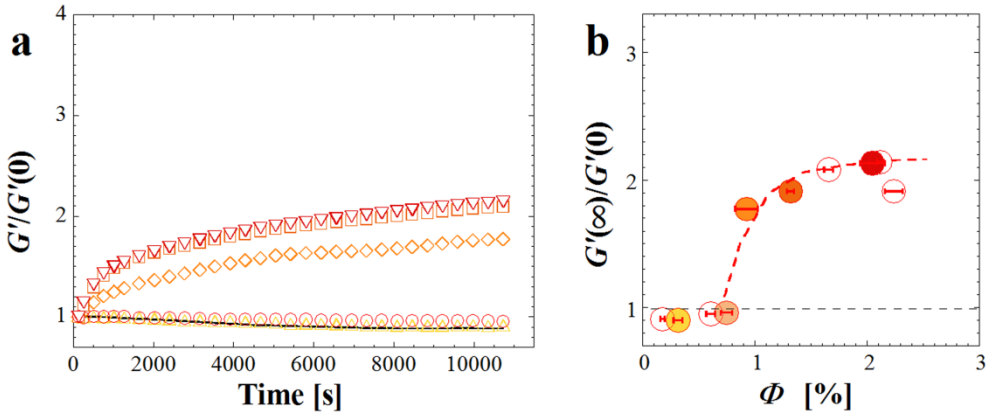

Figure 3.5 – (a) Time evolution of G' (normalized over the initial value) at $\omega = 0.1$ rad s^{-1} for PS/PMMA/clay samples at $\Phi = 0.32$, 0.75, 0.93, 1.32 and 2.05% (from bottom to top). (b) Normalized equilibrium values of G' attained at the end of time scans; semitransparent symbols are related to the samples whose Φ is mentioned above. Adapted from [Filippone et al., 2014] with permission of the Royal Society of Chemistry.

A similar effect of particle concentration is found considering the frequency-dependent linear viscoelastic moduli of the PS/PMMA/clay samples, measured after the thermal aging and reported in Figure 3.6. Concerning the unfilled blend, the high-frequency behavior is governed by the continuous PS phase, while the enhanced elasticity detected at low ω reflects the shape relaxation of the PMMA drops. The predictions of the Palierne model (see Appendix A.2) well fit the experimental data, confirming the reliability of the performed rheological measurements. In the presence of the filler, no relevant effects are found below Φ = 0.75%; such value is close to the threshold above which the elasticity of the blends starts to increase over time. From this composition on, the curves of G' flatten out, reaching a low-frequency plateau at the highest filler contents. The issue that will

be addressed in the next section is the link between such “delayed” rheological transition and the existence of fluid-fluid interfaces where the nanoparticles are inclined to gather, thereby losing their mobility.

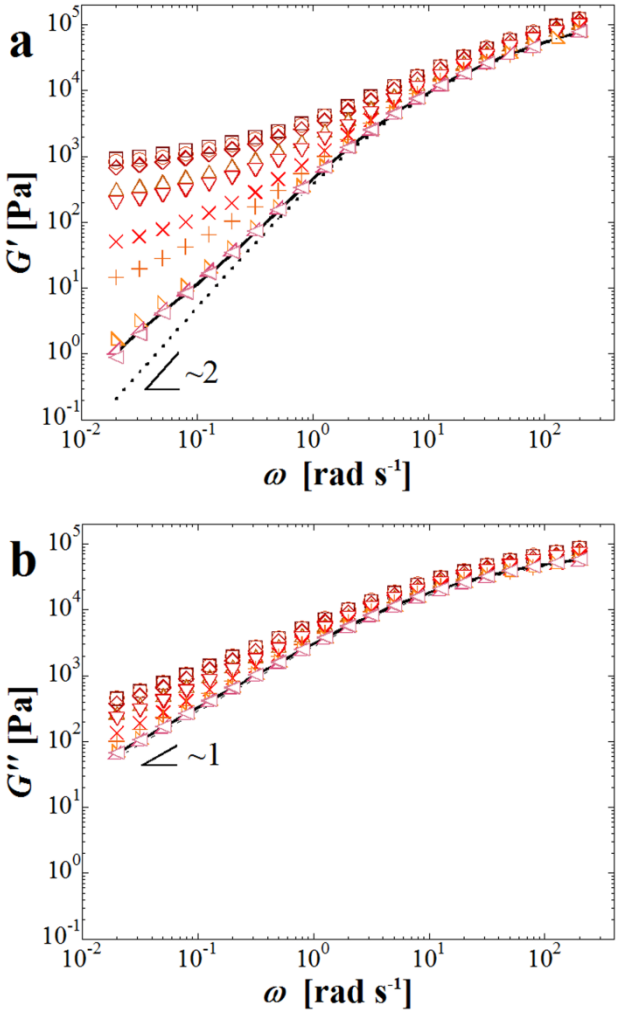

Figure 3.6 – Frequency-dependent (a) elastic and (b) viscous moduli of the neat PS (solid line) and PS/clay nanocomposites at Φ = 0.18, 0.32, 0.61, 0.75, 0.93, 1.32, 1.66, 2.05, 2.12 and 2.24% (bottom to top). Adapted from [Filippone et al., 2014] with permission of the Royal Society of Chemistry.

3.4 Comparison of the nanoparticle structures in the mono- and biphasic polymer matrices

From the results presented up to now, a substantial difference emerges between the PS/clay and PS/PMMA/clay systems. When the filler is dispersed in a monophasic fluid matrix, its impact on the overall rheological response is clearly appreciable at almost any Φ. On the other hand, the presence of nanoparticles in a biphasic matrix, where they preferentially locate at the fluid-fluid interface, affects the viscoelastic response of the filler only at sufficiently high filler content. Hereinafter, the characteristics of the studied systems are discussed in more detail, aiming to understand the different melt-state particle dynamics in the two suspending mediums.

3.4.1 Mechanisms of nanoparticle assembly

The growth of the elasticity at rest is a rheological peculiarity of nanofilled polymer systems, reflecting structuring phenomena of nanoparticles and the increase of their effective volume. Depending on filler content, different underlying mechanisms can be recognized. At very low Φ, the evolution of G' is related to the rotation of plate-like particles, which consequently lose the alignment imposed by the squeezing flow experienced during sample loading [Kim and Macosko, 2009]. An additional contribution arises at higher Φ due to particle flocculation, that is responsible for the confinement of the polymer between the forming flocs and pronounced hydrodynamic effects. Above the percolation threshold Φ_c, a space-spanning filler network forms/restores, further incrementing the overall elasticity. All the aforementioned phenomena require the mobility of the particles, whose assembly is driven by attractive interparticle interactions. Nevertheless, if the viscosity of the fluid phase is too high or the dimensions of the particles and their aggregates are too large, the mobility of the filler is hindered and the viscoelastic moduli remain stable during time [Romeo et al., 2009].

The characteristic time for structural rearrangements of plate-like particles can be roughly estimated as the inverse of the rotary diffusivity of rigid disks:

$$D_{r0} = \frac{3k_B T}{4\eta d^3} \tag{3.1}$$

where η is the viscosity of the suspending medium and d the diameter of the disks. For the PS/clay system, D_{r0} is in the range $10^3 \div 10^4$ s, which is compatible with the

timescale for the growth of G' shown in Figure 3.2. For the PS/PMMA/clay system, where the filler is mostly trapped at the fluid-fluid interface, Equation 3.1 cannot be used. The latter, indeed, does not contemplate energetically costly structuring phenomena (detachment of the particles from the fluid-fluid interface, deformation/dragging of the drops) that are necessary to alter the overall rheological response. Consequently, the time stability of G' noticed in the PS/PMMA/clay samples at low Φ reflects the hindered mobility of the interfacially trapped platelets. Once the available fluid-fluid interface is saturated, the exceeding particles are free to rearrange in the host medium irrespective of its biphasic nature, thereby causing the elasticity growth detected for the samples at $\Phi > 0.93\%$ (see Figure 3.5).

The differences between the morphologies of the PS/clay and PS/PMMA/clay systems after the thermal aging are evidenced in Figure 3.7, where TEM images of

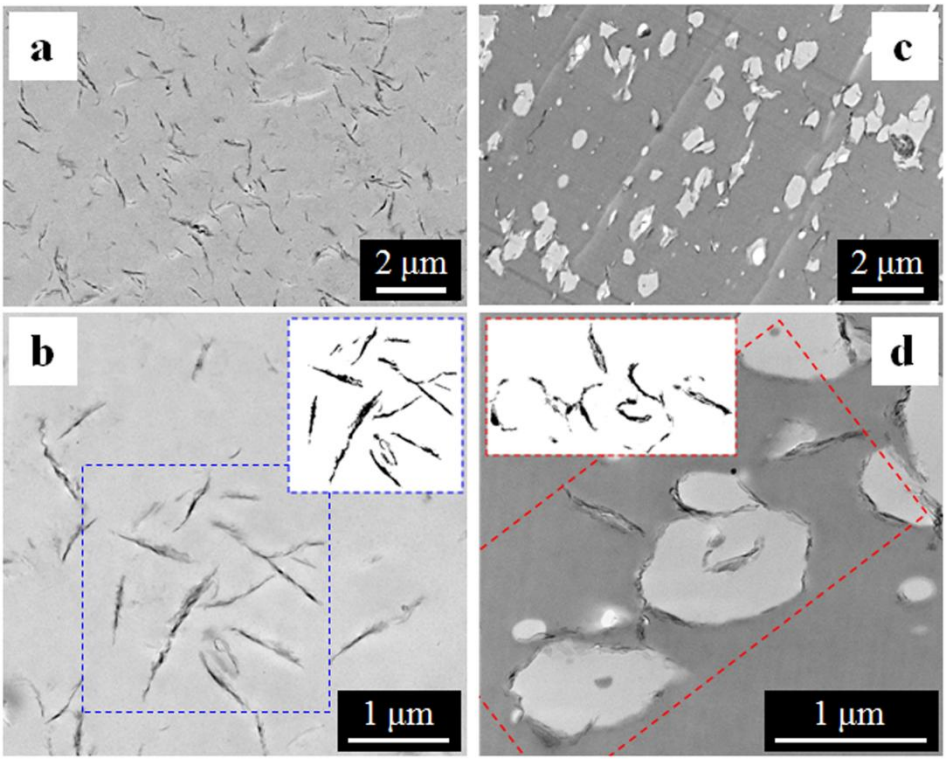

Figure 3.7 – TEM micrographs of the (a,b) PS/clay and (c,d) PS/PMMA/clay at Φ =1.32% after aging. The structures of the flocs highlighted in the high-magnification images are shown in the insets after the removal of the background fluids.

of samples at Φ = 1.32% are reported. At this filler content, both samples exhibit a comparable low-frequency plateau of G'. In the PS/clay sample, the tactoids are randomly suspended in the host matrix; the considerable lateral dimensions of such structures are due to hydroxylated edge-edge interactions between silicate layers [Ray et al., 2003]. The random assembly of the filler results in micron-sized flocs, which in turn form a three-dimensional, space-filling network. In the PS/PMMA/clay sample, large portions of the matrix are devoid of nanoparticles, which mostly adhere at the surface of the drops (imparting them highly irregularly shapes) or are trapped within drop clusters. Nonetheless, looking at higher magnifications (see Figure 3.7d), long-range connectivity of the particles can be noticed also in the PS/PMMA/clay sample. The main difference with the PS/clay system is that in the blend the particle flocs embed and connect the PMMA domains (either clay-coated drops or drop clusters).

3.4.2 Elasticity of the filler networks

Due to the similar rheological responses of the two systems at relatively high filler content, the contributions of the particles and the matrix have been studied by means of a recently proposed two-phase model [Filippone and Salzano de Luna, 2012]. The latter, conceived to describe the linear viscoelasticity of homopolymer-based nanocomposites above Φ_c, is based on the coexistence of two independent populations of dynamical species: (*i*) a fraction of free polymer, which encompasses the viscous feature of the system and whose dynamics are not affected by the filler; (*ii*) a three-dimensional network based on flocs of nanoparticles, which is responsible for the marked elasticity detected in the low-frequency range. When the suspending medium is a biphasic fluid, an additional contribution arises at low frequency because of the interfacial elasticity. Nevertheless, since the latter is not so relevant to invalidate the assumption that the elasticity of the nanocomposite is entirely related to the filler network, the model is applicable to both PS/clay and PS/PMMA/clay systems. The $G'(\omega)$ plots of nanocomposites at different $\Phi > \Phi_c$ can be then scaled on a single master curve to demonstrate the independency of the responses of the different phases.

The procedure for building the master curve of G' is reported in detail in various papers [Filippone et al., 2010c; Filippone et al. 2012; Filippone and Salzano de Luna, 2012], and the key steps are summarized hereinafter. The first step consists in evaluating the hydrodynamic effect related to the presence of the filler by introducing an amplification factor $B(\Phi)$, originally proposed for non-Newtonian

fluids filled with microparticles [Gleissle and Hochstein, 2003]. For polymer nanocomposites, $B(\Phi)$ represents the ratio between the complex moduli of the filled sample and the neat matrix in the high frequency range. The matrices to consider are, respectively, pure PS for the PS/clay system and the unfilled PS/PMMA blend for the PS/PMMA/clay one. The second step consists in identifying the horizontal (a_Φ) and vertical (b_Φ) shift factors for the scaling of the G' curves. These factors are defined as the coordinates of the points where the amplified viscous modulus of the neat matrix, $B(\Phi)\times G''(\omega)$, equals the low-frequency plateau of the elastic modulus, $G'_0(\Phi)$.

The previous procedure only applies to samples above the percolation threshold, which should be identified first. Actually, the physical constraints of the two-phase model allow to reliably identify the samples which exceed Φ_c: once the master curve has been built by referring to samples with a clear low-frequency plateau, the scalability of the G' curve of a sample at lower Φ unequivocally certifies the crossing of Φ_c. The hydrodynamic and shift factors for the studied systems are reported in Table 3.3; all these quantities are found to monotonically increase with increasing filler volume fraction.

Table 3.3 – Hydrodynamic and shift factors of each scaled G' curve of Figures 3.3 and 3.6. Adapted from [Filippone et al., 2014] with permission of the Royal Society of Chemistry.

	Φ [%]	$B(\Phi)$	a_Φ [rad s^{-1}]	b_Φ [Pa]
PS/clay	0.94 ± 0.07	1.126	0.004	13.6
	1.10 ± 0.01	1.153	0.012	42.7
	1.27 ± 0.05	1.185	0.025	88.3
	1.32 ± 0.08	1.194	0.051	171.5
	1.63 ± 0.01	1.256	0.223	812.7
	1.89 ± 0.10	1.313	0.332	1256.3
	2.65 ± 0.01	1.500	0.454	1942.2
PS/PMMA/clay	1.32 ± 0.03	1.227	0.024	94.8
	1.66 ± 0.04	1.321	0.044	185.0
	2.05 ± 0.11	1.448	0.113	525.7
	2.12 ± 0.03	1.472	0.143	674.3
	2.24 ± 0.08	1.518	0.157	763.3

The master curves of the PS/clay and PS/PMMA/clay systems are shown in Figure 3.8. In both cases the collapse of the moduli is satisfactory over about three decades of low scaled frequencies, which demonstrates the effectiveness of the two-phase model even in case of biphasic polymer matrices. The non-superposing tails at high dimensionless frequency ω/a_Φ reflect the dynamics of the unfilled matrices (whose relaxation spectrum is independent of Φ), so their presence does not invalidate the consistency of the scaling. Surprisingly, as shown in the inset of Figure 3.8, the two systems approach the plateau at low ω/a_Φ with the same trend.

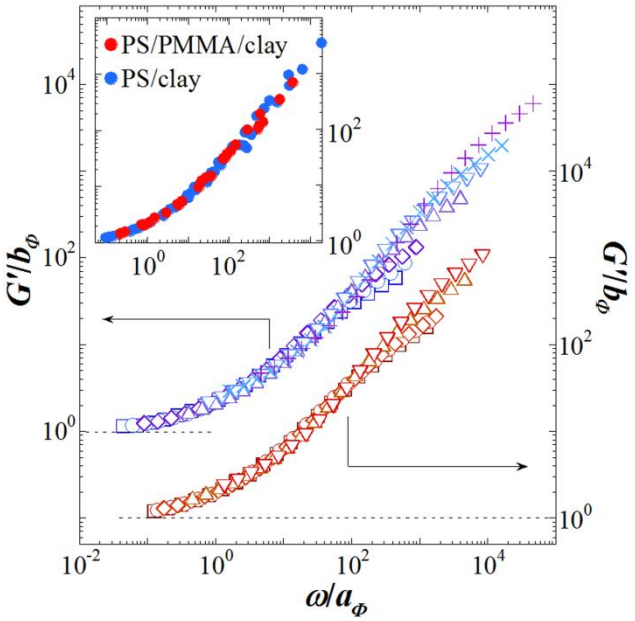

Figure 3.8 – Master curves of G' for the PS/clay (upper curve, left axis) and PS/PMMA/clay systems (lower curve, right axis). Symbols are the same as in Figure 3.3 and 3.6. The inset shows a detail of the overlay of the two master curves; only one of three points is reported. Adapted from [Filippone et al., 2014] with permission of the Royal Society of Chemistry.

At $\omega/a_\Phi >> 1$ the behaviour is governed by the matrix. Since the fastest relaxation modes of the PS/PMMA blend are essentially those of its predominant PS phase, the overlay at high ω/a_Φ is not unexpected. The superposition at $\omega/a_\Phi \sim 1$ is more surprising. In this intermediate frequency range, the network- and polymer-phase equally contribute to the elasticity of the system. Actually, the contributions of the

two phases are not merely additional. Moreover, the polymer-phase of the PS/PMMA/clay system exhibits an additional elastic connotation due to the interface between the polymers. The complex interplay among the various sources of elasticity complicates the discernment of the various contributions. Nonetheless, the main elastic features of the filler network are not affected by the presence of PMMA drops embedded in it. Hence, the structure of the particle networks in both the PS/clay and the PS/PMMA/clay samples can be studied using the same approaches employed for particulate gels in homogeneous fluids.

A quantitative comparison between the structures of the networks that form in the mono- and biphasic matrices can be performed by referring to the percolation theory. The latter predicts the network elasticity to grow with Φ as

$$G'_0 \sim (\Phi-\Phi_c)^v \tag{3.2}$$

the exponent v being related to the stress bearing mechanism [Stauffer and Aharony, 1992]. The previous equation is fitted to the experimental data of G'_0 for different possible values of Φ_c; the percolation threshold is thus taken as the one that returns the highest regression coefficient R^2.

The advantage of using the two-phase model is double: first, Φ_c can be sought in a restricted composition range, whose inferior limit is the highest Φ of the non-scalable G' curves; second, the values of G'_0 to be fitted can be accurately estimated even for samples whose network is too weak to cause the actual arrest of the relaxation dynamics. In this case, G'_0 is usually estimated presuming a plateau value of G' at frequencies much lower than those actually investigated. Such an extrapolation procedure, however, may result in non-trivial errors in the estimation of both Φ_c and v. Any conjecture can be avoided by referring to the master curve, whose vertical shift factors b_Φ exactly correspond to the elasticity of the filler network G'_0 [Filippone et al., 2012].

The results of the fitting procedure are shown in Figure 3.9, and the corresponding parameters are summarized in Table 3.3. The higher value of Φ_c found for the PS/PMMA/clay system is ascribed to the PMMA drops, which gather the tactoids and restrict their allowed space configurations. It is worth noting that the percolation threshold of the blend approximately coincides with the critical filler content above which the elasticity of the samples begins to increase over time (see Fig. 3.5b). Such a finding upgrades the picture emerged from the analysis of the time sweep experiments: after the saturation of the polymer/polymer interface, the added particles possess sufficient mobility to rearrange in the reduced volume outside the coated drops, easily connecting them to form a space-spanning filler

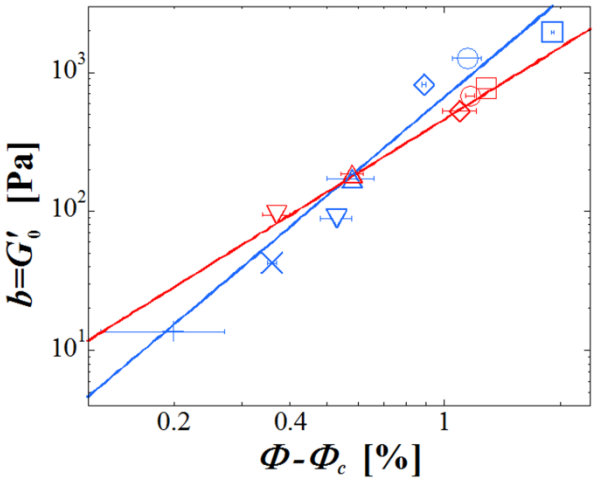

Figure 3.9 – Power-law dependence of the network elasticity on the reduced filler content for the PS/clay (blue) and PS/PMMA/clay system (red). Symbols are the same as in Figure 3.3 and 3.6. Adapted from [Filippone et al., 2014] with permission of the Royal Society of Chemistry.

network that embeds the PMMA phase. The values of the critical exponent ν for both the PS/clay and PS/PMMA/clay systems are consistent with various previously characterized polymer nanocomposites [Filippone and Salzano de Luna, 2012].

Table 3.3 – Percolation threshold and fitting parameter of the percolation law for the PS/clay and PS/PMMA/clay systems. Data taken from [Filippone et al., 2014] with permission of the Royal Society of Chemistry.

	Φ_c [%]	k [Pa]	ν
PS/clay	0.76	656 ± 26	2.34 ± 0.36
PS/PMMA/clay	0.95	457 ± 5	1.73 ± 0.17

3.4.3 Structure of the filler networks

The elasticity of the network in the biphasic matrix is less dependent on the reduced filler volume $\Phi-\Phi_c$, which suggests a different structure of the filler network. Valuable information can be obtained considering that the stress transfer takes place across an elastic backbone of particle aggregates. Modelling a gel of

colloidal particles as a collection of fractal flocs, Shih and co-workers have developed a scaling theory that relates the elastic constant and the limit of linearity, γ_{cr}, of the network to the fractal dimension of the flocs [Shih et al., 1990]. Such properties are predicted to scale with the filler content as $G'_0 \sim \Phi^A$ and $\gamma_{cr} \sim \Phi^B$. The exponents A and B, which are functions of the fractal dimensions of floc (d_f) and floc backbone (x), depend on the stress bearing mechanism: in the so-called strong-link regime the network elasticity is dominated by the inter-floc links, whereas in the weak-link regime the intra-floc elasticity governs the mechanical response. Attempts to apply the Shih's model to polymer/clay nanocomposites have led to reasonable values of d_f, but physically unacceptable values of x, which should be higher than unity to ensure the connectivity of the network [Durmus et al., 2007; Vermant et al., 2007]. Taking for granted the latter requisite, Wu and Morbidelli have envisaged intermediate situations by introducing a third parameter α ranging between 0 (strong-link) and 1 (weak-link) [Wu and Morbidelli, 2001]. For three-dimensional systems the expressions of the exponents A and B become

$$A = \frac{\beta}{3 - d_f} \tag{3.3}$$

$$B = \frac{3 - \beta - 1}{3 - d_f} \tag{3.4}$$

where $\beta = 1+(2+x)(1-\alpha)$.

The model by Wu and Morbidelli is used here to go deeper into the analysis of the two kinds of networks which form in the PS/clay and PS/PMMA/clay samples. Strain sweep experiments at ω = 0.1 rad s^{-1} have been performed to estimate the values of γ_{cr}, conventionally set as the strain at which logG' decreases by about 5% with respect to its low-strain plateau value. The log-log plots of G' as a function of γ are shown in Figure 3.10; both the PS/clay and PS/PMMA/clay systems exhibit the so-called Payne effect, i.e. a decrease of the limit of linearity with increasing filler content [Payne, 1965]. As established by the model of Wu-Morbidelli and shown in Figure 3.11, the power-law exponents A and B have been obtained by fitting the data at $\Phi \geq 1.10\%$ for the PS/clay samples and $\Phi \geq 1.32\%$ for the PS/PMMA/clay ones, i.e. well above the percolation thresholds.

The fitting parameters, computed assuming a reasonable value of the tortuosity of the network x = 1.3, are summarized in Table 3.4. Note that the results would be essentially the same by assuming values of x other than 1.3, and yet greater than 1.

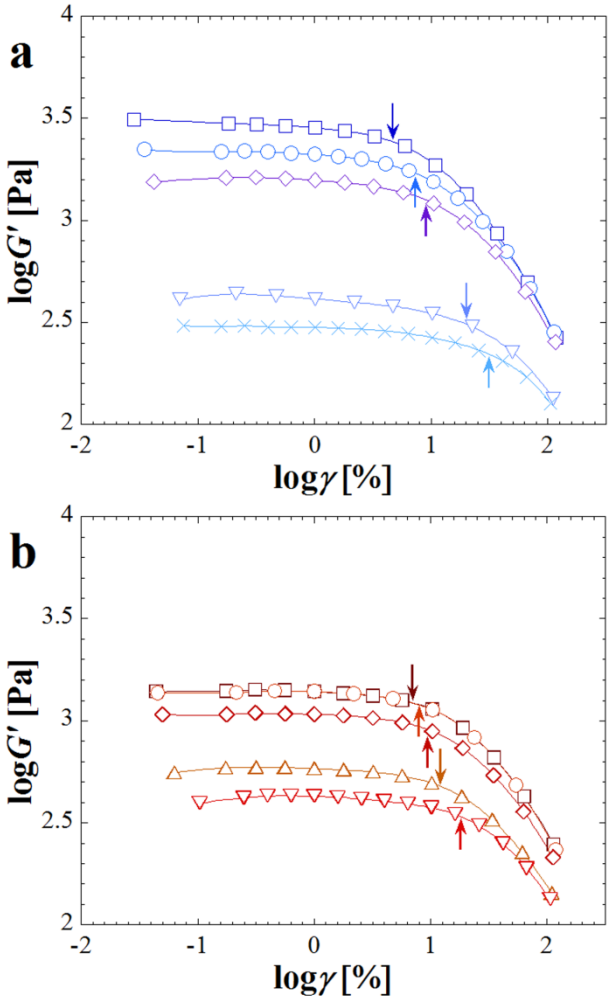

Figure 3.10 – Log-log plots of the strain-dependent G' for (a) the PS/clay samples at Φ = 1.10%, 1.27%, 1.63%, 1.89% and 2.65%, and (b) the PS/PMMA/clay samples at Φ = 1.32%, 1.66%, 2.05%, 2.12%, 2.24% (from bottom to top). The abscissae of the points indicated by the arrows are the estimated values of γ_{cr} on logarithmic scale. Adapted from [Filippone et al., 2014] with permission of the Royal Society of Chemistry.

The estimated fractal dimensions of the flocs in the PS/clay and PS/PMMA/clay systems are predicted to be almost the same, or a bit lower, than what reported in the literature for clay-based networks [Durmus et al., 2007; Vermant et al., 2007].

To corroborate the predictions of the model of Wu and Morbidelli, image analysis has been performed on various sections of flocs identified in several TEM

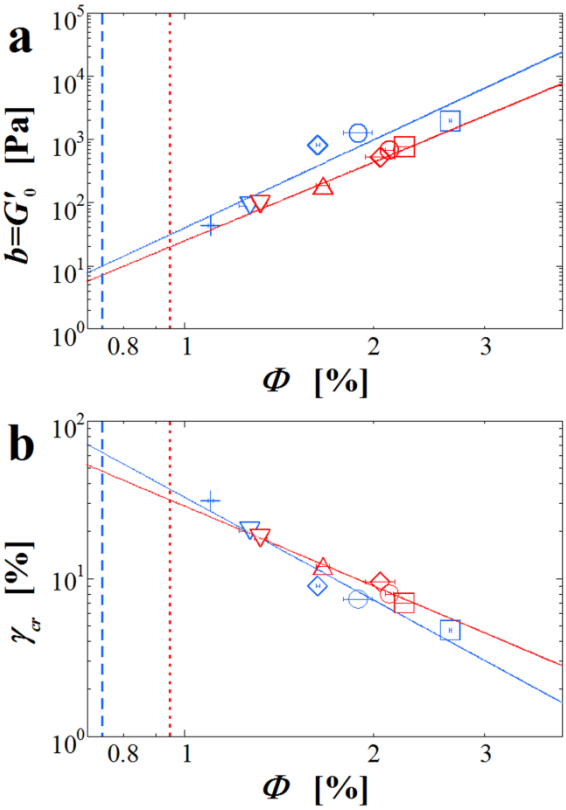

Figure 3.11 – (a) Network elasticity and (b) limit of linearity as a function of Φ for the PS/clay (blue) and PS/PMMA/clay (red) systems. Symbols are the same as in Figure 3.3 and 3.6 Solid lines are the power law fitting curves. Dashed and dotted lines indicate the percolation thresholds of the PS/clay and PS/PMMA/clay system, respectively. Adapted from [Filippone et al., 2014] with permission of the Royal Society of Chemistry.

micrographs. The main steps of such analysis are: image pre-processing (to isolate the pixels associated with the flocs); floc identification (assuming that two tactoids belong to the same floc if their minimum distance is lower than 100 nm); fractal analysis. A detailed description of the image processing procedure is reported in Appendix A.3, and an example of the outcome of the procedure is shown in Figure 3.12. The number of square boxes containing more than a certain fraction of mass, i.e. a fraction of black pixels in the binarized image, N_{BOX}, is reported as a function of the box size, L_{BOX}, in a log-log plot. The opposite of the slope represents the 2D box counting fractal dimension, D_f. The data reported in table 3.4 are the average values over about fifteen flocs, taken from several TEM micrographs.

Table 3.4 – Fractal dimension d_f, parameter α of the model by Wu & Morbidelli, and 2D box counting fractal dimension D_f for the PS/clay and PS/PMMA/clay systems. Data taken from [Filippone et al., 2014] with permission of the Royal Society of Chemistry.

	d_f	α	D_f
PS/clay	2.19 ± 0.01	0.16 ± 0.01	1.36 ± 0.06
PS/PMMA/clay	2.17 ± 0.08	0.28 ± 0.01	1.28 ± 0.08

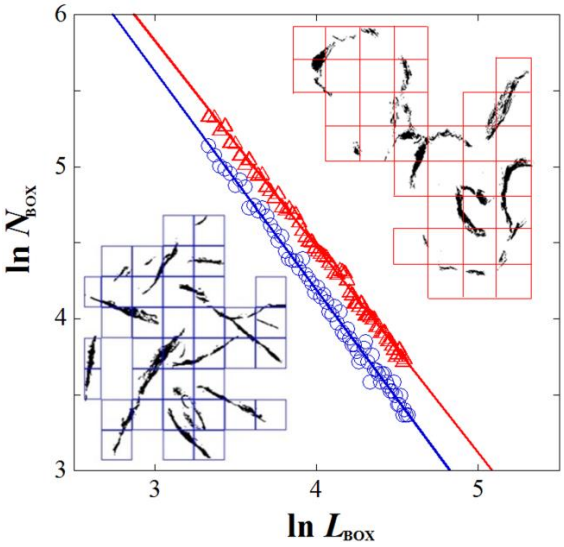

Figure 3.12 – Example of evaluation of the 2D box counting fractal dimensions, D_f. The number of square boxes which contain more than a certain fraction of mass is shown as a function of grid caliber. D_f is the slope of the linear regressions (solid lines). The insets show an example of grids with box size L_{BOX} = 20 pixels, corresponding to ~250 nm. Adapted from [Filippone et al., 2014] with permission of the Royal Society of Chemistry.

Also the values of D_f of the two systems are comparable, which corroborates the prediction of the Wu-Morbidelli model. Image analysis confirms a slightly lower fractal dimension of the flocs in the biphasic matrix, but the computed values of D_f are too close to be interpreted as a clear sign of a more opened structure. On the other hand, a subtle and yet statistically significant difference emerges when comparing the values of α. This parameter quantifies the relative importance of inter- and intra-floc links. Both systems exhibit values of α close to the extreme of the strong-link regime, which means that the flocs are on the whole quite soft,

behaving as weak springs. However, the comparison indicates that the flocs in the PS/PMMA/clay system are a bit stronger, or alternatively the inter-floc links are a bit weaker. The first possibility might reflect some extra elasticity of the drops and drop clusters in which the flocs are embedded; this contribution, which has revealed to be negligible when modeling the viscoelasticity of the nanocomposite, could stiffen the flocs as little as needed to slightly unbalance the system towards the weak-link regime. On the other hand, the clay stacks lying on the surface of the PMMA drops form curvy flocs. The latter could interact among them more weakly than in the PS/clay systems, in which hydroxylated edge-edge interactions are more likely to occur. In any case, it is interesting to remark the agreement with the picture given by Shih and co-workers. In the strong-link the individual flocs are allowed to grow freely from low particle concentration, which is congruent with what happens in a system without the constraint of the polymer-polymer interface such as our PS/clay. On the other hand, in the weak-link regime the network forms at higher particle concentration involving smaller and stronger flocs. It is logical to expect similar features in the PS/PMMA/clay system, where the drops anchor the particles and provide additional elasticity to the flocs.

3.5 Nanoparticle-induced alteration of blend phase inversion

As already pointed out in §2.1, in binary blends immiscibility often brings about distributed morphologies, where domains of one phase are dispersed in the second constituent. Co-continuous morphologies, where both phases are continuous and interpenetrated, can be instead obtained within a narrow range of compositions and/or using appropriate processing expedients. A well-established technique for the detection of co-continuity is the selective removal of that phase from the sample using an appropriate solvent [Galloway and Macosko, 2004]. Monitoring the change in mass during the extraction process allows to estimate the degree of continuity of phase *i*

$$\varphi_i = \frac{m_{i,0} - m_{i,f}}{m_{i,0}} \tag{3.5}$$

where $m_{i,0}$ and $m_{i,f}$ represent the masses of component *i* present in the sample at the beginning and at the end of the extraction, respectively.

Aiming to probe the ability of nanoparticles to affect the transition from distributed to co-continuous morphology in multiphase systems, extraction

experiments have been conducted on PS/PMMA blends with different compositions, both unfilled and clay-filled (clay/PMMA weight ratio equal to 0.02). For a specimen of unfilled blend at 35 wt% of PMMA, having a diameter of 25 mm and a thickness of ~ 4.5 mm, the estimated degree of PMMA continuity is about 0.3. To check such result, SEM observations have been performed on representative surface and edge regions of the sample after solvent extraction, as shown in Figure 3.13. A remarkable loss of dispersed domains is found at the sample surface, but the detail of the edge reveals the coexistence of regions where the solvent has penetrated and other that are inaccessible.

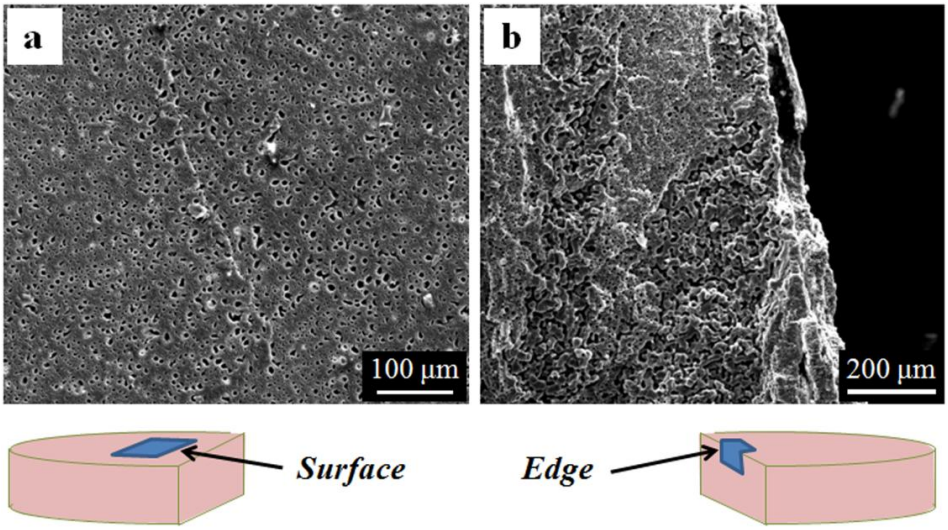

Figure 3.13 – SEM micrographs of (a) surface and (b) edge regions of a PS/PMMA sample at 35 wt% of PMMA and thickness ~ 4.5 mm.

The sensitiveness of solvent extraction experiments on sample size has been addressed by Galloway and co-workers [Galloway et al., 2004], who have highlighted that the measured degree of continuity is artificially increased by the dissolution of superficial domains. The fraction of extracted polymer that can be attributed to such domains decreases as the thickness of the sample (surface area per unit volume) increases. As a result, the degree of continuity is reduced, especially for blends with drop-matrix morphologies. Figure 3.14 shows all the results of solvent extraction experiments, reporting the degree of PMMA continuity as a function of blend composition for samples of different thicknesses. Besides highlighting a systematic increase of the degree of continuity with increasing the

amount of PMMA in the blend, the reported results reveal that the sample size effect is more remarkable in the filled samples than in the unfilled ones. This is clearly evidenced by a higher shift among the curves that retrace the variations of φ_{PMMA} with PMMA content for samples with different thicknesses.

According to Galloway and co-workers, the dependence of the degree of continuity on the sample thickness, *h*, is reliably modelable by a linear relationship

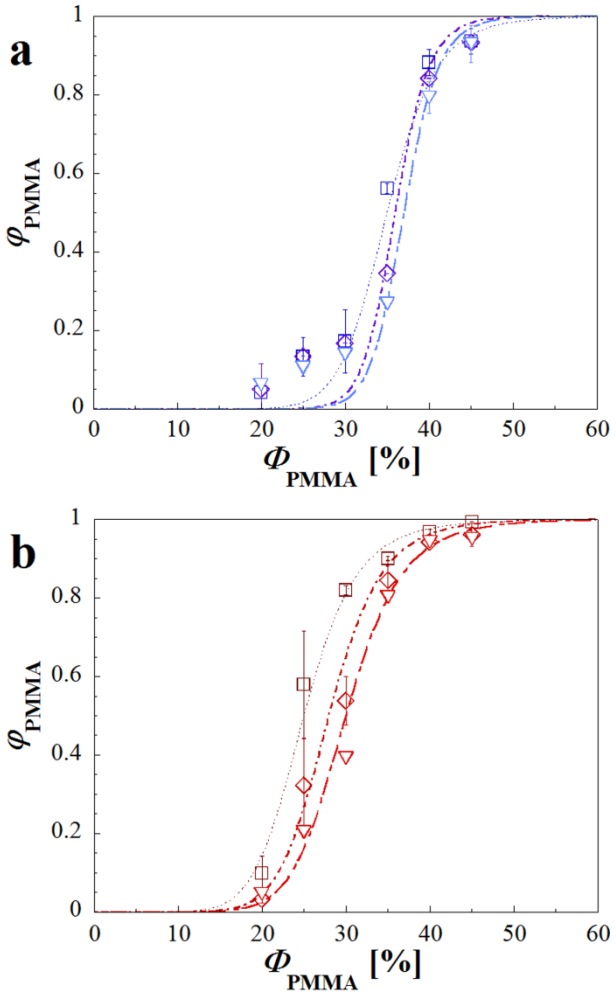

Figure 3.14 – Degree of continuity of PMMA as a function of PMMA weight content for (a) unfilled and (b) clay-filled PS/PMMA blends for samples of different thickness: 1.5 mm (squares), 3 mm (diamonds) and 4.5 mm (triangles). The lines are guides for the eye.

$$\varphi_i = m\left(\frac{1}{h}\right) + b \tag{3.6}$$

hence the experimental data can be corrected from the sample size effect by testing specimens with different surface-to-volume ratios and performing an extrapolation procedure that leads to the determination of the "bulk" degree of phase continuity φ. The latter, if the solvent penetration depth is small compared with extension of the sample, coincides with the intercept b. Figure 3.15 shows the degree of PMMA

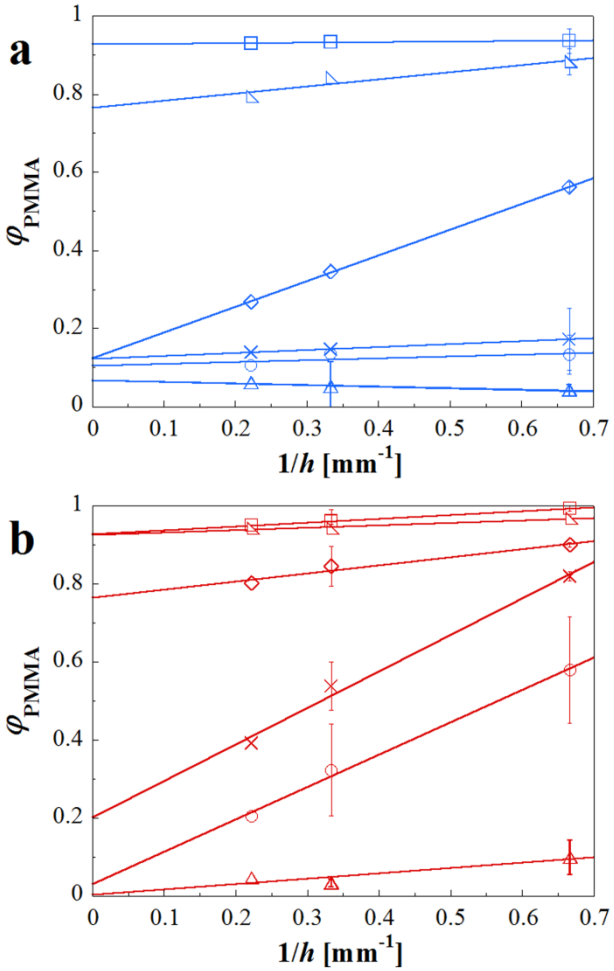

Figure 3.15 – Degree of continuity of PMMA as a function of the reciprocal of sample thickness for blends at different PMMA contents: 20, 25, 30, 35, 40 and 45% (from bottom to top). The data are fit according to Equation 3.6.

continuity as a function of 1/*h* for both the unfilled and filled blends. The analysis of the slopes of the fitting lines points out that the sample size effect appears to be more influential in the range of intermediate compositions, where phase inversion is expected to occur; on the other hand, it becomes more and more negligible as $\varphi_{PMMA} \rightarrow 1$, i.e. when the extracted phase is almost completely continuous.

The bulk degree of continuity of the PMMA, deriving from the correction of the experimental data, is reported in Figure 3.16 as a function of the PMMA weight fraction for the unfilled and filled systems. For PMMA contents lower than 25 wt%, φ is close to 0 in agreement with the expected drop-matrix morphologies for these compositions. For the unfilled blend, the sudden increase of the extractable fraction between 35 and 40 wt% of PMMA content is indicative of the onset of PMMA phase continuity. The addition of nanoparticles results in a reduction to 30÷35 wt% of the critical PMMA content for phase continuity. It is worth noting that for the unfilled blend containing 35 wt% of PMMA, shown in Figure 3.13, the bulk degree of PMMA continuity is slightly less than 0.1, while the experimental datum of φ_{PMMA} reported for the sample with thickness 4.5 mm is about 0.3. This comparison is emblematic of the artificial overestimation of the measured degree of phase continuity that is caused by the sample size effect.

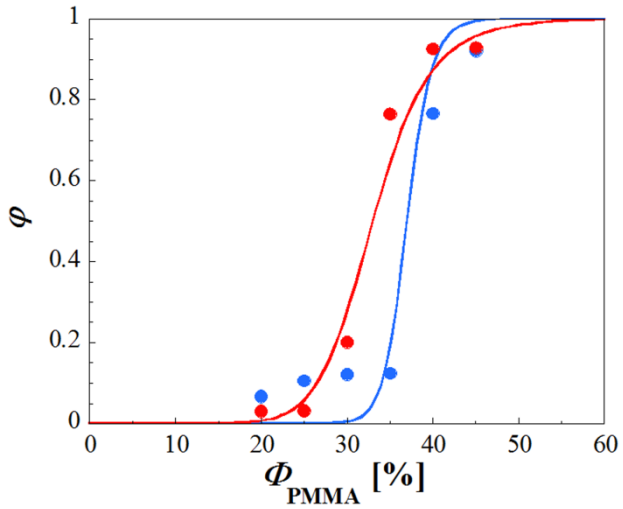

Figure 3.16 – Bulk degree of phase continuity of the PMMA as a function of the PMMA weight fraction in the blends: unfilled (blue symbols) and clay-filled samples (red symbols). The lines are guides for the eye.

The phase inversion composition for unfilled blends is basically related to the viscosity ratio of the blend constituents. However, the effect of the filler on the onset of co-continuity is reasonably relatable to modifications in the blend microstructure rather than viscosity changes. In order to support this hypothesis, morphological analyses have been performed. The SEM micrographs of Figure 3.17 show the surface and edge regions (identified as depicted in Figure 3.13) of unfilled and filled samples at 30 wt% of PMMA after the extraction experiments. Compared with its unfilled counterpart, the filled blend exhibits finer extracted domains on the surface and a greater number of elongated domains near the edge.

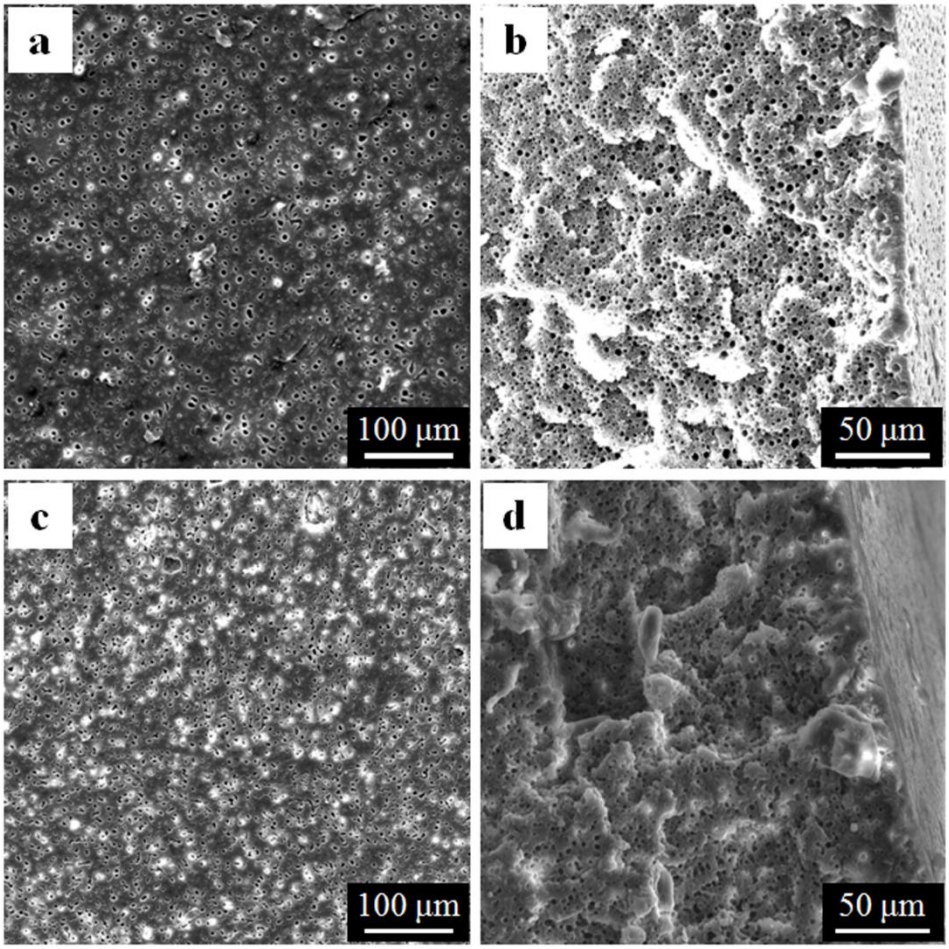

Figure 3.17 – SEM micrographs of (a, c) surface and (b, d) edge regions of (a, b) unfilled and (c, d) clay-filled PS/PMMA sample at 30 wt% of PMMA and thickness ~ 4.5 mm.

Some elongated PMMA domains can also be recognized in the "bulk" regions of the samples, shown in Figure 3.18. For both the unfilled and filled systems, the penetration of the solvent in the interior is limited due to the low surface-to-volume ratio of the observed specimens.

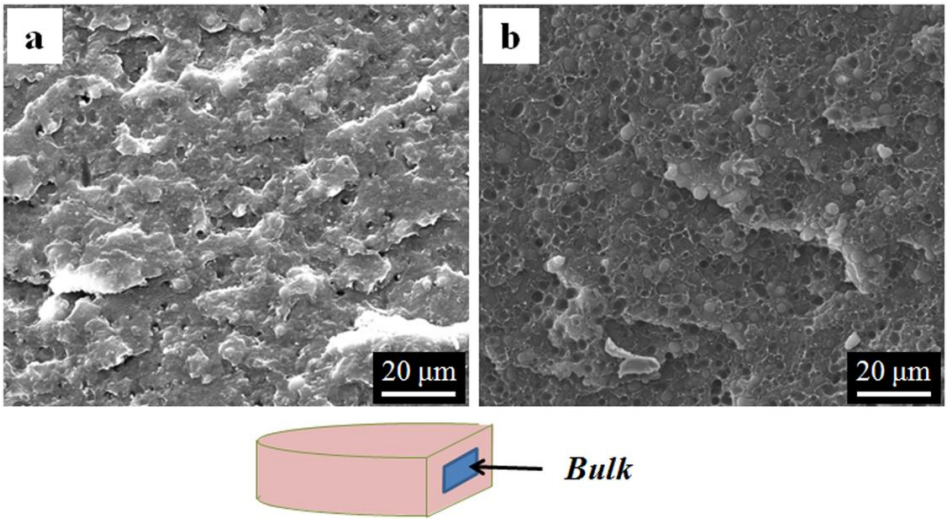

Figure 3.18 – SEM micrographs of the bulk (interior) regions of unfilled and clay-filled PS/PMMA sample at 30 wt.% of PMMA and thickness ~ 4.5 mm.

A clearer evidence of the morphological features of the filled system at 30 wt% of PMMA is given by the TEM micrographs of Figure 3.19a and 3.19b, taken from an as-extruded sample. Submicron- and micron-sized PMMA spheroidal droplets coexist with bigger, irregularly shaped structures. The latter derive from the clustering of distinct PMMA drops, which can be recognized due to the presence of clay platelets located on their surface (see inset of Figure 3.19b). Instead of coalescing into bigger domains, the pristine drops keep their individuality due to the bending stiffness of the particles, which stabilize energetically unfavorable morphological features, such as sharp corners or flat surfaces. The presence of drop clusters provides a reasonable explanation for the higher degree of PMMA interconnection detected in the filled blends with respect to the unfilled ones. The morphology of co-continuous systems at 45 wt% (Figure 3.19c and 3.19d) of PMMA exhibits a prevalence of large PMMA domains over isolated droplets. This is indicative that some coalescence of the PMMA domains occurs at high PMMA content.

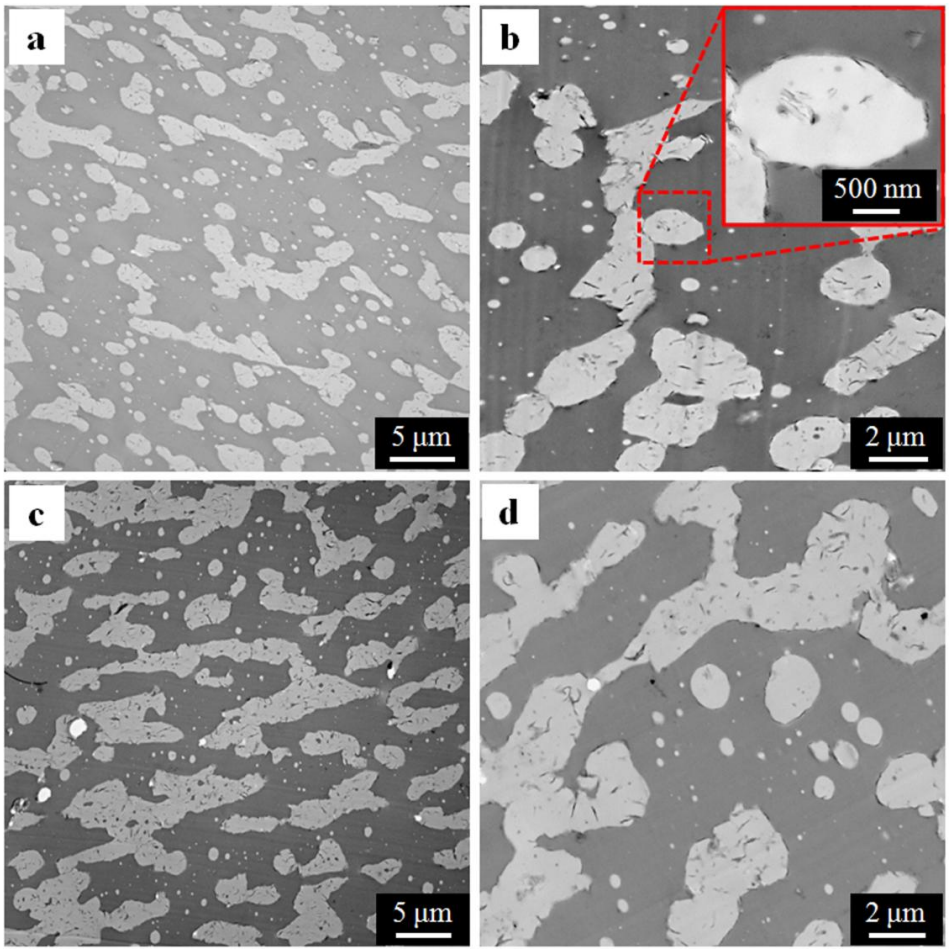

Figure 3.19 – TEM micrographs of the as-extruded PS/PMMA/clay at different PMMA contents: (a, b) 30 wt% and (c, d) 45 wt%.

In a recent paper, nanoparticle-induced drop clustering in PS/PMMA blends has been reported to occur in the course of prolonged slow flows [Filippone and Acierno, 2012]. Concerning the underlying mechanism, filler-induced bridging has been excluded as it involves the formation of a stable film between adjacent droplets, thus requiring a preferential wetting of the particles by the continuous phase. Indeed, as appreciable in Figure 3.19, the filler has a greater affinity with the PMMA phase, and no evidence exists of the presence of a continuous PS film between the clustered PMMA drops. The interfacial adsorption of nanoparticles and their influence on the interactions between the polymers is instead claimed to

play a major role in drop clustering. Indications about the van Waals interactions which establish between different phases can be inferred from the Hamaker constant of two bodies of a medium *i* that interact across a medium *j*

$$A_{iji} = \left(\sqrt{A_{ii}} - \sqrt{A_{jj}}\right)^2 \tag{3.7}$$

where

$$A_{ii} = 24\pi D_0^2 \gamma_i \qquad A_{jj} = 24\pi D_0^2 \gamma_j \tag{3.8}$$

are the Hamaker constants of two bodies of the same medium (either *i* or *j*) separated by vacuum ($D_0 \approx 1.65\times10^{-10}$ m) [Israelachvili, 1991]. In the systems studied here, the presence of the filler on the drop surface leads to a change in the value of A_{iji}, which has been estimated keeping PS as phase *j* and considering either PS or the organoclay as phase *i* [Filippone and Acierno, 2012]. The data reported in Table 3.5 reveal that the attractive forces between coated drops are found to be more than two orders of magnitude greater than between bare drops. Such a finding reflects the difference between the surface tension of the clay and those, similar between them, of the two polymers.

Table 3.5 – Hamaker constants at T = 190 °C for PS, PMMA, clay, and for PMMA and clay interacting across PS. Data taken from [Filippone and Acierno, 2012].

Parameter	Value [J]
$A_{\text{PS-PS}}$	5.85×10^{-20}
$A_{\text{PMMA-PMMA}}$	5.79×10^{-20}
$A_{\text{clay-clay}}$	4.70×10^{-20}
$A_{\text{PMMA-PS-PMMA}}$	1.60×10^{-24}
$A_{\text{clay-PS-clay}}$	6.30×10^{-22}

Apart from the clustering promoted by the interfacial segregation of the nanoparticles, the diverging shape relaxation time of the clay/coated interfaces is also believed to be crucial in inducing co-continuity. Indeed, it should prevent the interpenetrated morphology formed during melt mixing to evolve towards a distributed one driven by interfacial tension.

4

Nanoparticles as morphological modifiers in polymer blends – A strategy for improving the recyclability of plastics

The possibility of using inorganic nanoparticles to control the morphology of multiphase polymer systems has recently emerged as a feasible way to design high-performance formulations based on recycled plastics, hence providing sustainable alternatives to petroleum-derived materials. An intriguing opportunity in this sense is the minimization of the presence of multiple interfaces, which represent defect points in complex multiphase systems such as recycled co-mingled plastics, by driving the segregation of the polymer phases. In this chapter, after introducing current issues in polymer recycling (§4.1), some notable attempts to use clay nanoparticles to fulfill the technologically relevant objective of improving the recyclability of waste polyethylene terephtalate are presented (§4.2, §4.3).

4.1 Prefatory notes

The plastics market is currently dominated by petroleum-based products. The volumes are impressive: approximately 288 million tons of plastics have been produced worldwide only in 2012, and about 40% of this material has been introduced in the ecosystem as industrial waste products. As recently reported by PlasticsEurope, despite the financial crisis, the plastic production in Europe increased by 3.6% in the four-year period 2009-2012. Continuing to produce new plastic goods without taking into account the latest stages of their lifecycle has become simply unsustainable. Governments, companies and scientists are looking for alternatives to crude oil-based products. A feasible proposed solution is valorizing recycled petroleum-derived plastics to reduce their environmental impact due to low-degradation rates and noticeable carbon footprints during lifetime. Besides the environmental benefits, recycled plastics have gained

significant interest during the last decades also from an economical viewpoint, due to the increasing price of petroleum commodities.

Among the different recycling techniques, namely primary recycling, chemical recycling, energy recovery and mechanical recycling, the latter stands out as it can be performed by the same cost-effective machinery, such as extruders and mixers, used to produce plastic items via melt compounding. Nevertheless, one of the major bottleneck in the field of recycling of plastics is the separation and sorting of plastic waste into single components. Such a process is costly and sometimes impossible, and the plastic processors usually have to deal with blends containing multiple plastics of different compositions. To get an idea, the main constituents of municipal plastic waste streams are polypropylene (PP, 24.3%), low-density polyethylene (LDPE, 23.9%), high-density polyethylene (HDPE, 17.6%), polyethylene terephtalate (PET, 12.8%), polystyrene (PS, 6.6%) and polyvinyl chloride (PVC, 2.9%)[*]. Due to the immiscibility in the melt state of most polymers, reprocessing unsorted plastics of the waste stream leads to multiphase systems where the presence of multiple polymer/polymer interfaces (i.e. points where more than two polymers come into contact) would have a detrimental effect on both the final structural and functional properties. In the light of these considerations, and in spite of the improvements in the recycling rate of polymer wastes experienced in the last decades, it is not surprising that the use of recycled plastics is still marginal in comparison with the neat materials: the polymer with the highest recycled-to-virgin use ratio is LDPE (10%), while PVC and thermosets are not recycled at all [Mudgal et al., 2011].

As already pointed out in §2.4, using chemical compatibilizers to improve the interfacial adhesion in immiscible polymer blends is a strategy that suffers from scarce generalizability, since new compatibilizers need to be synthesized for each new mixture of polymers. Moreover, this approach is practically unfeasible when considering multiphase systems with uncertain composition, such as recycled co-mingled plastics, even if few attempts to add complex compatibilization systems to municipal plastic waste are reported [Luzuriaga et al., 2011]. A possible route towards the minimization of multiple interfaces has been recently proposed by Le Corroller and Favis, who have exploited polymer segregation and phase encapsulation to locate multiple phases within only one of two major phases [Le Corroller and Favis, 2012]. A five-component polymer blend with hierarchical phase structure and acceptable mechanical resistance has been designed, but the

[*] http://greennature.com/article2158.html (accessed on March 16th, 2015).

large-scale applicability of these concepts in the field of polymer recycling is far from being proved.

In the scenario depicted so far, there is definitely room for exploiting the nonspecific compatibilizing ability of nanoparticles to pursue a technologically relevant objective such as the development of value-added formulations based on recycled polymers. Up to now, most of the studies aimed to use small amounts of nanoparticles to improve the performances of recycled plastics have focused on thermoplastic homopolymers [Zare, 2013]. Meaningful results are those by Hamzehlou and co-workers, who have obtained comparable oxygen permeability of virgin and recycled PET filled with approximately 1 wt% of clay particles, and by Gao and co-workers, who have attained a twofold increase of the tensile strength and elongation at break of waste PP upon adding 3 wt% of carbon nanotubes [Hamzehlou and Katbab, 2007; Gao et al., 2011]. In all these works, the filler is used as a mere reinforcing agent; nonetheless, only few investigations centered on nanoparticle-driven morphologies in blends of recycled polymers are reported [Kerboua et al., 2010; Fang et al., 2013].

As a capitalization of the fundamental study described in Chapter 3, the intriguing opportunity to use nanoparticles to control the morphology and performances of blends of recycled polymers, thereby valorizing the latter, has been explored. This research activity is focused on formulations based on the most extensively recycled plastics. Hereinafter, some notable results are presented concerning binary and ternary polymer systems where PET ground from waste water bottles is dispersed in polyolefinic matrices: either PP or a cocontinuous HDPE/PP blend. Regarding the latter, an approach known as "reprocessing at low temperatures" has been pursued: compounding has been performed below the melting temperature of PET, which has therefore been used as a solid filler for the co-continuous polyolefinic matrix. Organically-modified clay platelets have been selected as nanometric filler due to their ability to adapt to polymer/polymer interfaces (as argued in Chapter 3) and influence the morphology of immiscible polymer blends even at low particle loadings. Two kinds of fillers with different surface chemistry have been used: Cloisite® 15A (C15A) and a more hydrophilic Cloisite® 30B (C30B).

The localization of the filler in the blends has been predicted on the basis of thermodynamic equilibrium considerations, the adopted procedure being analogous to that detailed in §3.3. Table 4.1 collects literature data of the surface tension and its dispersive and polar components for the polymers and the fillers at room temperature. These data have been used to estimate the various polymer/polymer

and polymer/filler interfacial tensions at the processing temperature It is helpful to remind that the lack of surface tension data for Cloisite® 15A is overcome by considering the values reported for Cloisite® 10A.

Table 4.1 – Dispersive and polar components of the surface tensions of the pure materials at room temperature (T = 20 or 25 °C) and temperature coefficients.

	Surface tensions at room T [mN m^{-1}]			$\partial\gamma_i/\partial T$ **[mN m^{-1} °C^{-1}]**
	γ_i	γ_i^d	γ_i^p	
HDPE	35.5 [a]	35.5 [a]	0 [a]	-0.062 [a]
PP	30.1 [a]	30.1 [a]	0 [a]	- 0.058 [a]
PET	44.6 [a]	9.0 [a]	35.6 [a]	- 0.076 [a]
C15A	45.2 [b]	33.4 [b]	11.8 [b]	- 0.136 [c]
C30B	61.6 [b]	44.6 [b]	17.0 [b]	- 0.162 [c]

[a] From http://www.surfacetension.de/solidsurface-energy.htm (accessed April 5th, 2013)
[b] From [Kamal et al., 2009]
[c] Estimated by [Picard et al., 2002]

HDPE and PP have been respectively purchased from Versalis and Carmel Olefins. The PET has been collected from waste water bottles, washed, granulated and dried. The fillers are organo-modified montmorillonites with different polarities, supplied by Southern Clay Products: less polar Cloisite® 15A (C15A) and more polar Cloisite® 30B (C30B). The PET and the fillers hav been dried overnight under vacuum at T = 90 °C before processing.

Blends at different compositions have been prepared by melt compounding the constituents in a co-rotating twin-screw extruder (15 mL Micro Compounder, DSM Xplore) under nitrogen atmosphere at temperature T = 240 or 270 °C, average shear rates of about 100 s^{-1} and residence time of 600 s. The extruded materials have then been compression-molded in the form of rectangular bars and thin sheets for the subsequent characterizations.

Differential scanning calorimetry has been performed under nitrogen flow using a Q20 DSC apparatus (TA Instruments). The samples have been first heated from room temperature up to 300 °C, then cooled down to 30 °C, and finally heated again. Each step has been performed at a rate of 10 °C min^{-1}.

The morphology of the samples at the micro-scale has been investigated using a scanning electron microscope Leica Stereoscan 420. The inspected surfaces have obtained through a brittle fracture in liquid nitrogen of compression-molded samples. A thin layer of gold has been sputtered onto the fracture surfaces before performing the observations.

Dynamic-mechanical analyses have been carried out using a Tritec 2000 DMA (Triton technology, UK). The bar-shaped specimens (size ~10 × 10 × 2 mm^3) have been heated at 2 °C min^{-1} from 25 °C up to T = 200÷260 °C, depending on the sample composition. The tests have been performed in single-cantilever bending mode at a frequency ω = 1 Hz and total displacement of 0.02 mm, which is small enough to be in the linear regime.

The tensile properties have determined at room temperature and humidity, according to ASTM test method D882, using an Instron machine (mod. 3600) with a load cell of 5 kN. The specimens have been cut from compression-molded sheets in the form of strips (size ~ 0.2 ×10 × 100 mm^3), tested at 25 mm min^{-1} up to a strain of 2% and then at to 50 mm min^{-1} until break. The Young modulus, tensile strength and elongation at break have been recorded. The reported data are the average values of the results of 8 tests per sample.

4.2 Morphology and thermo-mechanical behavior of clay-filled binary blends (PP/PET)

Using recycled PET in multiphase polymer formulations with prescribed morphology appears a promising strategy to valorize the high stiffness and thermal resistance of the recyclate. In line with this aim, preliminary investigations on a blend composed by PP and PET recovered from waste bottles have been performed; the selected PP/PET weight ratio is 75/25. Moreover, the effect the addition of small amounts (2 phr) of C15A clay particles has been addressed. The unfilled and filled blends and the pure polymers, used as reference materials, have been prepared via melt compounding at T = 270 °C. The surface tensions of the various components at the processing temperature are reported in Table 4.2, having been extrapolated from the data of Table 4.1 (under the assumption of a linear temperature dependence).

Table 4.2 – Dispersive and polar components of the surface tensions of the neat materials at T = 270 °C as obtained by linear extrapolation (using the data reported in Table 4.1).

	Surface tensions at T = 270 °C [mN m^{-1}]		
	γ_i	γ_i^d	γ_i^p
PP	15.6	15.6	0
PET	28.3	22.6	5.7
C15A	11.2	8.3	2.9

The values of the polymer/polymer and polymer/filler interfacial tensions (estimated from Equation 2.4 and 2.5), the wetting parameter (computed from Equation 2.3) and the spreading coefficients (calculated from Equations 2.6) are reported in Table 4.3. These data suggest a preferential localization of the clay particles at the PP/PET interface and a slightly higher affinity with PP.

Table 4.3 – Polymer/polymer and polymer/filler interfacial tensions, wetting parameter and spreading coefficients at the operating temperature T = 270 °C.

Parameter	Value [units]
$\gamma_{PP/PET}$	7.01 [mN m^{-1}]
$\gamma_{PP/C15A}$	4.07 [mN m^{-1}]
$\gamma_{PET/C15A}$	4.00 [mN m^{-1}]
ω_a	0.01 [-]
$\lambda_{PP/C15A/PET}$	- 1.06 [mN m^{-1}]
$\lambda_{C15A/PET/PP}$	- 6.94 [mN m^{-1}]
$\lambda_{PET/PP/C15A}$	- 7.08 [mN m^{-1}]

DSC measurements have been carried out to assess the impact of the particles on relevant thermal properties of the systems, such as melting and crystallization temperatures (T_m, T_c) and melting enthalpy (ΔH_m). The estimated values, listed in Table 4.4, remain essentially unchanged upon both blending and adding the filler.

Table 4.4 – DSC data for the various samples.

Sample	T_m [° C]		T_c [° C]		ΔH_m [J g^{-1}]	
	PP	PET	PP	PET	PP	PET
PP	164.7	-	118.6	-	73.6	-
PET	-	250.8	-	204.2	-	36.2
PP/PET	164.9	246.7	120.9	207.6	81.8	24.2
PP + C15A	164.7	-	118.6	-	69.9	-
PET + C15A	-	251.4	-	202.3	-	36.1
PP/PET + C15A	162.4	251.7	119.5	199.9	78.2	25.1

This might be indicative of a preferential positioning of the clay at the PP/PET interface. Entezam and co-workers have reported that the presence of C30B particles in a PP/PET blend results in increased the crystallization temperature and degree of crystallinity of PET and negligible alterations of the PP characteristics [Entezam et al., 2013]. Nonetheless, such findings are ascribed to the marked preference of C30B to locate inside the PET phase, where the filler can effectively act as a nucleating agent.

In spite of the marginal effect on the crystalline features of the polymers, the dynamic-mechanical analyses unequivocally show that the macroscopic behavior of the PP/PET blend is remarkably affected by the addition of the filler. The visual monitoring of the temperature scan for representative samples is reported in Figure 4.2. At 170 °C, the PP has already begun to melt and flex, and drips between the supporting clamps at about 200 °C. Conversely, PET still remains self-supporting at the end temperature of 240 °C. The dynamic-mechanical behavior of the unfilled blend is essentially governed by the matrix: the presence of PET is responsible for a moderate increase of the softening temperature in comparison with the melting point of PP. Instead, the filled sample keeps its structural integrity well above 200 °C, approaching the behavior of the minor PET phase. For sure, the filler by itself is not able to explain the observed effects. Indeed, tests performed on the filled PP and PET samples (not shown) have revealed that the clay does not significantly alter the behavior of the homopolymers. The outstanding enhancement of the softening temperature of the blend can be instead reasonably ascribed to the synergism between the intrinsic reinforcing action of the particles and some morphological modification promoted by them.

Similar effects have been reported by Filippone et al., who have succeeded in enhancing the low thermal performances of HDPE, LDPE and PLA by blending them with polymers with higher melting points, such as polyamides, and adding small amounts of clay particles [Filippone et al., 2010a; Filippone et al., 2010b; Nuzzo et al., 2014a]. In these cases, the improved thermal resistance has been ascribed to the formation of a continuous "scaffold" of the minor heat-resistant phase, promoted by the selective localization of the fillers inside the same phase or at the interface. Such an explanation would be also reasonable for the studied systems, but an *ad hoc* morphological characterization, targeted to verify the distribution of the particles inside the blend and the microstructures that form in their presence, is paramount in this sense. Even so, the presented results give evidence of the potential of controlling the morphology of polymer blends through nanoparticles to design high-performance formulations based on recycled plastics.

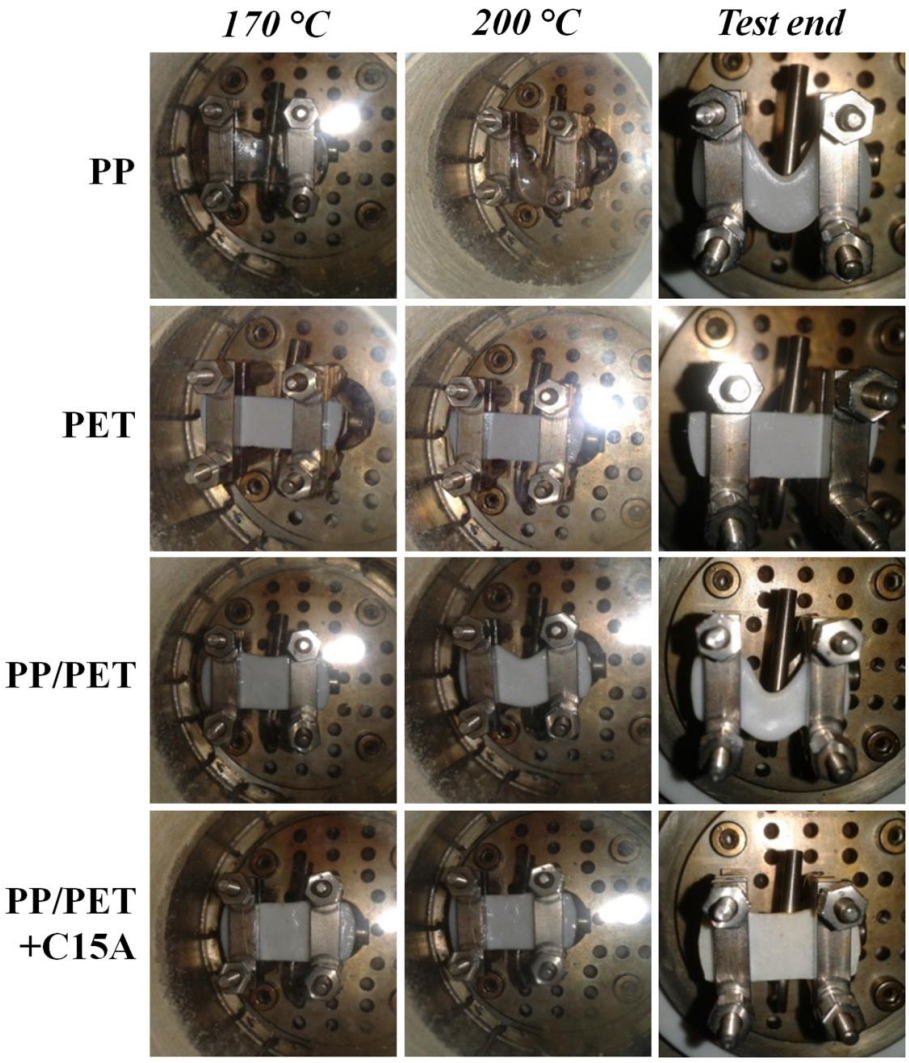

Figure 4.1 – Pictures of various samples during and at the end of dynamic-mechanical tests (end temperature: 200 °C for PP, 220 °C for PP/PET, 240 °C for PET and PP/PET+C15A).

4.3 Morphology and thermo-mechanical behavior of clay-filled ternary polymer blends (HDPE/PP/PET)

Another explored pathway to improve the recyclability of PET combines the exploitation of the compatibilizing effect of clay particles and an approach that is

commonly known as “reprocessing at low temperatures”. Specifically, a ternary polymer blend has been prepared using PET as a solid filler in a co-continuous polyolefinic matrix constituted by HDPE and PP. The samples, whose composition is indicated in Table 4.5, have been prepared at T = 240 °C, and the impact on the morphology and thermal properties of both C15A and C30B has been assessed.

Table 4.5 – Designation and composition of the samples.

Sample	HDPE [wt%]	PP [wt%]	PET [wt%]	Filler [phr]
HDPE	100	0	0	0
PP	0	100	0	0
PET	0	0	0	0
50/50/0	50	50	0	0
49/49/2	49	49	2	0
48/48/4	48	48	4	0
46/46/8	48	48	4	0
46/46/8 + C30B	46	46	8	0
46/46/8 + C15A	46	46	8	0.5

Table 4.6 reports the surface tensions of the polymers and the fillers at the processing temperature T = 240 °C, estimated using the data indicated in Table 4.1 under the assumption of a linear temperature dependence.

Table 4.6 – Dispersive and polar components of the surface tensions of the neat materials at T = 240 °C as obtained by linear extrapolation (using the data reported in Table 4.1).

	Surface tensions at T = 240 °C [mN m^{-1}]		
	γ_i	γ_i^d	γ_i^p
HDPE	21.9	21.9	0
PP	17.3	17.3	0
PET	30.3	24.2	6.1
C15A	15.3	11.3	4.0
C30B	25.8	18.7	7.1

Table 4.7 reports the values of the polymer/polymer and polymer/filler interfacial tensions, estimated from Equation 2.4 and 2.5, and the wetting parameter for the ternary polymer system, computed from Equation 2.3 considering PET as a solid filler. These data indicate that the location of the filler mainly depends on its polarity: indeed, the more polar C30B is preferentially wetted by the PET, whereas the less polar C15A has better affinity with the polyolefins. Moreover, the wetting parameter reveals a preferential positioning of PET inside the PP phase. This thermodynamic prediction is desirable in the view of minimizing the multiple interface, as pointed out in §4.1.

Table 4.7 – Polymer/polymer and polymer/filler interfacial tensions and wetting coefficient for the ternary polymer system at the operating temperature T = 240 °C.

Parameter	Value [units]
$\gamma_{HDPE/PP}$	0.52 [mN m^{-1}]
$\gamma_{HDPE/PET}$	6.17 [mN m^{-1}]
$\gamma_{PP/PET}$	7.20 [mN m^{-1}]
$\gamma_{HDPE/C15A}$	1.47 [mN m^{-1}]
$\gamma_{PP/C15A}$	1.14 [mN m^{-1}]
$\gamma_{PET/C15A}$	2.64 [mN m^{-1}]
$\gamma_{HDPE/C30B}$	7.05 [mN m^{-1}]
$\gamma_{PP/C30B}$	6.98 [mN m^{-1}]
$\gamma_{PET/C30B}$	0.43 [mN m^{-1}]
$\omega_{HDPE/PP/PET}$	1.96 [-]

The morphologies of the investigated systems are shown in Figure 4.2. The polyolefins in the unfilled blend are mutually interpenetrated, the PP appearing more compact and the rough texture of HDPE being indicative of its higher ductility. The PET forms micron-sized domains which, as predicted from wettability considerations, preferentially locate inside the PP phase. The different polarity of the clays, being responsible for their propensity to avoid the contacts with either the hydrophobic polyolefins or the hydrophilic PET, reflects itself in a varying influence of the filler on the morphology of the systems. The more polar C30B, which is expected to be preferentially wetted by the PET, has a negligible effect on the overall morphology of the blend. Conversely, the less polar C15A

appears to produce a significant refinement effect, reducing the characteristic size of the PET domains without altering the structure of the co-continuous matrix. Such an impact on the blend morphology may be ascribed to the confinement of the clay platelets at the interface between the PET domains and the polyolefinic matrix, which lets the filler act as a barrier to microstructural evolutions in the multiphase system.

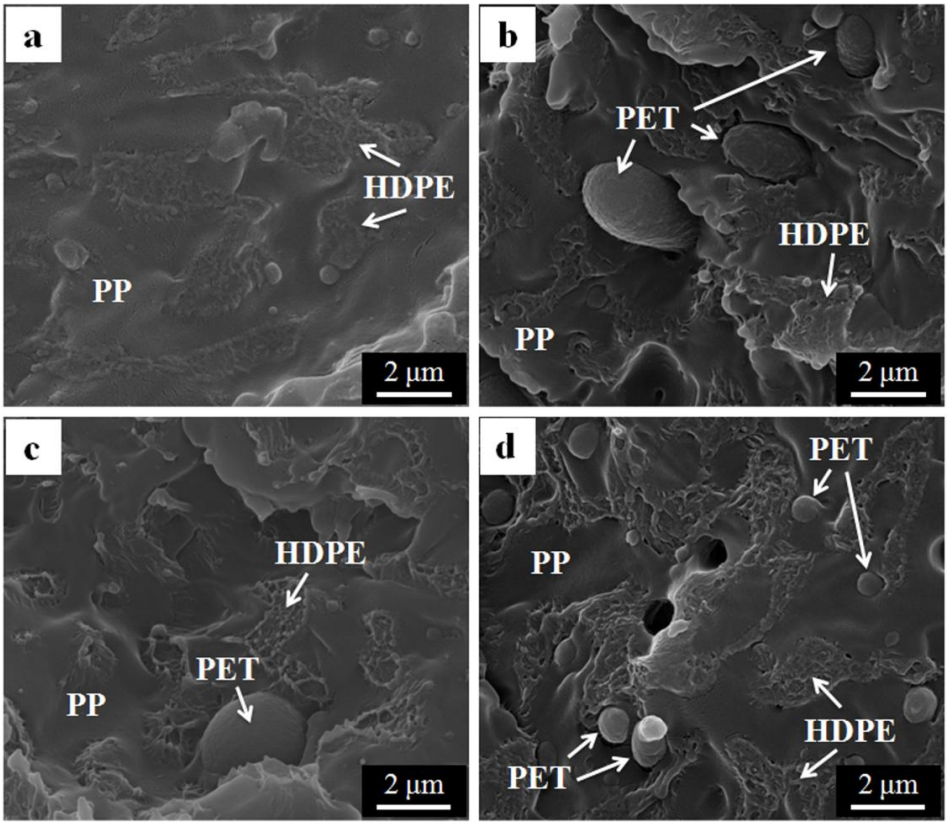

Figure 4.2 – SEM micrographs of the (a) 50/50/0, (b) 46/46/8, (c) 46/46/8+C30B and (d) 46/46/8+C15A blends.

The results of the dynamic-mechanical tests are shown in Figure 4.3. In particular, Figure 4.3a and 4.3b respectively point out the effects of the PET content and of the kind of filler on the storage modulus *E'* of the blends. In the 50/50/0 sample, the presence of PP enhances the modulus, which drops just above 120 °C in the neat HDPE. The mechanical behavior of the blends is not remarkably

affected by the presence of PET. As far as the filled blends are concerned, C30B does not produce relevant effects, while the increments of the elastic modulus at high temperatures are detected in the presence of C15A. Such improved high-temperature resistance can be reasonably related to to the morphology refinement promoted by the less polar filler.

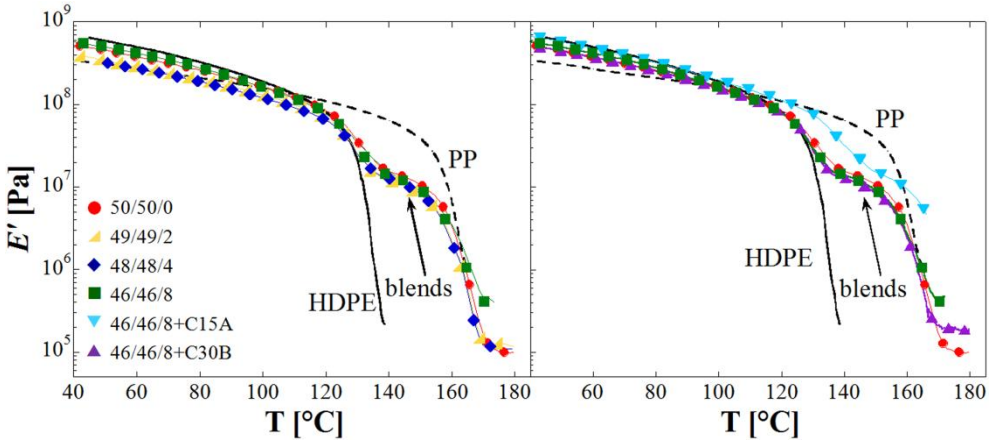

Figure 4.3 – *E'* versus *T* curves for the neat polymers and the unfilled and filled blends.

Table 4.8 reports the mechanical properties of the samples, namely Young modulus (E), ultimate tensile strength (σ_u) and elongation and break (ε_b), determined by means of tensile tests. HDPE exhibits a much higher ductility than PP, and the co-continuous polyolefin blend exhibits lower mechanical properties due to the poor interface adhesion. The presence of PET enhances the stiffness of the blends, causing restrained decreases of the other properties. Neither of the fillers significantly alters the tensile characteristics of the systems, confirming that the enhancing effect of C15A on the mechanical behavior of the blends becomes evident at higher temperatures. Such a conclusion is supported by some reported results, according to which the addition of small amounts of C15A to a HDPE/PP co-continuous blend has a negligible effect on its room-temperature stiffness and strength [Chiu et al., 2010].

To sum up, adding recycled PET as solid filler to a co-continuous HDPE/PP blend has resulted in restrained losses in the mechanical properties of the polyolefinic binary matrix. As evidenced by wettability considerations and morphological analyses, the PET preferentially locates inside the PP phase, thereby allowing to limit the issue of multiple interfaces. Concerning the effect of the filler

Table 4.8 – Tensile properties of the neat polymers, the unfilled and filled blends.

Sample	E [MPa]	σ_u [MPa]	ε_b [%]
HDPE	723 ± 78	907 ± 348	22.8 ± 1.7
PP	624 ± 74	14.3 ± 6.4	16.9 ± 1.9
PET	1318 ± 35	68.8 ± 4.0	10.6 ± 1.7
50/50/0	619 ± 50	13.3 ± 3.5	18.9 ± 0.8
49/49/2	652 ± 18	4.1 ± 0.7	13.5 ± 1.5
48/48/4	630 ± 4	15.5 ± 0.5	6.3 ± 0.9
46/46/8	870 ± 28	20.1 ± 5.5	8.5 ± 1.8
46/46/8+C15A	764 ± 41	18.1 ± 1.9	11.1 ± 0.9
46/46/8+C15A	871 ± 75	18.7 ± 1.0	7.9 ± 0.8

on the structure and properties of the ternary polymer systems, the more polar particles do not significantly alter the morphology of the blends, while the less polar ones appear to be more effective as a compatibilizer, promoting a refinement of the PET domains. Such an effect, ascribable to the likely positioning of the nanoparticles at the PET-matrix interface, is reflected by a considerable enhancement of the mechanical behavior of the blends at high temperature.

In the light of the discussed preliminary results, blending recycled plastics to other polymers and cleverly using nanoparticles to control the morphology of the resulting system appears as an economically and environmentally feasible route to give a new value to the aforementioned waste materials, improving their recyclability and taking advantage of their still exploitable properties.

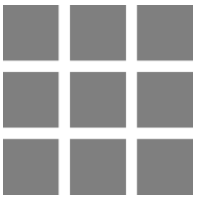

PART

II

Surface morphologies in solvent-cast systems

5 Phase separation induced morphologies in polymer films – Literature review

The immiscibility of polymers can be exploited to obtain not only multiphase materials with prescribed bulk structure and properties, but also polymer films with a wide range of surface morphologies. A typical route for film preparation consists in casting a drop of polymeric solution onto a solid substrate and letting the solvent evaporate to induce polymer precipitation. In the presence of two or more polymeric constituents, the evaporation of the solvent brings about phase separation processes that can be very different from that in bulk, being strongly influenced by surface effects at both the air/solution and solution/substrate interfaces. This chapter is intended to present the current state-of-the-art about the control of surface morphologies in polymer films. After evidencing the main material- and process-related factors that dictate the final surface structure of such flat systems (§5.1), a deep insight into the phase separation mechanisms during the casting process is offered (§5.2). Moreover, some meaningful examples are provided to shed light on the link between surface structure and performances of multiphase polymer films. Ultimately, as in the case of bulk systems, the morphological implications deriving from the incorporation of nanoparticles in polymer films are discussed (§5.3).

5.1 Formation of monophasic polymer films by solvent casting

The scientific interest in polymer films, stimulated by the new insights provided by the confinement of polymers in a flat geometry in comparison with bulk materials, dates back to the mid-twentieth century. From then on, polymer films have represented a matter of increasingly intensive research in physics, chemistry, engineering and materials science. The reason for such sustained growth in this field is the need for a fundamental understanding of the main factors that determine the characteristics of such two-dimensional systems: thermodynamic and kinetic

effects, interfacial interactions, flow and instability phenomena [Ramanathan and Darling, 2011].

Besides their scientific relevance, polymer films are widely used as industrial commodities (coatings, lubricants), and in advanced applications such as optoelectronics, biotechnology, nanolithography, and the development of novel sensors and actuators. For most of these purposes, the final material performances are dictated by the surface morphology of the film at different length scales (from few tens of nanometers to hundreds of micrometers) and the resulting topography.

Among the large variety of processes for film production, drop casting, dip coating and spin casting of polymeric solutions are commonly employed to prepare films with thickness ranging from few nanometers to several micrometers and desired surface characteristics and structure. In particular, drop casting is one of the most useful approaches for these purposes, as it is based on the simple deposition of a drop of solution onto a substrate followed by solvent evaporation at the air/solution interface. The removal of the solvent is even faster in spin casting, which envisages the rotation of the substrate and the consequent spreading of the drop driven by centrifugal forces. During evaporation, the polymer concentration increases until supersaturation is reached, eventually resulting in the precipitation of the polymer and the vitrification of the film structure [Young et al., 2002]. When designing a polymer film by means of such techniques, various aspects that could influence the final structure and surface features have to be taken into account. The wetting properties of the initial solution are among the most important factors: indeed, as highlighted by Neogi and co-workers in studies on polystyrene (PS) and poly(dimethylsiloxane) (PDMS), they affect the spreading dynamics of the drop onto the substrate and, ultimately, the extension and thickness of the film after the drying step [Nieh et al., 1996; Saritha et al., 2006]. The wetting properties of a polymer solution can be tuned by a judicious choice of the solvent, polymer concentration, and both surface chemistry and texture of the substrate, as well as the drop deposition method and the applied drying technology [Strawhecker and Kumar, 2001; Fukai et al., 2006].

Various investigations on the spreading and drying drops of colloidal suspensions and polymer solutions on solid surfaces have been recently carried out, aiming to control the shape of the deposit that remains on the substrate after the evaporation of the solvent [Neogi, 2001; Kajiya et al., 2006; Okuzono et al., 2009; Härth and Schubert, 2012; Bertola, 2013]. In general, the evolution of a droplet of polymer solution on a solid substrate is the result of an interplay between droplet spreading and solvent evaporation. After its deposition, the droplet spreads on the

substrate to reach the equilibrium wetting conditions. The subsequent evaporation of the solvent causes an increase of the solution viscosity near the edge which limits the further spreading of the droplet. In relatively dilute solutions, a commonly observed phenomenon is the "coffee stain" effect, reported for the first time by Deegan and co-workers [Deegan et al., 1997]. Solvent evaporation induces an outward flow, which brings the solute towards the perimeter of the droplet and creates a ring-like deposit after drying. Such outward flow ensues from the combination of the increased evaporation rate at the drop edge and the contact line pinning caused by solute deposition near the edge. Focusing on PDMS/heptane systems, Poulard and Damman have recently pointed out that the evolution of a drop of a dilute polymer solution on a wettable surface and the properties of the film remaining after solvent evaporation drastically depend on the solute/solvent interactions and, ultimately, on surface tension effects, polymer concentration and solution viscosity [Poulard and Damman, 2007]. Specifically, the polymer can flow inwards or outwards the solution drop depending on the difference in surface tension $\Delta\gamma$ between the solute and the solvent (Marangoni effect). If $\Delta\gamma > 0$, the "coffee stain" effect is observed, while for $\Delta\gamma < 0$ an inward flow occurs and the final polymer deposit is drop-shaped; in the case of similar surface tensions of solute and solvent, there is a lack of internal flow and a film of pure polymer with almost constant thickness forms. The width and stability of the rim that forms in case of outward flow have been found to increase with increasing either solution viscosity or polymer concentration.

Concerning semicrystalline polymers, the final structure and surface features of the film also depend on the nucleation and growth of polymer crystals. Polymer precipitation is a complex process that mainly depends on the chemical structure of the polymer, the evaporation rate of the solvent and the concentration of polymer in the pristine solution. For instance, an increase in the initial polymer concentration results in an increased solution viscosity, which affects the spreading of the drop onto the substrate. Moreover, for concentrated polymer solutions, the enhanced polymer supersaturation that occurs during the evaporation of the solvent accelerates the nucleation rate while the crystal growth rate decreases. As a result, the final morphology of the surface of the film is characterized by a high number of small crystallites [Ma et al., 2008]. A similar effect can also be achieved by increasing the evaporation rate of the solvent. In this case, the attained degree of polymer supersaturation increases and, concomitantly, the nucleation rate increases. The high density of produced nuclei limits their ability to grow before

impinging with neighboring domains, giving rise to crystallites of small size [Young et al., 2002].

Spherulitic surface morphologies are typically encountered in films of semi-crystalline polymers (both cast and crystallized from the melt) with thickness ranging from hundreds of nanometers to several micrometers. Generally, spherulites exhibit radial symmetry from a central point where the refractive index of the crystal in the radial and tangential directions are different from each other; hence, when the spherulite is observed with polarized light between cross polarizers, a so-called Maltese cross pattern of birefringence appears. During the spherulization process, which starts from nucleation points and proceeds with a radial growth up to the impingement of neighboring spherulites, the polymer chains align themselves in highly ordered crystalline lamellae. The latter are sandwiched with amorphous regions of semi-crystalline polymer, hence even fully spherulized structures may not be considered as completely crystallized. Other peculiar crystalline structures that may form for certain polymers and under specific conditions of film formation are fractals and dendrites, the latter being formed by highly-branched, short lamellae [Massa et al., 2003].

To conclude this overview of the formation of surface morphologies in homopolymer films, it is worth noting that in the case of ultrathin samples, whose thickness is below 100 nm, the deposition on a nonwetting substrate can cause dewetting phenomena. To attain thermodynamic stability, an initially uniform film may flow or deform, lowering its energy through the formation of holes. The latter then grow and coalesce, eventually breaking up the remaining network-like polymer structure into droplets [Ramanathan and Darling, 2011]. A more detailed discussion on ultrathin polymer films, however, goes beyond the scope of the present work. The influence of the presence of two or more polymer components on the development on the film morphology is the focus of the following section.

5.2 Formation of multiphase polymer films

The variety of surface morphologies characterizing solvent-cast polymer films is even broader when dealing with starting solutions that contain two or more polymers. In this case, the immiscibility of most macromolecular materials results in the occurrence of phase separation during the evaporation of the common solvent. While the mechanisms of phase separation of bulk polymer systems, reviewed in §2.1, have been thoroughly investigated, a lower level of

understanding has been reached in the case of polymer films: indeed, complex structures may form due to the presence of substrate/polymer and polymer/air interfaces [Geoghegan and Krausch, 2003].

The phase separation process, as well as the surface morphology and texture of the resulting multiphase polymer films, are very sensitive to various material- and process-related parameters: surface chemistry and texture of the substrate, composition of the starting solution (i.e. overall solute concentration and relative amounts of the polymers), solvent evaporation speed, polymer surface tension and solubility [Walheim et al., 1997; Dekeyser et al., 2004; Mokarian-Tabari et al., 2010]. At the two extremes, phase separation may exclusively take place either in the plane of the film or in the direction perpendicular to the plane of the film. The former phenomenon is named "vertical phase separation" and is generally related to the presence of a polymeric phase that is more affine to the casting substrate: such phase would tend to migrate towards the substrate interface. Alternatively, the component with lower surface energy can segregate to the film surface in order to minimize the energy of the system. As a result, a self-stratified film forms. The latter case is instead known as "lateral phase separation" and occurs if the polymers have similar surface tensions and affinities with the substrate [Heriot and Jones, 2005; Xue et al., 2012]. Phase separation during casting is characterized by the prevalence of kinetic factors over thermodynamics, due to the relatively rapid evaporation of the solvent; the resulting kinetically trapped morphologies can be driven to the equilibrium state by further annealing treatments (thermal or solvent vapour) [Ahn et al., 2012].

A mechanism for lateral phase separation has been proposed by Walheim and co-workers, who have focused on spin-cast binary and ternary films of amorphous polymers: PS, poly(methyl methacrylate) (PMMA) and polyvinylpyridine (PVP) [Walheim et al., 1997; Walheim et al., 1999]. After the deposition and spreading of a drop of the initial polymer solution onto the substrate, phase separation occurs as a consequence of the evaporation of the solvent at the air/solution interface. This results in the formation of coexisting phases of the different polymers, which are initially liquid due to the presence of large amounts of solvent. At this point, the surface of the sample is essentially smooth if the surface tensions of the phases are similar to each other. During solvent evaporation, polymer concentration progressively increases in each of the phases until supersaturation is reached, eventually leading to the precipitation of the polymer. The different polymeric phases solidify at different stages of the casting process, depending on the solubility of the polymers in the common solvent. The size and shape of the

domains and the topography of the resulting film are determined by the rate and sequence of polymer precipitation and the surface tensions of the constituents. The authors have highlighted that the earlier the polymer precipitation, the higher the domains; if the solvent is better for the polymer that has the lower surface energy, the surface structure exhibits sharp edges, otherwise a round topography is observed. The different steps of the process of lateral phase separation for a ternary polymer blend are depicted in Figure 5.1.

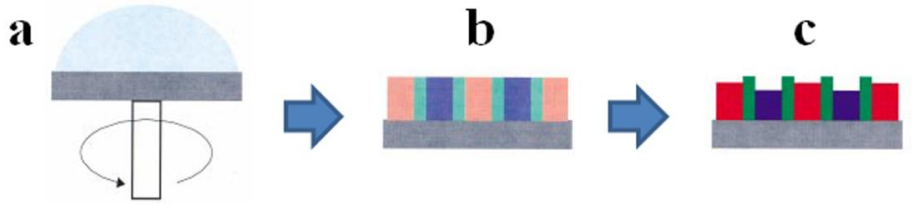

Figure 5.1 – Scheme of the mechanism of lateral phase separation for a spin-cast ternary polymer blend. At the beginning, the three polymers and the common solvent form a single phase (a). During the casting process, the solvent evaporates and phase separation takes place; at this point, the surface of the film is essentially smooth (b). Depending on their relative solubility, the three polymer phases contain different solvent concentrations and hence solidify at different stages. The less soluble polymer precipitates first (green), followed by a collapse of the more soluble components (red and blue) below the average height of the already formed domains (c). Adapted with permission from [Walheim et al., 1999], copyright 1999, American Chemical Society.

Based on the findings of Walheim and co-workers, Heriot and Jones have provided further insight into the mechanism of lateral phase separation, using small-angle light scattering and light reflectivity to directly monitor the morphological evolutions of a PS/PMMA system during spin casting from a toluene solution [Heriot and Jones, 2005]. According to the authors, after the removal of the excess solution at the start of spinning, phase separation takes place by the formation of a transient layered structure, due to the different affinities of the components with the substrate. As the solvent continues to evaporate, the film thins and instabilities develop at the interfaces between different phases, driven by solvent concentration gradients within the layers [Mokarian-Tabari et al., 2010]. Such interfacial instabilities eventually lead to the break-up of the layers into lateral domains. Phase separation then proceeds as described by Walheim and co-workers, with further solvent evaporation and the precipitation of the different polymers.

Observing the segregated surface morphology of the final PS/PMMA films, Heriot and Jones have highlighted that each major phase domain embeds small-scale inclusions (whose size is in the range $10^2 \div 10^3$ nm) of the other polymer constituent. The authors have then hypothesized the occurrence of a "secondary" phase separation (not directly detected) at some point during casting. Such phenomenon has been reported and described by Liu and co-workers for a blend of poly(ε-caprolactone) (PCL) and polyetherimide (PEI) [Liu et al., 2007]. Each of the liquid phases that form after the first separation stage contains a high amount of one of the polymers, while the other components are present at lower contents. The further evaporation of the solvent increases the viscosity of the solution and hinders the diffusion of the polymer chains. As a result, further separation phenomena occur in each liquid phase, the minor polymeric components forming domains over small length scales after precipitation.

When at least one of the polymer is semi-crystalline, the surface morphology and texture of the final multiphase film are also affected by the crystalline structure. For films of PMMA and poly(ethylene oxide) (PEO), Ferreiro and co-workers have observed a variety of morphologies as a function of the relative amounts of the polymers: crystalline PEO dendrites, seaweeds, fractals and spherulites separated by amorphous PMMA regions [Ferreiro et al., 2002a; Ferreiro et al., 2002b]. Focusing on a blend of poly(vinylidene fluoride) (PVDF) and PMMA, Narula and Pillai have pointed out that the PVDF spherulites become gradually less distinct with increasing PMMA content [Narula and Pillai, 1990]. Moreover, Ma et al. have highlighted that the surface morphology of a PVDF/PMMA blend at weight composition 70/30 is dictated by the crystalline structure of PVDF, likely because the latter has a low surface tension [Ma et al., 2008]. Concerning fully semi-crystalline blends, such as those formed by PCL and PEO, only few studies deal with the surface features of as-cast films, the majority being centered on the crystallization behavior of the phases during thermal annealing [Qiu et al., 2003; Huo et al., 2014].

To conclude this overview on multiphase polymer films, it is worth highlighting that important applications are emerging in which a thorough understanding and control of the process of phase separation would be highly desirable [Heriot and Jones, 2005]. Blends of semiconducting polymers can be used to manufacture efficient photodiodes and photovoltaic devices, owing to the importance of interfaces in the localization and separation of excitons [Halls et al., 1995; Moons, 2002; Peumans et al., 2003; Morteani et al., 2003; Snaith et al., 2004]. Similar considerations make bilayer structures (which, as pointed out above, can form

spontaneously during the casting process) attractive for polymer photovoltaics [Granström et al., 1998; Arias et al., 2002; Chappell et al., 2003; Corcoran et al., 2003; Kim et al., 2004]. In appropriate circumstances, lateral phase separation can be templated by an underlying pattern created by, for instance, soft lithography [Böltau et al., 1998]. In all these cases, casting techniques are particularly attractive as they represent relatively inexpensive and facile processing methods to produce a wide range of different surface morphologies with tailored features.

5.3 Nanoparticles in polymer films: morphological implications

In polymer film processing, the addition of nanoparticles has been initially investigated as a way to stabilize the structure of homopolymer-based samples against dewetting [Ramanathan and Darling, 2011]. Nevertheless, similarly to the case of bulk systems, in recent years the intriguing opportunity of incorporating nanofillers to polymer blend films in order to tune their morphology of has attracted the attention of numerous researchers. Some meaningful findings are discussed hereinafter.

The first quantitative studies of the influence of nanofillers on the phase separation dynamics during casting have been carried out by Composto and co-workers on silica-filled blends of PMMA and poly(styrene-co-acrylonitrile) (SAN) [Chung et al., 2004]. The dispersion of the filler is initially uniform, and during phase separation the silica particles are sufficiently mobile to partition into the PMMA domains. This results in a slackening of the evolution of the phases, ascribed to an increase of the viscosity of the preferred phase. The same research group has highlighted that an appropriate surface modification may promote the segregation of silica particles at the PMMA/SAN interface, thereby stabilizing the morphology of the film even at low filler content (< 2 phr) [Chung et al., 2005; Gam et al., 2011].

The phase separation of a toluene solution of PS and PMMA in the presence of metal (cobalt-platinum-copper) nanoparticles has been investigated by Minelli and co-workers [Minelli et al., 2006]. The morphology of the unfilled PS/PMMA blend at weight composition 80/20 is characterized by PMMA domains dispersed in a PS matrix. The addition of the filler, which partitions in the PS-rich phase and at the PS/PMMA, does not qualitatively alter such structure, but significantly reduces the size of the dispersed phase and affects the topography and surface texture of the

resulting film. Specifically, increasing the filler concentration results in an increase of the surface density of PMMA domains and, therefore, of the film thickness and surface roughness. The authors have ascribed the observed morphological modifications to the compatibilizing role exerted by the filler, which reduces the interfacial energy between the phases, and to the increased viscosity of the preferred PS phase. The latter effect is claimed to reduce the mobility of the polymer chains, provided that the inter-particle distance is comparable with the radius of gyration of the individual polymer molecule [Cole et al., 1999; Vacatello, 2001]. The same research group has highlighted that uneven partitioning of CdSe nanoparticles in a spin-cast PS/PMMA blend results in a the formation of ordered filler patterns inside the laterally-separated domains [Minelli et al., 2004].

The scenario depicted so far points out that, despite the major differences in comparison with the bulk systems treated in Part I, a clever use of inorganic nanoparticles can be beneficial also for immiscible polymer blend films, aiming to finely control their surface morphology and properties. However, almost all of the studies reported in the literature concern spin-cast blends of amorphous polymers, and there is still plenty of room for exploring the potential of such nano-sized fillers in semi-crystalline polymer systems. This is one of the stimuli for the research activity carried out on polymer films, that is the focus of Chapter 6.

6

Surface morphology and texture of semi-crystalline polymer films*

The ability of finely tuning the surface morphology and topography of polymer films is crucial as the surface dictates the performances of the final systems. The systematic study of the parameters that govern the surface morphology of semi-crystalline polymer films obtained via solvent casting is the focus of this chapter. After providing experimental details (§6.1), the discussion revolves around homopolymer-based films, assessing how their surface features are determined by the physicochemical properties of the pristine solution and the solution/substrate interactions (§6.2). On the basis of the reported results, the casting route has been optimized for the preparation of multiphase polymer films. For the latter, the phase separation process and the resulting surface structure are found to be influenced by the relative amounts of the polymeric components (§6.3) and the incorporation of nanoparticles (§6.4). Specifically, either a refinement or a coarsening of the surface morphology is observed depending on the affinity of the filler with the other constituents of the starting solution.

6.1 Prefatory notes

The literature review presented in Chapter 5 highlights the main differences between the evolution of the bulk microstructure of multiphase polymer systems and the development of the surface morphology of a polymer film during solvent casting. The latter process is the object of the fundamental study presented hereinafter, aimed to systematically investigate the parameters that govern the surface structure of solvent-cast polymer films (among others, crystallinity) and to

* Part of the results presented in this chapter has been published in Causa A, Filippone G, Acierno D, Domingo C, Salerno A, "Surface morphology, crystallinity, and hydrophilicity of poly(ε-caprolactone) films prepared via casting of ethyl lactate and ethyl acetate solutions", Macromol. Chem. Phys. 216, 49-58 (2015).

shed light on the complexities that arise when two or more polymer phases and solid fillers are present in the starting solution.

The polymeric constituents of the studied systems are poly(ε-caprolactone) (PCL) and poly(ethylene oxide) (PEO). They are both semi-crystalline and biodegradable and form an immiscible polymer pair whose technological interest has been extensively reported [Qiu et al., 2003; Fang et al., 2007]. In particular, PCL/PEO blends are used in biomedical applications such as controlled drug delivery and porous scaffolds for tissue engineering [Washburn et al., 2002; Park et al., 2005; Lyons et al., 2008]. The used solvents are ethyl lactate (EL) and ethyl acetate (EA), which are obtained via the esterification of ethanol with lactic and acetic acid, respectively. The solvent precursors are both generated from biomass and, hence, EL and EA represent benign alternatives to traditional hazardous organic solvents. The films are obtained by casting a drop of polymer solution onto a glass substrate and subsequently drying it at a controlled temperature. The judicious choice of the materials makes the casting process completely sustainable, and therefore suitable for the production of films for bio-related purposes.

The mechanism of formation of the films and the final surface features are preliminary investigated for homopolymer-based systems, assessing the impact of the physicochemical properties of the starting solution and the interactions between the latter and the casting substrate. In line with this aim, the visual monitoring of the casting process has been combined with morphological observations performed through different techniques: optical, confocal and scanning electron microscopy. The study of monophasic polymer films represents the basis for the optimization of materials and processing conditions of polymer blends. The possibility of tuning the surface morphology and texture of the final films by adjusting the blend composition is explored through the same characterization described above. The effect of the incorporation of fillers with different surface functionalities is finally inspected by coupling microscopy techniques and energy dispersive spectroscopy.

PCL and PEO, with molecular weights of 60 and 100 kDa respectively, have been purchased from Sigma-Aldrich (Madrid, Spain). The solvents, both having a purity grade ≥ 99.0 wt%, have been used without further purification; EL has been supplied by Sigma-Aldrich (Madrid, Spain), EA by Panreac Química (Madrid, Spain).

Four different kinds of commercially available NPs have been selected as fillers: hydroxyapatite (HA, calcium phosphate) particles with size < 200 nm, purchased from Sigma-Aldrich (Madrid, Spain); an aluminium magnesium layered double hydroxide (LDH, Perkalite® F100S modified with a hydrogenated fatty acid) comprising individual platelets of ~ 0.5 nm in thickness and ~ 150 nm in width, provided by AkzoNobel (Amersfoort, The

Netherlands); hydrophilic titanium dioxide (Aeroxide® TiO_2 P25) and hydrophobic titanium dioxide (Aeroxide® TiO_2 T805, treated with octylsilane), both consisting of primary particles with average size of 21 nm, supplied by Evonik Industries (Essen, Germany).

The pristine polymer solutions have been prepared by mixing the components under stirring at 60 °C for 4 h on a common laboratory heater (RCT basic, IKA, Staufen, Germany). Different total polymer concentrations have been selected: 2, 5 and 10 wt/vol% for the homopolymer-based systems (of either PCL or PEO); 5 wt/vol% for the polymer blend systems, characterized by the presence of PCL and PEO in the weight proportions 90/10, 80/20, 70/30 and 60/40.

For the nanoparticle-filled systems, the polymer weight ratio has been fixed to 60/40 and the materials have been prepared by means of a two-step procedure, as described in the following. First, each kind of filler has been separately dispersed in EL at a concentration of 5 wt/vol%; the suspension has then been subjected twice to magnetic stirring for 5 min and subsequent ultrasonication for 15 min in order to reduce particle aggregates. Second, the concentration of filler has been adjusted by adding pure EL and the polymers have been finally incorporated in order to obtain different solutions with a fixed polymer concentration of 5 wt/vol% and variable filler content of either 3 or 5 wt% relative to the polymer blend. Mixing has been carried out at 60 °C for 4 h on a laboratory heater.

Subsequently, the films have been manufactured through a drop casting procedure. In particular, circular glass slides, having a diameter of 12 mm and a thickness of 0.15 mm (Labbox Labware, Barcelona, Spain), have been cleaned with acetone and pre-heated at 40 °C on a common laboratory heater (RCT basic, IKA, Staufen, Germany). Next, a 10 µL droplet of polymeric solution has been pipetted onto the glass slide and the solvent has been allowed to evaporate by keeping the system at 40 °C overnight.

The physical and chemical properties of the pristine solutions have been assessed by means of rheological tests and wettability measurements. The steady-shear behavior of the solutions has been investigated using a stress-controlled rheometer (MCR 302, Anton Paar, Graz, Austria). The experiments have performed at room temperature and in the range of shear rate of $\dot{\gamma}$=0.1-100 s^{-1}. The wettability of the substrate by pure solvents and PCL solutions has been assessed by dropping a 3 µL volume of sample onto the glass slides and measuring the static contact angle values by means of a contact angle system (DSA 100, Krüss, Hamburg, Germany). Five independent measurements have been carried out for each composition, using the Young/Laplace method to fit the shape of the sessile drop.

The spreading dynamics of the solutions on the substrates have been studied to assess the mechanisms of film formation through drop casting as a function of solvent type and polymer concentration. The measurements have been carried out by collecting photographs of the sample at specific time intervals and analyzing the resulting images by means of the Image J® public domain software.

The crystallization of the polymers and the final crystalline structure and surface morphology of the films have been investigated using an optical microscope (Olympus

BX51, Tokyo, Japan) in both direct and transmission mode. The optical micrographs have been further analyzed by using the ImageJ® software to assess the area fraction and characteristic size of the phase domains. At least five pictures, made over different regions of independent specimens and at different magnifications, have been analyzed for each blend, following the procedure that is described in detail in Appendix A.4. The statistical significance of the results has been assessed by one-way ANOVA. Tukey post-hoc test at the significance level $p < 0.03$ has been used to identify statistically different data by means of the software OriginPro 8.

The microstructure of the samples has been further inspected through scanning electron microscopy (SEM, QUANTA200F FEG ESEM, FEI, Eindhoven, The Netherlands). The surface of each sample has been gold-sputtered before SEM observations. Energy dispersive spectroscopy (EDX, INCA by Oxford Instruments, High Wycombe, United Kingdom) has been used to investigate the localization and distribution of the nanoparticles.

The surface texture of the samples has been examined by means of confocal microscopy (Leica DCM 3D, Wetzlar, Germany). The analysis has been carried out on the gold-sputtered surface of the samples with a 50X objective and relevant topographical parameters (defined by ISO 25178 standard) have estimated. The root mean square height of the surface (*Sq*), corresponding to the standard deviation of the height distribution, is used to assess the surface roughness of the films. The developed interfacial area ratio (*Sdr*), defined as the percentage deviation of the actual surface from perfect flatness, is used to assess the specific surface of the films. The analysis has also enabled the assessment of the skewness of the height distribution (*Ssk*), which is indicative of the symmetry of the topography about the mean plane; in particular, positive (respectively negative) values of *Ssk* indicate that the bulk of the material is below (respectively above) the mean plane.

6.2 Formation and surface structures of monophasic films

Drop casting of homopolymer-based solutions has brought about the formation of films with various surface morphologies, depending on the polymer/solvent pair and the initial polymer concentration. As shown in the SEM micrographs of Figure 6.1, the PCL samples cast from both EL and EA exhibit a continuous and homogeneous structure, characterized by spherulitic crystals (see inset of Figure 6.1c). The latter appear flat and sharp-edged in the films prepared from solutions at low PCL concentration, being smaller and more rounded at higher polymer content. Furthermore, the samples obtained from EA solutions exhibit smaller spherulites compared with those prepared from EL solutions. The spacing between crystalline domains is evidenced by the bright zones in the micrographs.

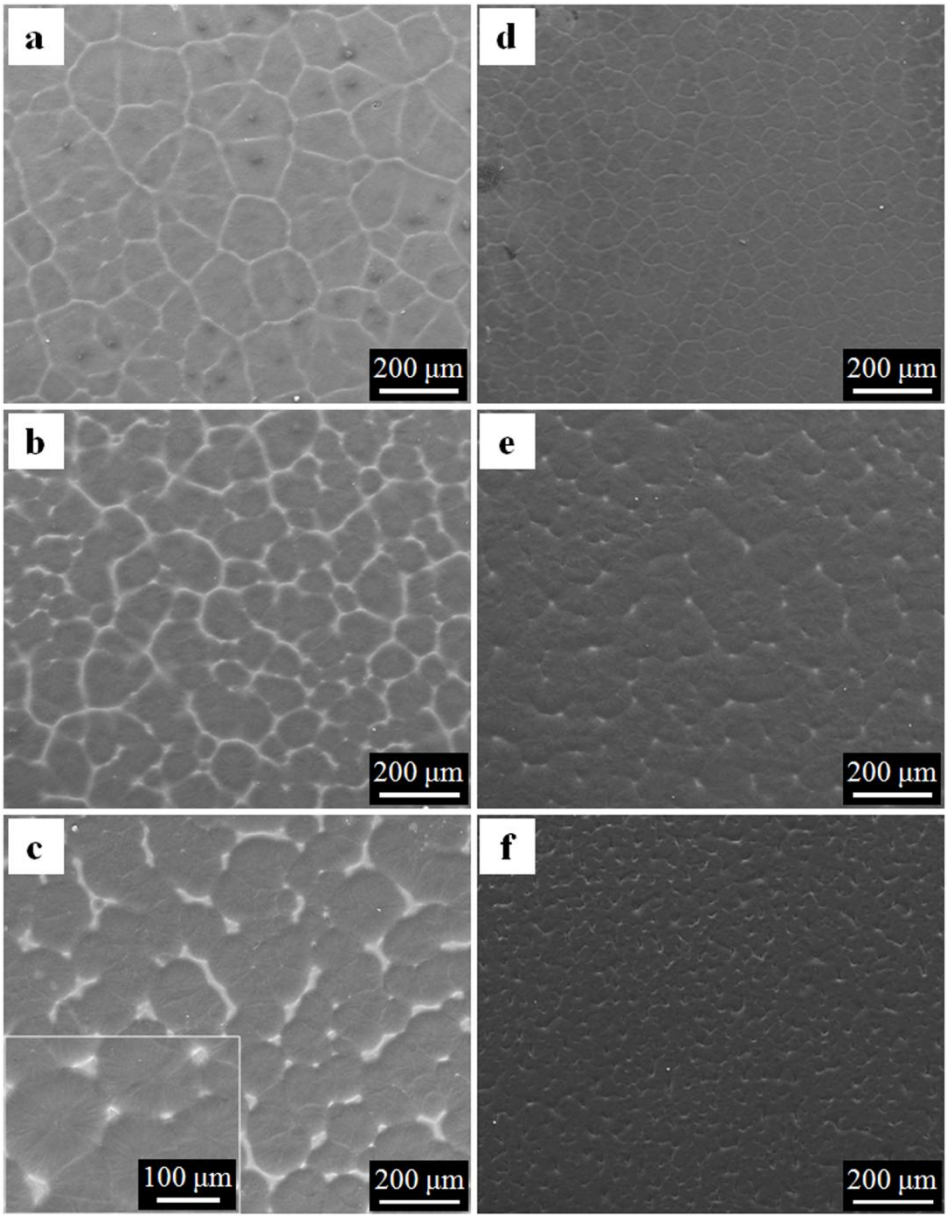

Figure 6.1 – SEM micrographs of the PCL samples obtained from solutions in EL (a-c, from 2 to 10 wt/vol%) and EA (d-f, from 2 to 10 wt/vol%). Adapted from [Causa et al., 2015] with permission by John Wiley and Sons.

Regarding the PEO samples, whose structures are shown in the SEM micrographs of Figure 6.2, the effect of polymer concentration is not clearly detectable, while the solvent choice plays a major role. Indeed, casting from EL solutions leads to the formation of continuous films. The PEO spherulites are much larger than the PCL ones, the order of magnitude of their diameter being 10^3 μm. These spherulites, as shown in the inset of Figure 6.2a, are composed by crystalline

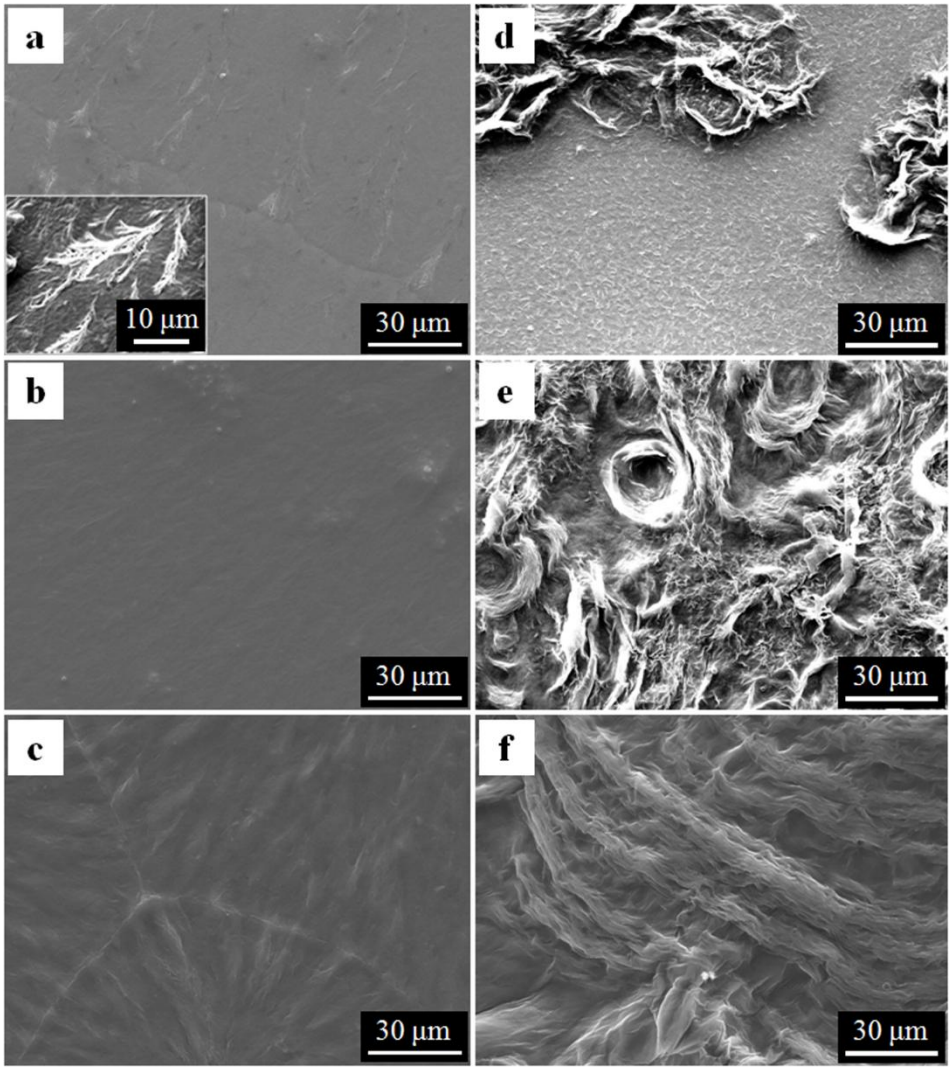

Figure 6.2 – SEM micrographs of the PEO samples obtained from solutions in EL (a-c, from 2 to 10 wt/vol%) and EA (d-f, from 2 to 10 wt/vol%).

lamellae whose arrangement is reminiscent of the wheat-like morphology observed by Hou and co-workers [Hou et al., 2007]. Conversely, disordered, bundle-like PEO structures result from EA solutions.

In the light of the observations expressed above, PCL-based systems have revealed to be particularly suitable for a systematic study aimed to investigate the interplay among solvent nature, polymer concentration and solution-substrate interactions and assess the influence of such factors on the formation of the films. Thereinafter, downline of a characterization of the physicochemical PCL solutions in both EL and EA, a critical analysis of the drop casting process is performed.

6.2.1 Influence of the physicochemical features of the pristine solutions on the mechanism of film formation

The viscosity of the pure EL and EA solvents at 25 °C are $\eta = 2.44 \times 10^{-3}$ Pa s and $\eta = 0.423 \times 10^{-3}$ Pa s, respectively [Dean, 1998]. As shown in Figure 6.3, all the solutions exhibit a Newtonian behavior in the whole range of shear rates investigated. The viscosity of the solvent increases with increasing polymer concentration, being generally higher for the EL solutions.

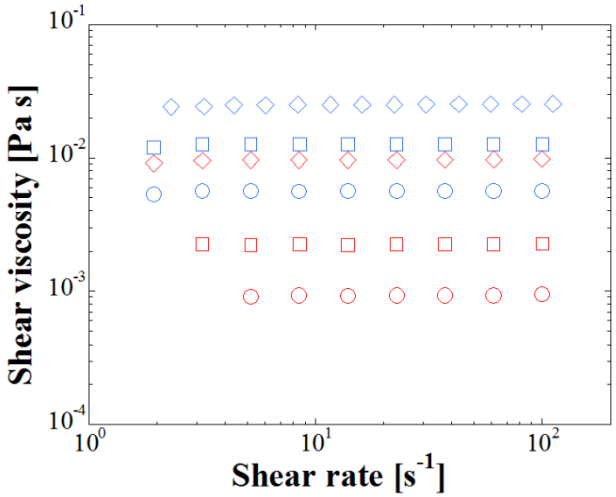

Figure 6.3 – Steady shear viscosities of solutions of PCL in EL (blue symbols) and EA (red symbols) at different polymer concentrations: 2, 5 and 10 wt/vol% (circles, squares and diamonds). Adapted from [Causa et al., 2015] with permission by John Wiley and Sons.

According to the wettability tests, the contact angle of EL deposited onto the glass substrate is 13.4 ± 2.2° and negligible changes have been recorded for all the studied EL solutions. The contact angle of pure EA has not been assessed with sufficient accuracy, because of the too fast evaporation of the solvent drop. Only the EA solution at 10 wt/vol% of polymer is stable enough to allow a reliable estimation of the contact angle, corresponding to 20.9 ± 1.6°. A corroboration of the higher wettability of glass by the EL system is given by the fact that the glass surface is hydrophilic and EL, being more polar than EA (their relative dielectric permittivities at room temperature are 15.7 and 6.08 respectively), is thus more chemically affine to the substrate [Dean, 1998; Aparicio and Alcalde, 2009].

To sum up, the EL systems have a higher affinity than the EA solutions with the glass substrate. On the other hand, the EL solutions are more viscous than the EA ones, and this should limit the spreading of the former samples onto the substrate. Moreover, the latter parameter is inversely related to the solvent evaporation rate, which is faster for EA. In the light of the previous considerations, the kinetics of formation of the polymeric film by drop casting have been studied in detail.

As pointed out in §5.1, the evolution of a drop of a dilute polymer solution on a wettable surface and the properties of the film that remains after solvent evaporation drastically depend on surface tension effects, polymer concentration and solution viscosity. In particular, the difference in surface tension $\Delta\gamma$ existing between the solute and the solvent is responsible for the flow of the polymer inward or outward the solution drop; the direction such flow depends on the value of $\Delta\gamma$. The surface tension of PCL, evaluated by means of contact angle measurements, is reported to be γ = 52.3 mN m^{-1} at room temperature [Wu et al., 2011]. The solvents are instead characterized by lower surface tension values, corresponding to γ = 28.3 mN m^{-1} for EL and γ = 23.4 mN m^{-1} for EA [Dean, 1998]. Hence, in the studied systems the polymer flows outwards the solution and accumulates at the rim. As a direct consequence, a "coffee stain" effect is observed, and the final film evidences a ring-shaped morphology. The polymer viscosity also affects the dynamics of formation of the film as, in general, an increase of the initial polymer concentration results in an amplification of the size of the polymeric rim [Poulard and Damman, 2007].

The evolution of the basal area of the drops during the casting process is shown in Figure 6.4 for the different studied solutions. The basal area A_t of the drops, which assume a spherical-cap shape soon after deposition, is reported as a function of time; the data are normalized by their initial values A_{t0}, which are plotted in Figure 6.4a and 6.4b for the EL and EA systems respectively. The area A_r of the

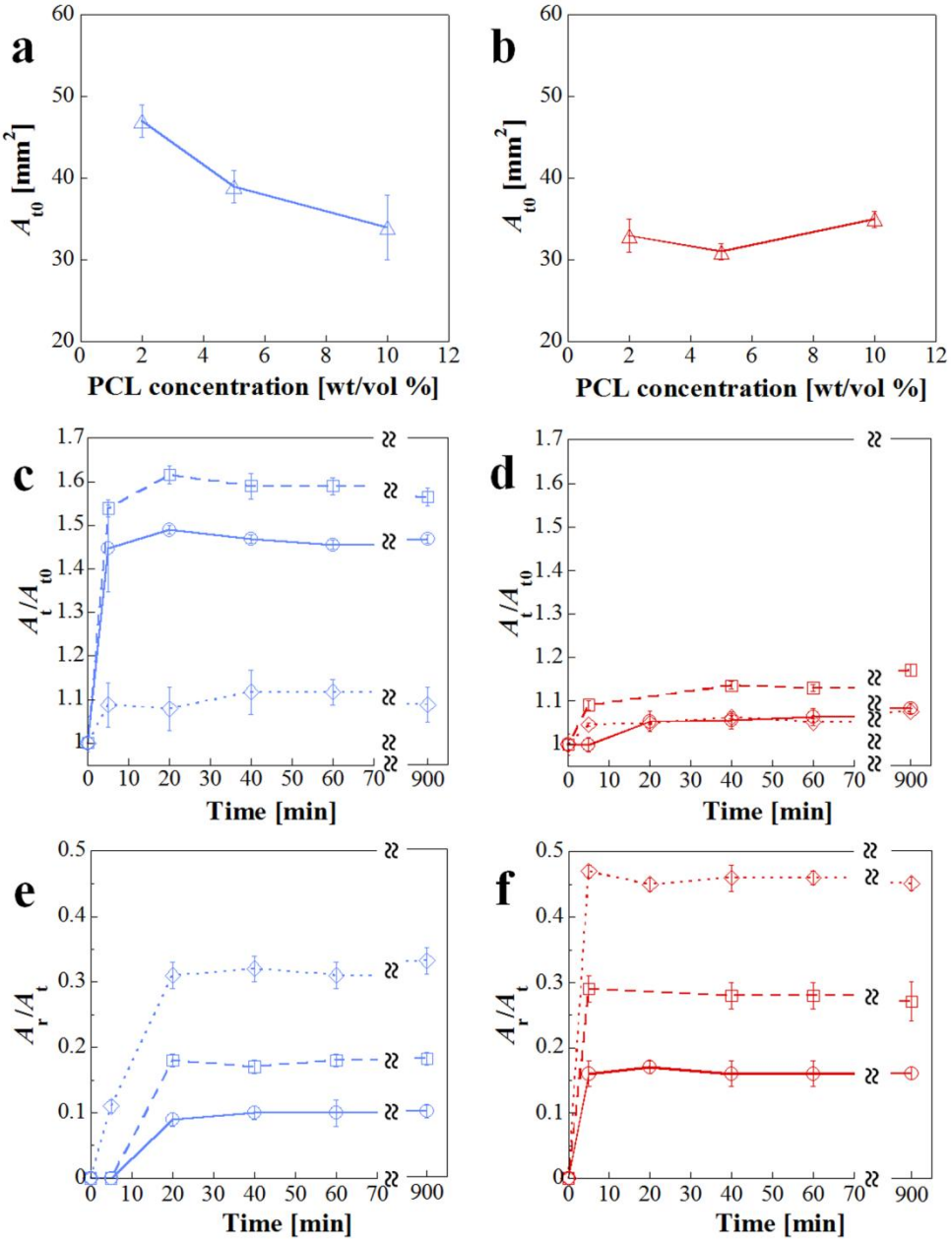

Figure 6.4 – Initial basal area, time evolution of both the normalized basal area and the area fraction of the outer ring for the drops of (a, c, e) PCL-EL and (b, d, f) PCL-EA solutions at different polymer concentrations: 2, 5, and 10 wt/vol% (circles, squares and diamonds). Adapted from [Causa et al., 2015] with permission by John Wiley and Sons.

outer ring, which forms during drying due to the "coffee stain" effect, is also reported as a fraction of the total area A_t.

The basal area of the drops of the EL solutions grows rapidly in the earlier stages at any composition, and equilibrium values are approached in about 20 minutes (Figure 6.4c and 6.4e). At this point, a ring-shaped PCL-rich deposit is visible at the edge of all the samples. By increasing polymer concentration, significant variations of both the basal area and the rim area fraction are observed. In particular, considering the equilibrium values, A_t decreases by about 40% when passing from 2 to 10 wt/vol%, whereas the percentage extension of the rim A_r/A_t exhibits a three-fold increase; a visual evidence of such variations is given by the images of Figure 6.5a and 6.5b. The same general trend is noticed when dealing with the EA solutions (Figure 6.4d and 6.4f), but in this case the percentage increase of A_t is much lower and the equilibrium conditions are reached faster than for EL. In particular, after 5 min from the deposition of the solution, the film has achieved its final shape and the formation of polymer-rich edges has been detect. After that and up to 900 min, minor variations of the basal surface are found at different polymer contents, but the width of the external ring is significantly affected by polymer concentration. Indeed, A_r/A_t triples when polymer concentration is increased from 2 to 10 wt/vol%.

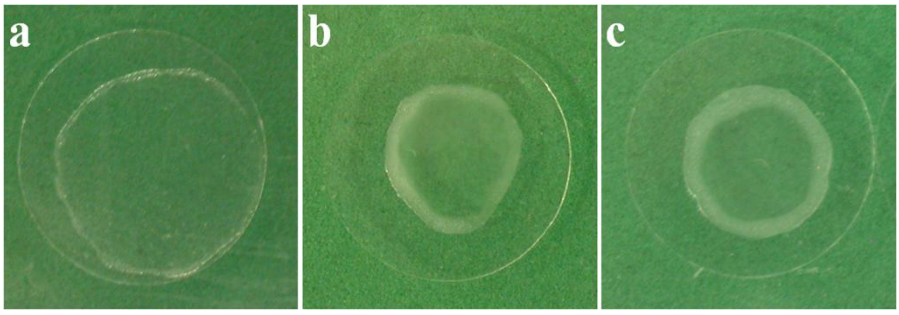

Figure 6.5 – Final film structure achieved in the case of (a) 2 wt/vol% PCL-EL solution, (b) 10wt/vol% PCL-EL solution and (c) 10wt/vol% PCL-EA solution. Adapted from [Causa et al., 2015] with permission by John Wiley and Sons.

The differences exhibited by the studied systems during the drying process point out that solvent polarity, $\Delta\gamma$, solution viscosity, and evaporation rate are all involved in the mechanism of formation of the film, but it seems that the latter parameter might play a major role. The higher polar affinity of EL to the glass substrate could reflect the enhanced spreading of the EL solutions if compared to

the EA ones. However, the high evaporation rate of EA causes a fast accumulation of polymer at the air-solution interface and a drastic increase in viscosity, which hinders the spreading irrespective of the affinity with the substrate. The spreading of the drops can proceed till the contact line is pinned due to both the evaporation of the solvent at the drop edge and the contemporary outward polymer flow. As a consequence, the fast evaporation rate of EA reduces the spreading of the drops and accelerates the precipitation of PCL and its subsequent accumulation at the edge. Concerning the "coffee stain" effect, it is worth noting that an increase in polymer concentration generally results in an amplification of the external deposit due to a high $\Delta\gamma$. Most importantly, the comparison of Figure 6.5b and 6.5c indicates that the formation of the rim is mainly due to surface tension effects, rather than viscosity effects. Indeed, it should be expected that the lower viscosity values of the EA systems with respect to the EL ones result in higher values of rim width. The experimentally observed opposite trend is mainly ascribed to the high $\Delta\gamma$ that characterizes the PCL-EA solutions.

Figure 6.6 reports the results of measurements of the thickness of the central part of the films as a function of polymer concentration and solvent type, carried

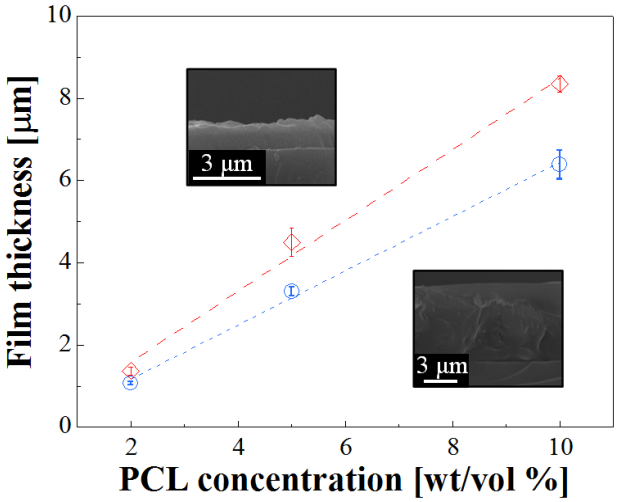

Figure 6.6 – Correlation between film thickness and PCL concentration ì in the EL (blue symbols) and EA solutions (red symbols). The SEM images refer to the cross-section of PCL samples prepared from EA solutions with polymer concentration 2 wt/vol% (up-left side) and 10wt/vol% (down-right side). Adapted from [Causa et al., 2015] with permission by John Wiley and Sons.

out to obtain further information about the influence of the properties of the starting solutions on film formation. These tests reveal that the thickness of the films is in the 1÷9 μm range, increasing by rising PCL concentration. Furthermore, the highest values are achieved for the films obtained from EA solutions. These results are in line with the previously discussed effect of the decrease of the drop spreading with the increase of PCL concentration, as well as with the significantly lower spreading of the EA systems in comparison with the EL ones.

6.2.2 Crystalline and topographical features of the films

Aiming to study the morphology of semi-crystalline polymers such PCL and PEO, the information provided by the SEM technique can be reliably completed by optical microscopy. The surface structure of the formed PCL films are shown in the optical micrographs of Figure 6.7 and 6.8, respectively acquired in direct and transmission mode. Images of the PEO films obtained by casting EL solutions are reported in Figure 6.9. The crystallization of both polymers starts from nucleation sites and proceeds with a radial growth, bringing about the formation of spherulites with lamellar structure. The growth front is hindered by the impingement of adjacent spherulites, which determines the final shape of the crystalline domains. The different structures of PCL and PEO crystals clearly emerge from the images obtained with polarized light: PCL spherulites consist of bundles of primary lamellae (evidenced by the Maltese cross pattern of birefringence), while PEO crystallites are composed by short dendrites.

Concerning the PCL samples, the observed effects of the characteristics of the pristine solutions on the final crystalline structure have been roughly expressed above: the size of the spherulites decreases by increasing polymer concentration in both solvents, and the spherulites in the films cast from EA are smaller than in those cast from EL. Such considerations are corroborated by crystal size measurements performed on low magnification optical images, such as those shown in Figure 6.10. The size distribution of the crystalline domains shifts to smaller sizes by increasing polymer concentration. Such transition is more gradual in the EL cast films (Figure 6.10a) than for the EA systems. For the EL systems, the size of the spherulites (see Table 6.1) decreases by about 50% as PCL concentration is increased from 2 to 10 wt/vol%. Regarding the EA cast films (Figure 6.10b), the most significant variation in the crystal size distribution is appreciated when the polymer concentration increases from 5 to 10 wt/vol%, as the corresponding mean domain size decreases by more than 40%.

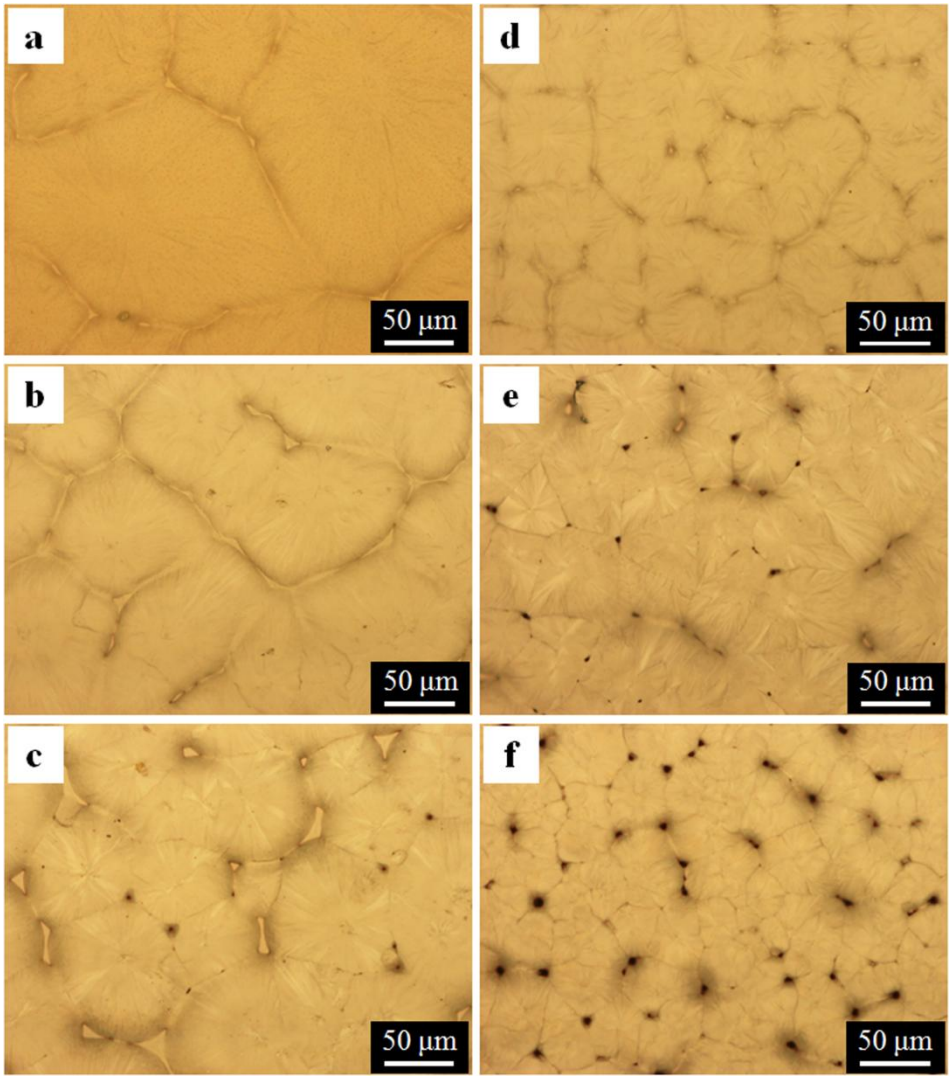

Figure 6.7 – Optical micrographs of PCL films prepared from solutions in EL (a: 2 wt/vol%; b: 5 wt/vol%; c: 10 wt/vol%) and EA (d: 2 wt/vol%; e: 5 wt/vol%; f: 10 wt/vol%). Adapted from [Causa et al., 2015] with permission by John Wiley and Sons.

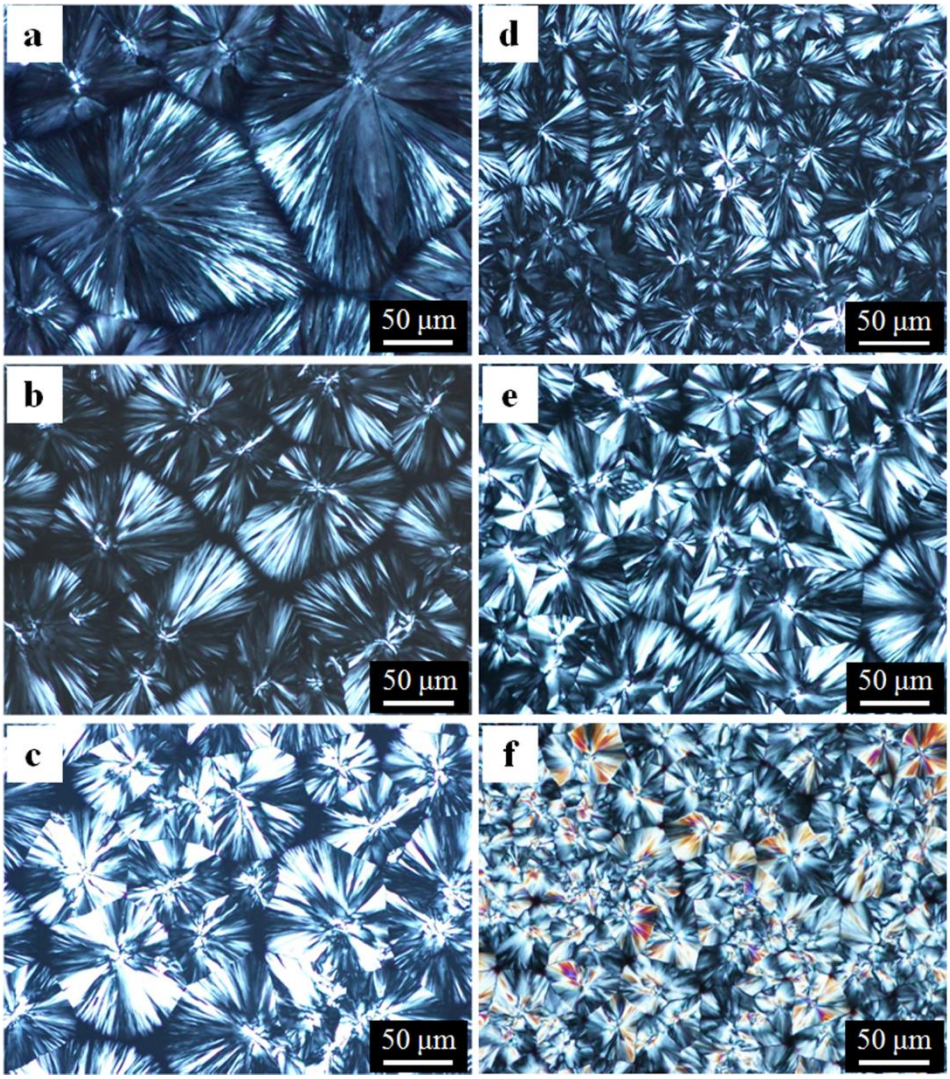

Figure 6.8 – Polarized optical micrographs of PCL films prepared from solutions in EL (a: 2 wt/vol%; b: 5 wt/vol%; c: 10 wt/vol%) and EA (d: 2 wt/vol%; e: 5 wt/vol%; f: 10 wt/vol%). Adapted from [Causa et al., 2015] with permission by John Wiley and Sons.

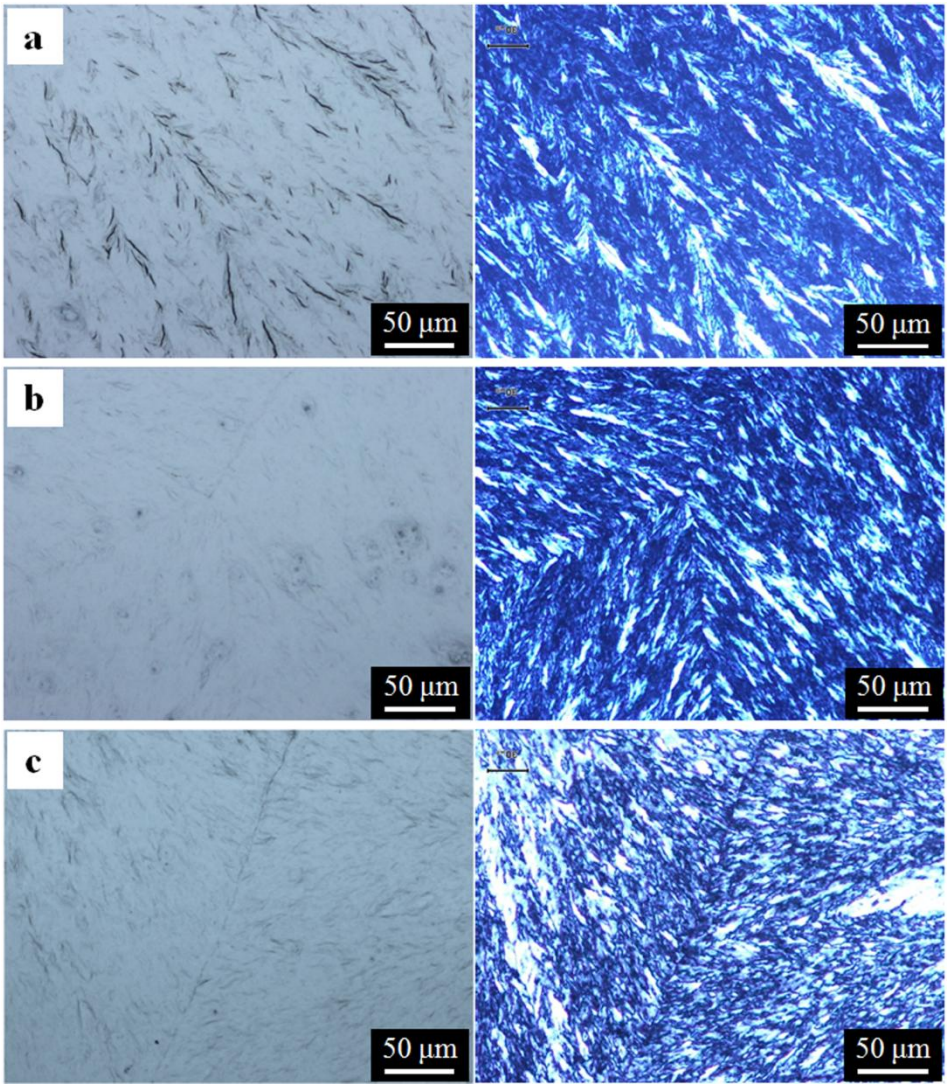

Figure 6.9 – Optical micrographs (in direct and transmission mode) of PEO films prepared from solutions in EL (a: 2 wt/vol%; b: 5 wt/vol%; c: 10 wt/vol%).

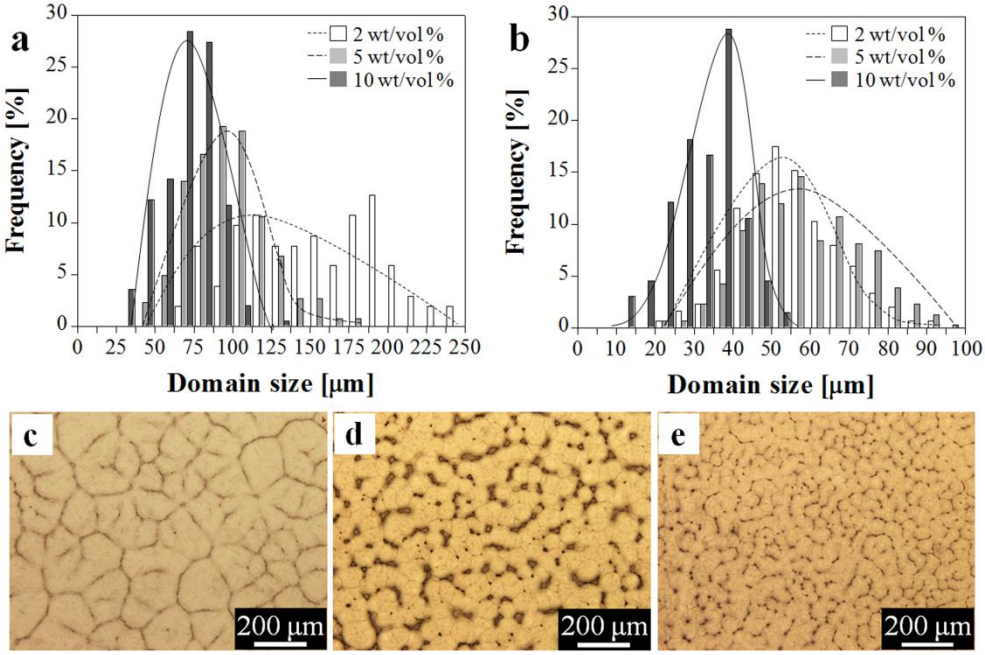

Figure 6.10 – PCL spherulite size distribution in the EL (a) and EA cast films (b) and micrographs of representative films cast from different solvents and polymer concentration: (c) EL, 2 wt/vol%; (d) EL, 10 wt/vol%; (e) EA, 2 wt/vol%. The lines are a guide to the eye. Adapted from [Causa et al., 2015] with permission from John Wiley and Sons.

Table 6.1 – Geometrical features of the crystallites in the PCL films. Adapted from [Causa et al., 2015] with permission from John Wiley and Sons.

Solvent	Polymer concentration [wt/vol%]	Size [µm]	Height [µm]	Spacing [µm]
EL	2	151.1 ± 44.6	0.12 ± 0.01	5.10 ± 0.64
	5	97.1 ± 26.2	0.28 ± 0.09	4.73 ± 0.37
	10	70.0 ± 17.2	0.28 ± 0.04	4.67 ± 0.53
EA	2	54.8 ± 12.6	0.22 ± 0.10	3.49 ± 0.41
	5	58.6 ± 14.3	0.29 ± 0.11	4.12 ± 0.82
	10	32.7 ± 8.5	1.98 ± 0.48	11.65 ± 0.92

The reduction of the size of PCL spherulites with increasing polymer concentration is mainly ascribable to the increase in the solution viscosity, which in turn promotes nucleation while limiting the growth of the nuclei that form during the evaporation of the solvent [Simon et al., 2007; Greenman et al., 2014]. The enhanced crystal growth for the EL systems compared to the EA ones is ascribable to the lower evaporation rate of EL, which slows down the nucleation rate, resulting in a low number of large crystals.

The different surface morphologies obtained by changing polymer concentration and kind of solvent in the starting solutions result in dissimilar textural features, as inferable from confocal microscopy. The latter allows to estimate relevant topographical parameters of the films, reported in Table 6.11. The root mean square height of the surface, *Sq*, is a measure of the surface roughness of the films. The developed interfacial area ratio, *Sdr*, quantifies the deviation of the actual surface from perfect flatness and, in turn, the specific surface of the films. The skewness of the height distribution, *Ssk*, expresses the symmetry of the topography about the mean plane.

Table 6.2 – Textural features of the PCL and PEO films: surface roughness (*Sq*), specific surface (*Sdr*) and skewness (*Ssk*).

Polymer-solvent pair	**Polymer concentration [wt/vol%]**	***Sq* [µm]**	***Sdr* [%]**	***Ssk***
PCL-EL	2	0.01	0.03	- 2.69
	5	0.03	0.05	-4.12
	10	0.04	0.10	-5.72
PCL-EA	2	0.04	0.07	- 1.78
	5	0.05	0.12	- 5.67
	10	0.25	1.18	- 3.32
PEO-EL	2	0.18	0.35	3.01
	5	0.13	0.18	3.45
	10	0.36	0.86	1.60

Figure 6.11 shows representative high-magnification images of the surfaces of the PCL films. For them, two levels of roughness can be identified: one is related

to the lamellar structure of the single crystallite, while the other one reflects the space arrangement of the crystallites, separated by a certain inter-domain spacing. Confocal analysis has also allowed to estimate geometrical features of the

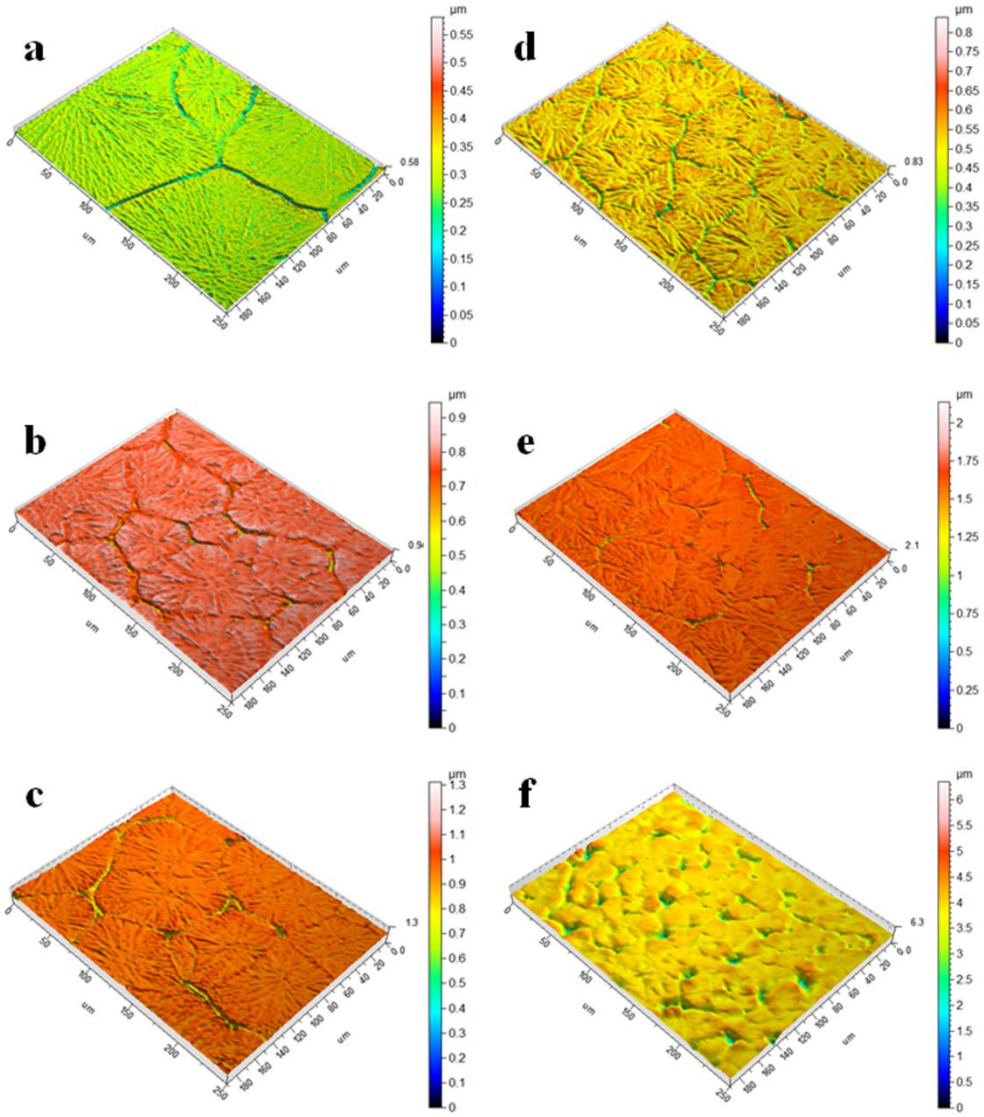

Figure 6.11 – Topography images of PCL films cast from solutions in EL (a-c, from 2 to 10 wt/vol%) and EA (d-f, from 2 to 10 wt/vol%). Adapted from [Causa et al., 2015] with permission from John Wiley and Sons.

crystallites, namely height and spacing, reported in Table 6.1 together with the mean crystal sizes. The cross-check of topographical and geometrical parameters highlights that increasing polymer concentration in the starting solution results in a rougher surface texture; moreover, the EA cast films are generally rougher than the EL cast ones. The lowest value of *Sq* is found for the EL cast film at 2 wt/vol%, which is characterized by large and thin crystallites. On the opposite, the roughest sample is the EA cast film at 10 wt/vol% that exhibits small but thick crystallites.

The differences in surface texture are related to the wettability of the surface of the polymer film, which is commonly studied by means of water contact angle measurements performed in static conditions [Martinelli et al., 2012; Yilgor et al., 2012]. These tests have been used to assess the hydrophilicity of PCL samples prepared from different solutions. The results of the water contact angle measurements, carried out on an area far away from the polymer-rich outer ring, are reported in Figure 6.12. For all the studied samples, contact angles in the 60-90° range have been measured. These data are in line with those reported in literature for PCL substrates, indicating the poorly hydrophilic nature of the polymer, which confers to PCL materials a low affinity to polar liquids such as water [Salerno et al., 2010]. Although static contact angle measurements are not the most appropriate to assess the effective contact angle values of each sample,

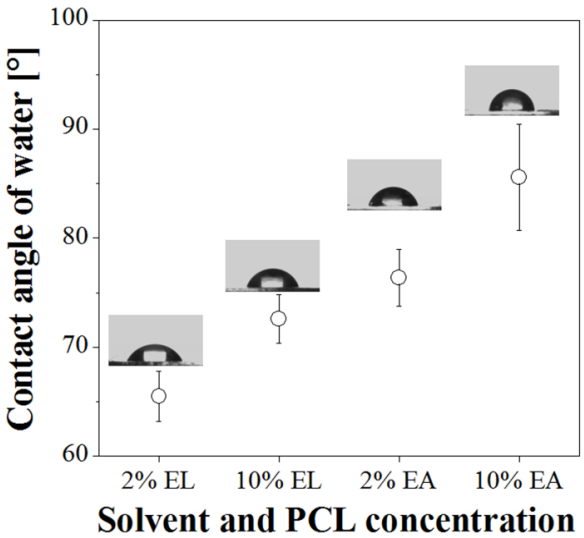

Figure 6.12 – Contact angle of water on PCL films cast from EL and EA solutions at different polymer concentrations: 2 wt/vol% and 10 wt/vol%. Adapted from [Causa et al., 2015] with permission from John Wiley and Sons.

these values may provide a general correlation between surface roughness and wettability. In particular, in agreement with the surface roughness data, for both the EL and EA cast films the contact angle increases by increasing polymer concentration; furthermore, the EA cast samples exhibit higher contact angles than the EL cast ones. The link between surface roughness and hydrophilicity can be ascribed to the inability of water to penetrate inside the grooves of a rough surface for capillarity. This leads to a low contact area between the film and the water drop and, therefore, to a high static angle.

Concerning the PEO films cast from EL solutions, representative surface images are shown in Figure 6.13. A comparison of the textural parameters reported in Table 6.1 reveals that these films are rougher than the PCL ones, and their surface topography is mainly determined by the lamellar structure of the single spherulite rather than by the spatial arrangement of the spherulites. Such a difference is suggested by the different signs of *Ssk*, which is negative for PCL and positive for PEO. Water contact angle measurements have not been performed on the PEO samples due to the hydrosolubility of such polymer.

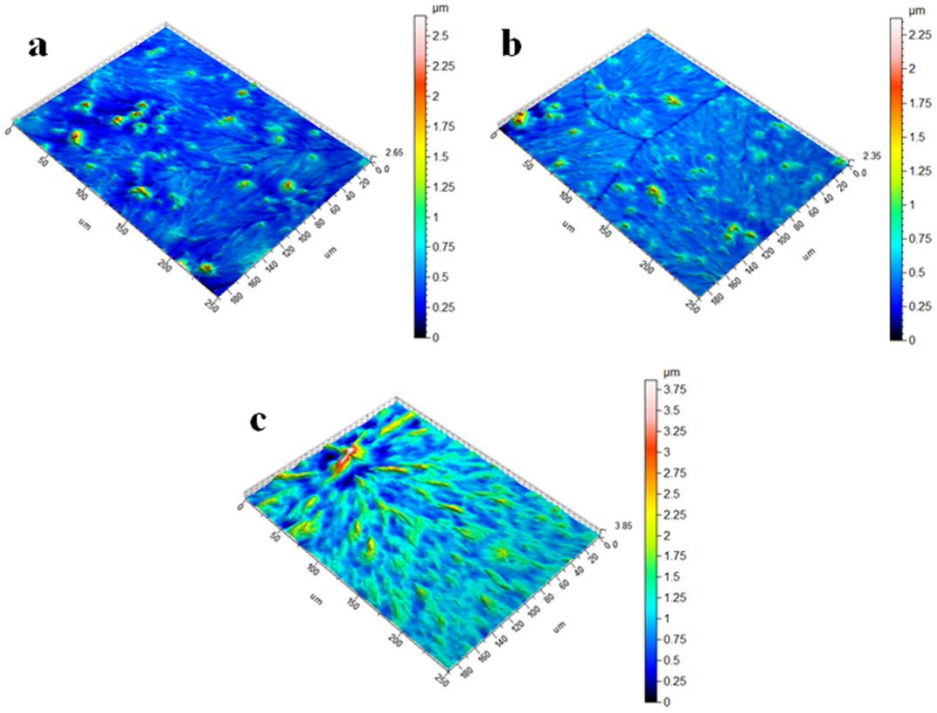

Figure 6.13 – Topography images of PEO films cast from EL (a-c, from 2 to 10 wt/vol%).

To summarize, in this section it has been pointed out the surface morphology and texture of solvent-cast polymer films can be reliably tuned by changing the main physicochemical properties of the starting solution, namely polymer concentration and kind of solvent. Apart from representing a systematic study of the parameters that govern the surface features of semi-crystalline polymer films, the reported results have served as a starting point for optimizing the preparation and characterization of multiphase polymer films.

6.3 Formation and surface structures of biphasic polymer films – Effect of composition

Due to the irregularity of the PEO structures formed using EA, PCL/PEO blend films have been prepared by casting EL solutions at overall polymer concentration of 5 wt/vol% onto glass substrates. The immiscibility of PCL and PEO results in phase separation during the solvent casting process. As shown in the optical micrographs of Figure 6.14, the unfilled PCL/PEO blend exhibits phase-separated surface morphologies in the whole range of investigated compositions, with significant differences depending on the relative amount of the two polymers. At the lowest PEO content (Figure 6.14a) the surface structure resembles that of the neat PCL (cf. Figure 6.7b), while PEO is in the form of small dispersed domains. By increasing the PEO weight fraction in the blend, the numerical density of the PEO-rich domains increases while their size slightly grows. This is evidenced by the results of image analysis, which are summarized in Figure 6.15 in terms of characteristic size and area fraction of the PEO-rich phase. Further PEO addition up to 40 wt% determines a phase inversion in the surface morphology of the film: the PCL/PEO blend at weight composition 60/40 exhibits isolated PCL domains suspended in a PEO-rich continuous phase. A closer inspection reveals that in all the blends the PEO phase exhibits a “salami-like” morphology, embedding small, rounded PCL domains. The results of image analysis indicate that such small PCL inclusions occupy between 10% and 20% of the surface area of the host phase.

Further morphological details of the blend films can be appreciated in the SEM micrographs of Figure 6.16. The PEO-rich regions appear brighter than the PCL-rich ones, and the presence of small-scale polymer inclusions in the various phases is clearly detectable. In particular, the PCL domains enclosed by the PEO-rich regions appear to be concave, as evidenced by the high-magnification micrograph of the sample at 20 wt% of PEO (inset of Figure 6.16b). In the same image it is

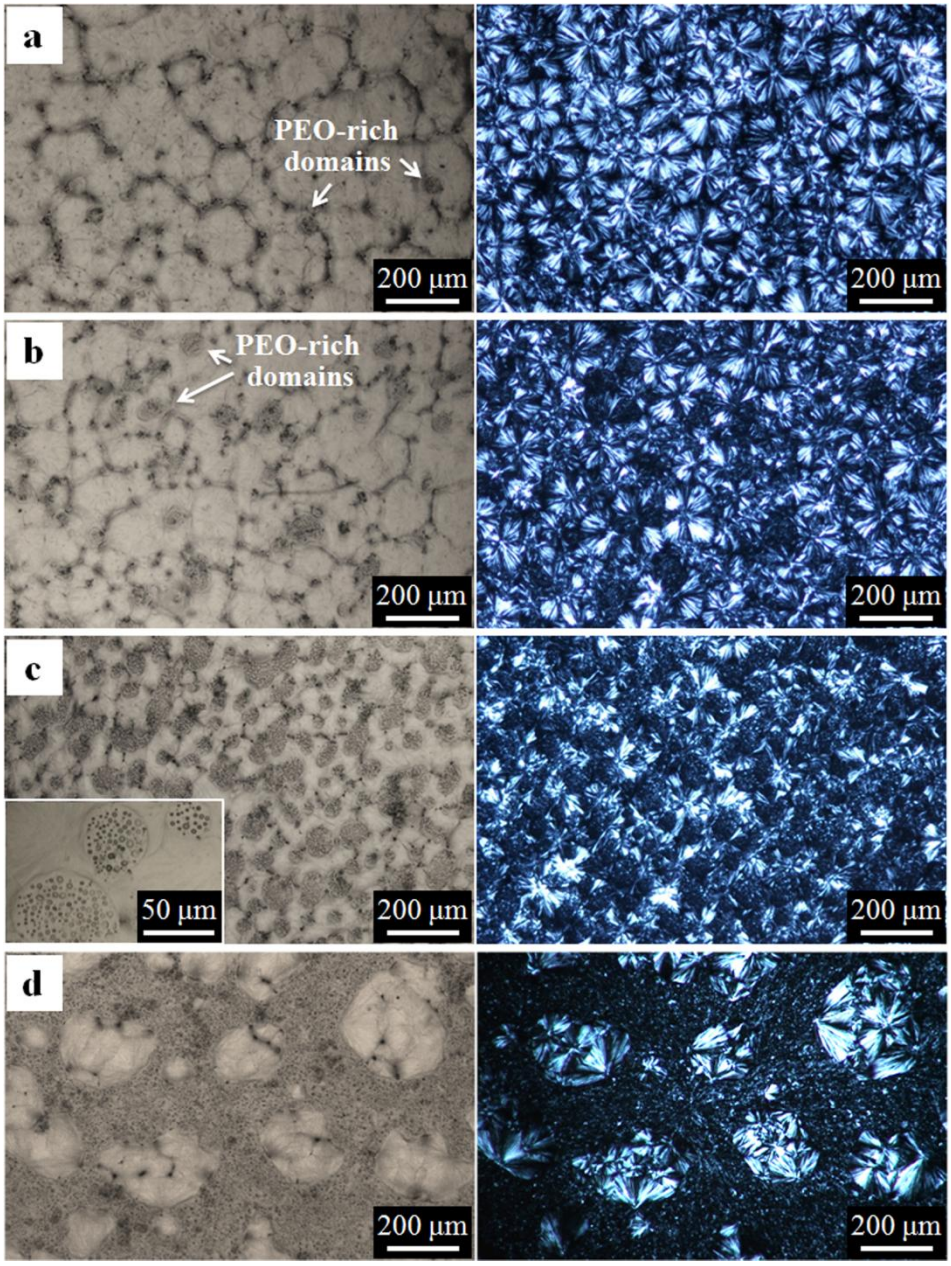

Figure 6.14 – Optical micrographs (in direct and transmission mode) of PCL/PEO blend samples at different weight compositions: (a) 90/10, (b) 80/20, (c) 70/30, (d) 60/40.

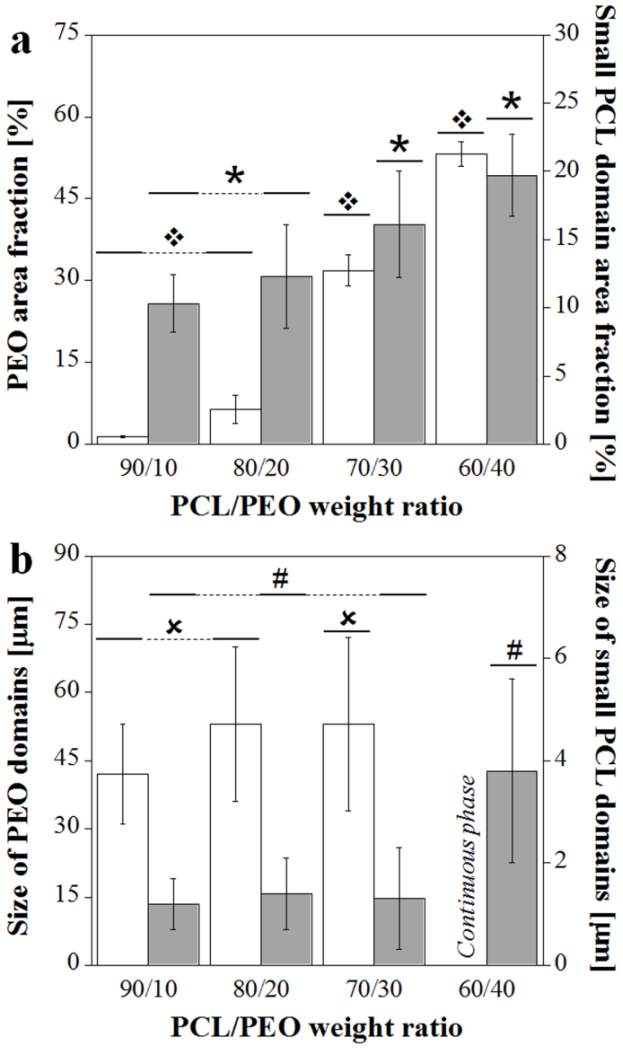

Figure 6.15 – Area fraction and mean size of the PEO-rich (white columns) and embedded PCL-rich domains (grey columns) in the unfilled blends. The symbols (asterisks, diamonds, hashes and crosses) placed above the histogram bars designate sets of statistically significant data ($p < 0.03$).

also possible to recognize the texture of the PCL and PEO crystals, respectively characterized by bundle-like and wheat-like lamellar structures.

The existence of polymer structures with different size scales (10^2-10^3 µm and less than 1 µm) in immiscible blend films has already been evidenced by Liu et al. for a blend of PCL and polyetherimide, as discussed in §5.2 [Liu et al., 2007] . The

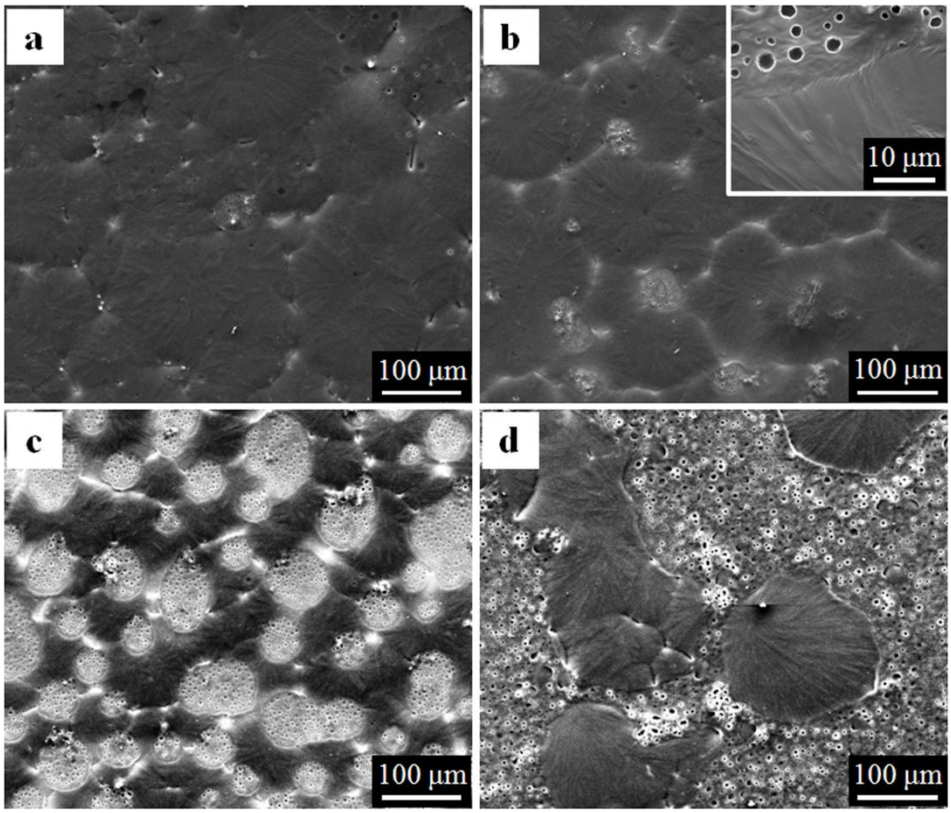

Figure 6.16 – SEM micrographs of films of unfilled PCL/PEO blends at different compositions: (a) 90/10, (b) 80/20, (c) 70/30, (d) 60/40.

authors propose that the formation of small-scale inclusions occur in the so-called "secondary phase separation", which is an intermediate step of the solvent casting process of solution blending. In brief, after the spreading of the starting solution, the solvent evaporates at the air/solution interface and induces the formation of liquid phases that contain both polymers, but have different compositions. The further evaporation of the solvent results in an increase of the viscosity of the solution, hence the polymer chains are only able to diffuse over short distances. Such hindered diffusion is mainly responsible for the formation of small polymer domains, which result from the late precipitation of the minor polymeric constituents trapped in the each phase.

The precipitation step is governed by the different solubility of the two polymers in their common solvent. Based on the Hildebrand solubility parameters,

δ, of EL (δ_{EL} = 20.2 MPa$^{1/2}$) [Barton, 1991], PCL (δ_{PCL} = 19.7 MPa$^{1/2}$) [Bordes et al., 2010] and PEO (δ_{PEO} = 20.2 MPa$^{1/2}$) [Yuan, 1999], it can be assumed that PEO is more soluble in EL than PCL. Taking this aspect into account, and considering that the weight fraction of PCL is always higher than that of PEO, it can be assumed that PCL is the first polymer to reach supersaturation and condense, forming structures with different characteristic size scales, while PEO is still swollen by the solvent. At this point, further solvent evaporation is required for PEO to solidify, possibly leading to a collapse of PEO to a level below the already vitrified phase.

The different morphologies obtained varying the blend composition lead to dissimilar textural features of the final films, evidenced in Figure 6.17 and by the topographical parameters reported in Table 6.3. Both *Sq* and *Sdr* are found to increase with increasing PEO concentration, the values of *Ssk* being intermediate between those of the homopolymers. At low PEO contents, the film texture resembles that of the PCL matrix: this is evidenced by the same values of *Sq* and

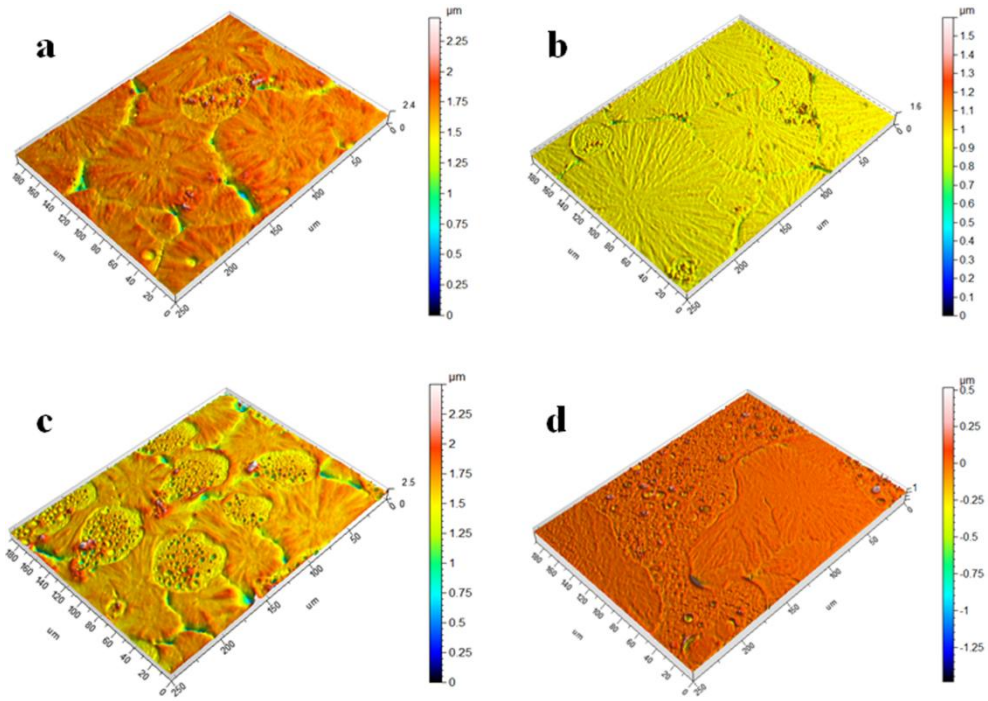

Figure 6.17 – Surface topographies of films of unfilled PCL/PEO blends at different compositions: (a) 90/10, (b) 80/20, (c) 70/30, (d) 60/40.

Table 6.3 – Textural features of the unfilled PCL/PEO blend films.

PCL/PEO weight ratio	*Sq* [µm]	*Sdr* [%]	*Ssk*
90/10	0.03	0.05	- 1.0
80/20	0.30	0.48	- 1.5
70/30	0.72	1.8	0.01
60/40	1.07	1.7	- 0.18

Sdr shared by the PCL/PEO blend at weight ratio 90/10 and the PCL sample obtained in the same processing conditions (cf. Figure 6.11b and Table 6.2). As the PEO concentration is increased, the topography of the surface becomes more complex. In particular, the considerable increase in roughness and specific surface of the samples at high PEO content reflects the presence of a large number of concave, micron-sized PCL domains inside the PEO-rich phase (see Figure 6.17d).

6.4 Formation and surface structures of biphasic polymer films – Effect of nanoparticle incorporation

The previous investigation on the unfilled PCL/PEO systems provides the bases for studying the effects of the incorporation of nanoparticles on the surface morphology of polymer blend films. Specifically, the attention has been drawn to PCL/PEO samples at weight ratio 60/40, filled with four kinds of nanoparticles that differ among them in terms of geometrical and surface features: hydroxyapatite (HA), a hydrophilic, biocompatible filler widely used for the reinforcement of bio-based polymers [Aronov et al., 2006; Salerno et al., 2014]; aluminum-magnesium layered double hydroxide (LDH, also known as hydrotalcite), a synthetic clay consisting of stacks of individual platelets, whose surface is made hydrophobic by an organic modifier [Lv et al., 2007]; titanium dioxide particles characterized by hydrophilic (untreated, P25) and hydrophobic (silanized, T805) surfaces, respectively [Cai et al., 2012; García-González et al., 2009a]. From this point forward, unless otherwise specified, the discussion will always be focused on PCL/PEO blends at weight ratio 60/40; the compositional indication will then be omitted in this chapter.

First of all, the degree of dispersion of the fillers in the pristine solutions has been investigated. Representative optical micrographs of systems at 5 wt% of filler concentration soon after ultrasonication are shown in Figure 6.18. The best level of dispersion of attained for hydrophilic nanoparticles (HA and P25), while the hydrophobic ones (LDH and T805) appear in the form of aggregates of tens of microns. Taking into account the marked polar feature of the solvent, this finding is not surprising. Afterwards, the solvent begins to evaporate and the concentration of the polymers gradually increases. The consequent alterations in polarity and viscosity of the suspending medium affects the nanoparticle dynamics, which in turn influence polymer phase separation. As a result of this complex interplay, the final film morphology may deviate from what expected on the basis of straightforward thermodynamic considerations.

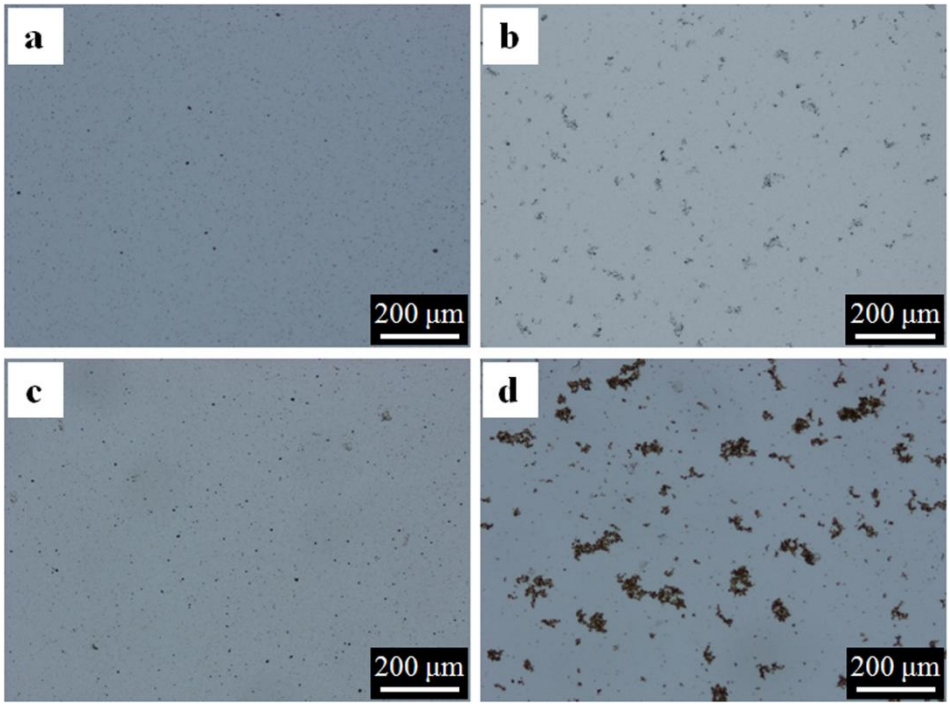

Figure 6.18 – Optical micrographs of nanofilled polymer solutions (filler concentration: 5 wt% with respect to the polymer blend) acquired soon after the ultrasonication step. Kinds of filler: (a) HA, (b) LDH, (c) P25, (d) T805. Nanoparticles and their aggregates appear as dark zones dispersed into the brighter suspending fluid.

Some examples of the transient morphologies exhibited by the nanofilled blends during solvent evaporation are shown in Figure 6.19. These snapshots shed light on the uneven distribution of the filler when the polymer phases begin to separate. At this intermediate stage of the process, all the kinds of nanoparticles seem to predominantly enrich the continuous PEO phase. Aggregates are clearly detectable in the case of hydrophobic fillers, while substantial differences emerge between the hydrophilic ones. Indeed, the inter-particle attractive van der Waals interactions result in the formation of isolated micron-sized HA flocs and a space-filling network of P25 particles; the arrangement of the polymer phases is affected by such dissimilar filler structures, the P25 network embedding small PCL domains.

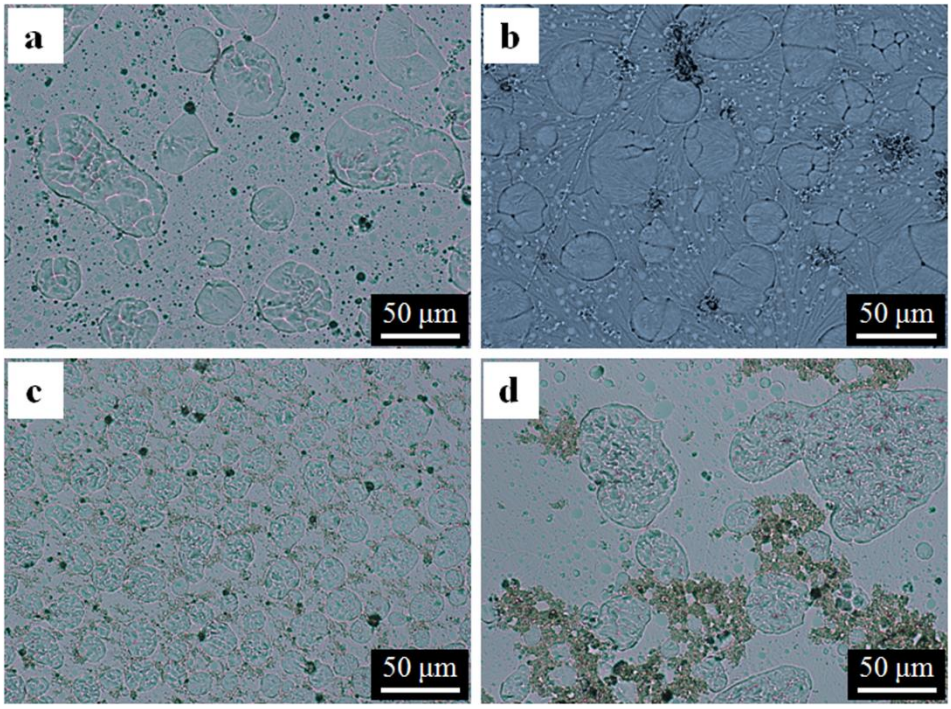

Figure 6.19 – Optical micrographs of nanofilled polymer solutions (filler concentration: 5 wt% with respect to the polymer blend) acquired during the solvent-casting process. Kinds of filler: (a) HA, (b) LDH, (c) P25, (d) T805.

Figure 6.20 and 6.21 show optical micrographs of representative blend samples with filler concentration of 3 and 5 wt% respectively; the results of the domain size measurements are reported in Figure 6.22. At the lowest filler content, HA, P25

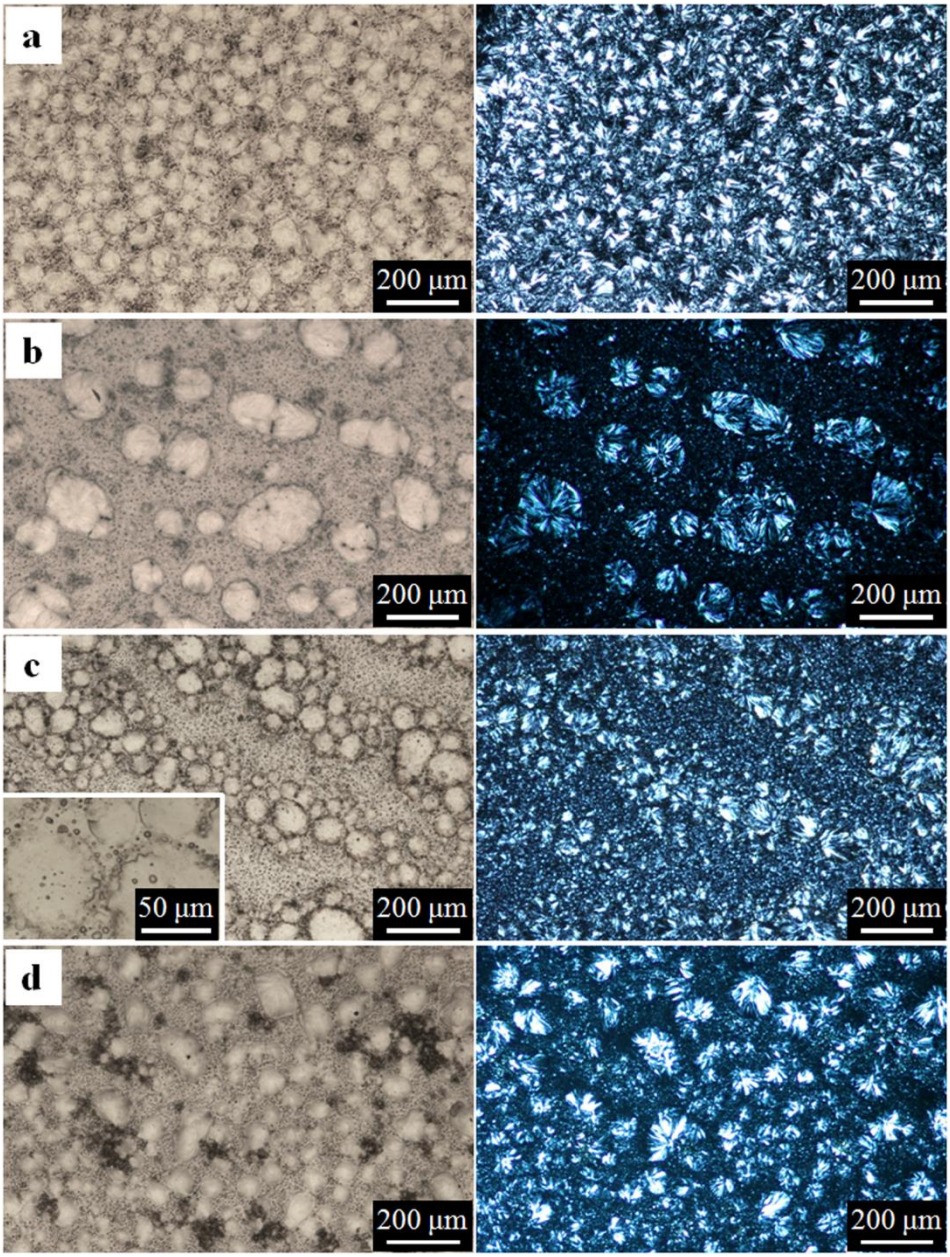

Figure 6.20 – Optical micrographs (in direct and transmission mode and different magnifications) of PCL/PEO blend samples (weight ratio 60/40) filled with 3 wt% of (a) HA, (b) LDH, (c) P25 and (d) T805.

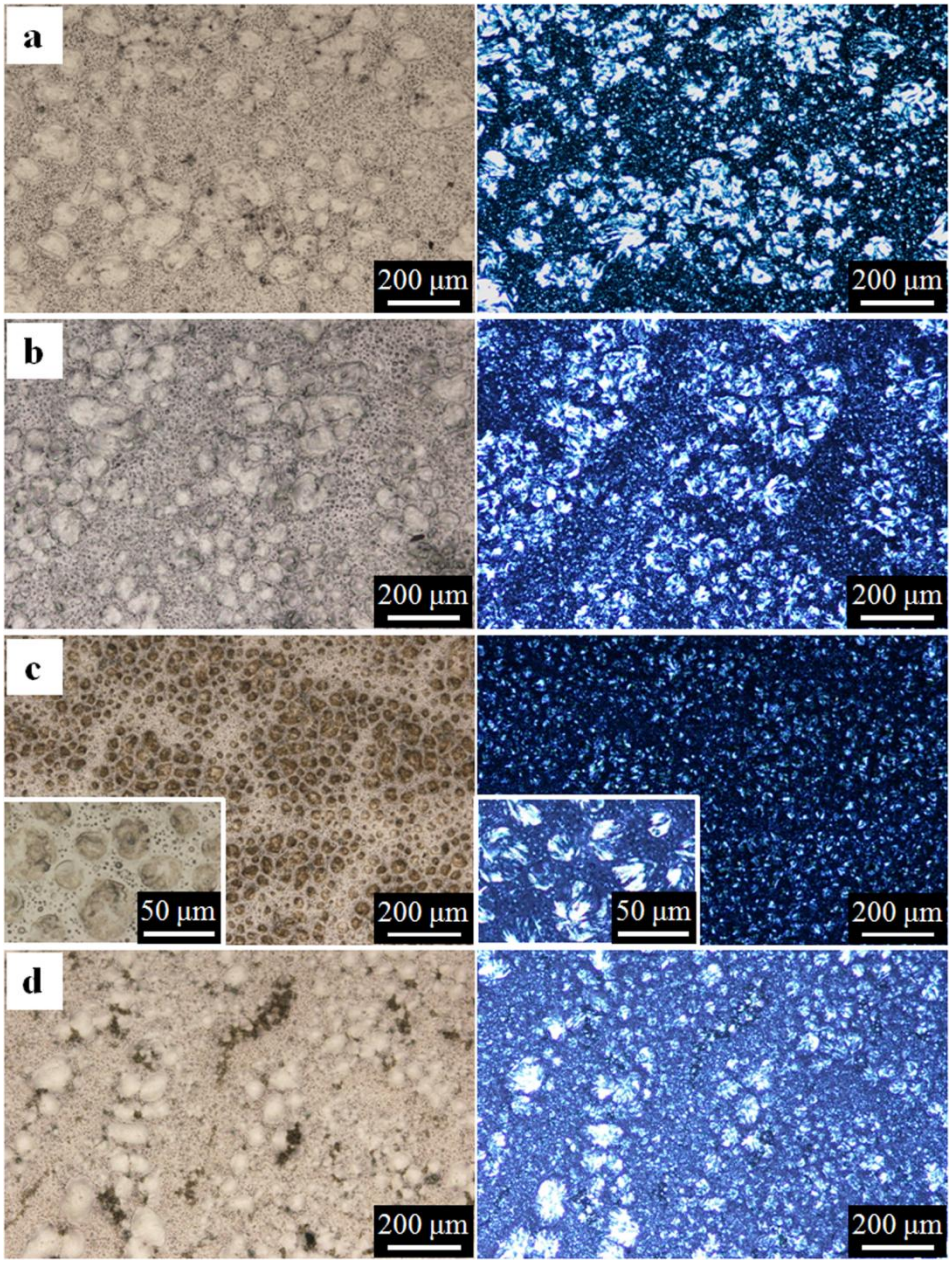

Figure 6.21 – Optical micrographs (in direct and transmission mode and different magnifications) of PCL/PEO blend samples (weight ratio 60/40) filled with 5 wt% of (a) HA, (b) LDH, (c) P25 and (d) T805.

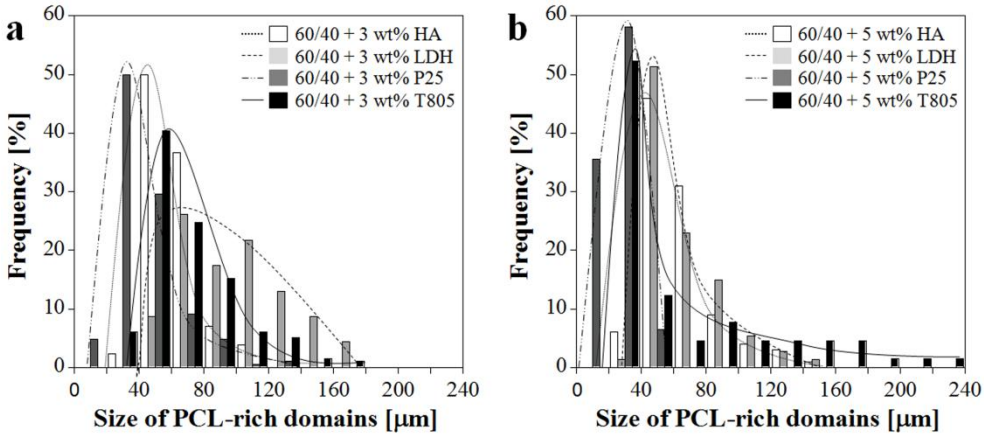

Figure 6.22 – Results of image analysis for the filled PCL/PEO blend films: size distributions of the PCL-rich domains in samples with (a) 3 wt% and (b) 5 wt% filler concentration.

and T805 induce a reduction of the mean size of the PCL-rich phases, whereas the surface morphology is essentially unaltered upon addition of LDH. A refinement of the PCL phase is also detected in all the filled systems at higher particle loading, the size distributions of the PCL-rich domains having a maximum in the range 40÷60 μm. The narrowest distributions are exhibited by the samples filled with bare titania nanoparticles. In particular, the P25-containing blends exhibit a peculiar surface structure, characterized by a pattern of alternated PEO-rich regions and clusters of round PCL domains, which keep their individuality due to the interposition of very thin PEO channels. Conversely, coarser morphologies are observed in the presence of silanized titania nanoparticles, as confirmed by the presence of tails at high size values in the PCL domain size distributions. In such systems, the PEO-rich regions present dark zones which could be ascribed to large filler aggregates. The surface topography of the blend films with 3 and 5 wt% filler concentration of is shown in Figure 6.23 and 6.24, respectively. Confocal analysis highlights that in the filled samples the PCL-rich domains exhibit not only smaller sizes, but also increased height and numerical density in comparison to the unfilled blends. The textural data reported in Table 6.4 indicate that such relief structure results in higher values of *Sdr* without significantly affecting *Sq*.

In order to assess the distribution of the nanoparticles after film settling, EDX spectroscopy has been performed on the final samples. Figure 6.25 shows representative SEM micrographs of the filled blend films with the superposition of

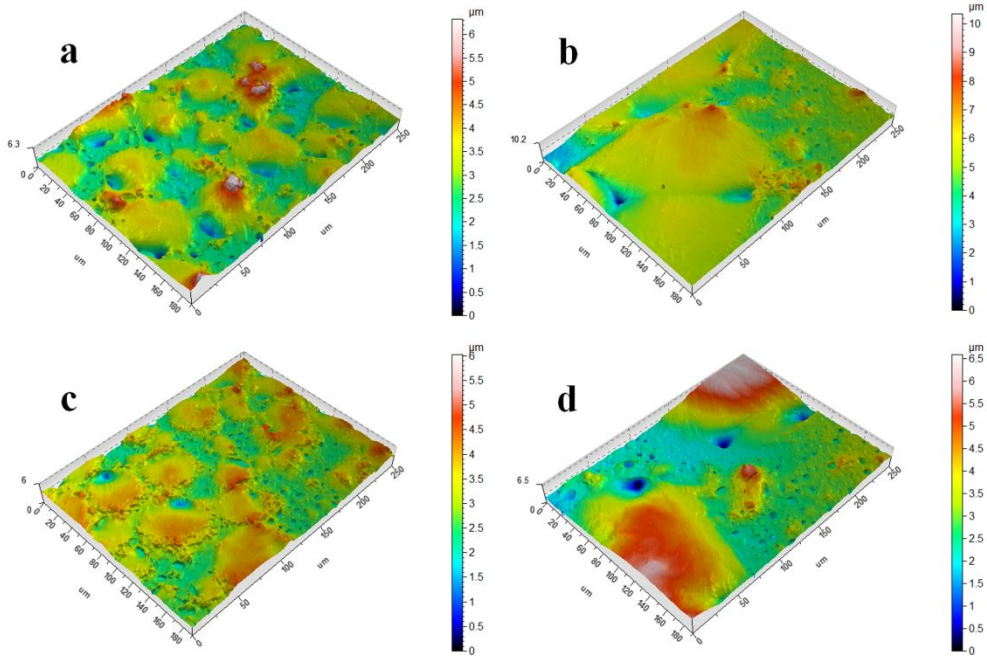

Figure 6.23 – Surface topography of films of PCL/PEO blends with 3 wt% filler concentration. Kinds of filler: (a) HA, (b) LDH, (c) P25, (d) T805.

Table 6.4 – Textural features of the unfilled PCL/PEO blend films.

Sample	*Sq* [µm]	*Sdr* [%]	*Ssk*
60/40 + 3 wt% HA	0.69	3.7	0.51
60/40 + 3 wt% LDH	0.80	3.1	- 0.50
60/40 + 3 wt% P25	0.57	3.5	- 0.19
60/40 + 3 wt% T805	1.15	2.0	0.69
60/40 + 5 wt% HA	0.78	4.2	0.44
60/40 + 5 wt% LDH	0.76	2.5	0.42
60/40 + 5 wt% P25	0.78	1.9	1.1
60/40 + 5 wt% T805	1.12	4.2	0.06

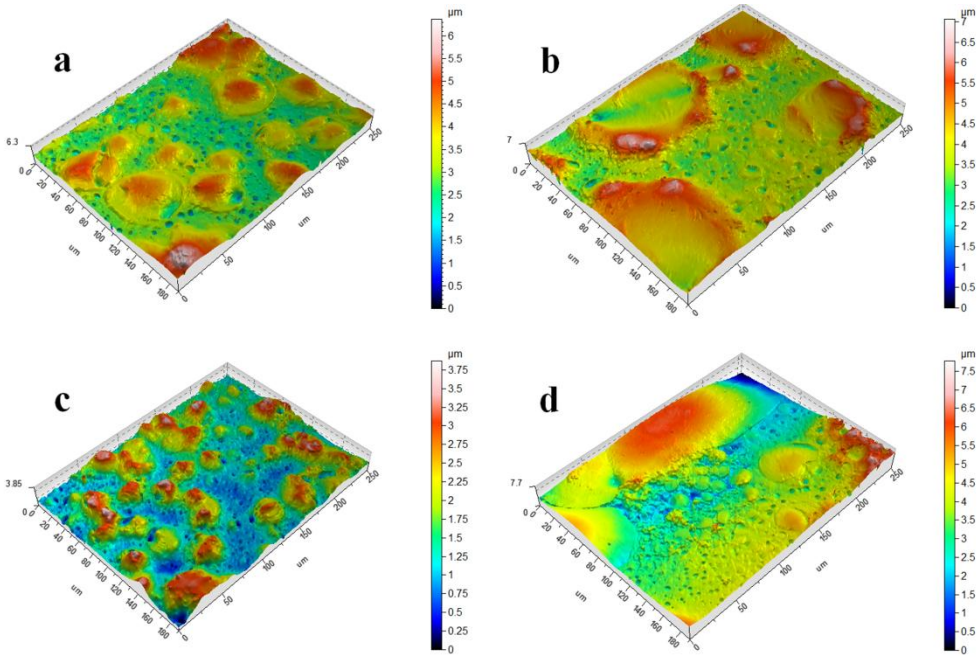

Figure 6.24 – Surface topography of films of PCL/PEO blends with 5 wt% filler concentration. Kinds of filler: (a) HA, (b) LDH, (c) P25, (d) T805.

the corresponding EDX elemental mappings (phosphorus for HA, magnesium for LDH, titanium for P25 and T805). HA exhibits a widespread localization even if the nanoparticles tend to accumulate in the region close to the interface between the polymers (as emerged from the micrograph of the sample containing 5 wt% of HA). Conversely, LDH tends to jam the interface between PEO-rich and PCL-rich domains. Concerning P25, the EDX mapping relative to the sample at the lowest filler loading shows that the particles gather in the thin PEO-rich channels at the interface between PCL-rich domains; such filler pattern is reminiscent of the continuous P25 network illustrated in Figure 6.19c. A similar distribution is also expected at higher filler concentration, even if its assessment is made quite challenging by the considerably fine surface morphology of the blend containing 5 wt% of P25. T805 agglomerates are instead almost exclusively located in the PEO-rich phase. Ultimately, the linear elemental spectra reported in Figure 6.26 corroborate the previous findings, i.e. the preferential localization of LDH, P25 and (with a more heterogeneous distribution) HA at the interface between PEO- and PCL- rich domains and the segregation of T805 in the PEO-rich phase.

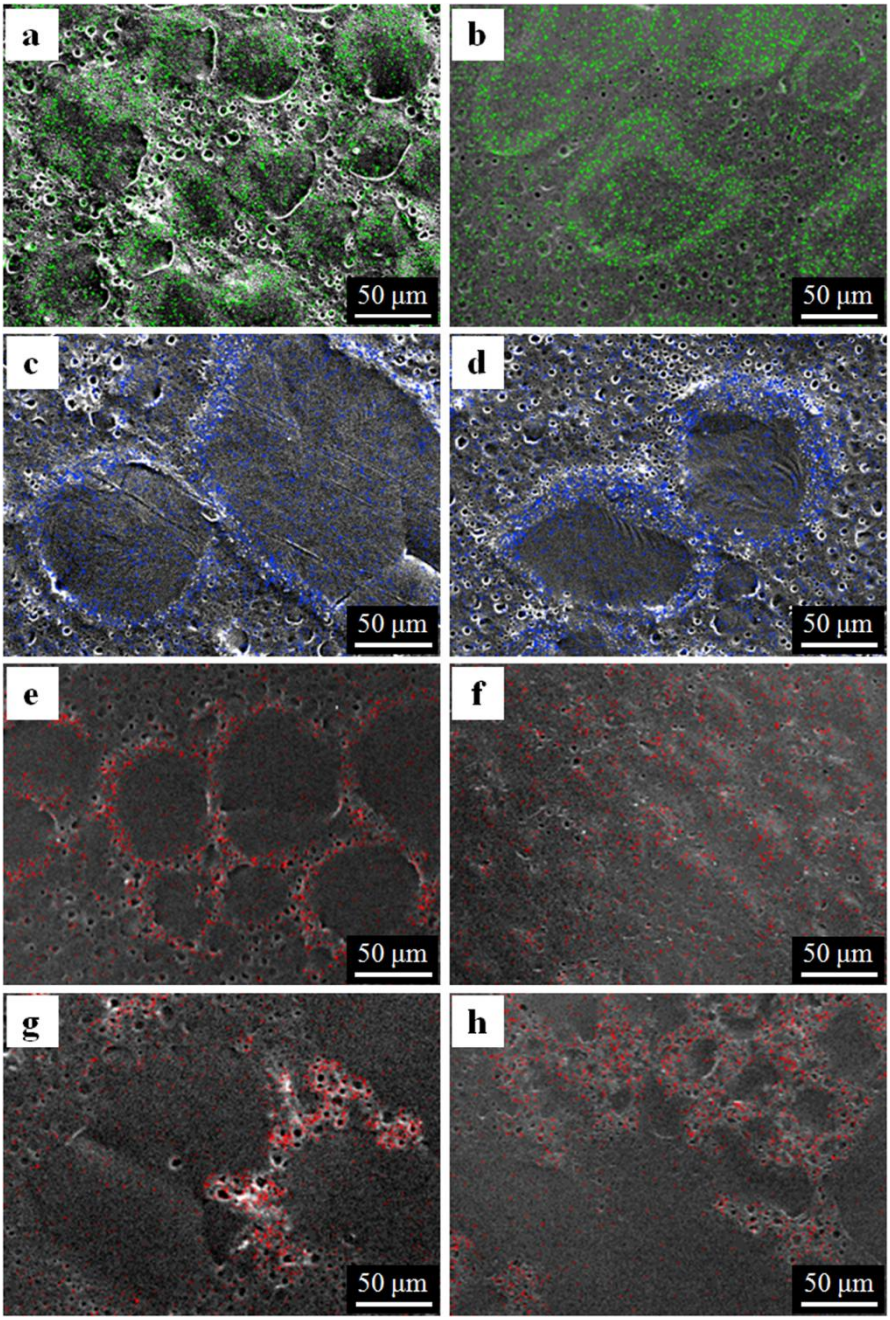

Figure 6.25 – SEM micrographs of filled blend films and X-ray maps of different elements: phosphorus (green) for HA (a, b), magnesium (blue) for LDH (c, d), titanium (red) for P25 (e, f) and T805 (g, h). Filler concentrations: 3 (left column) and 5 wt% (right column).

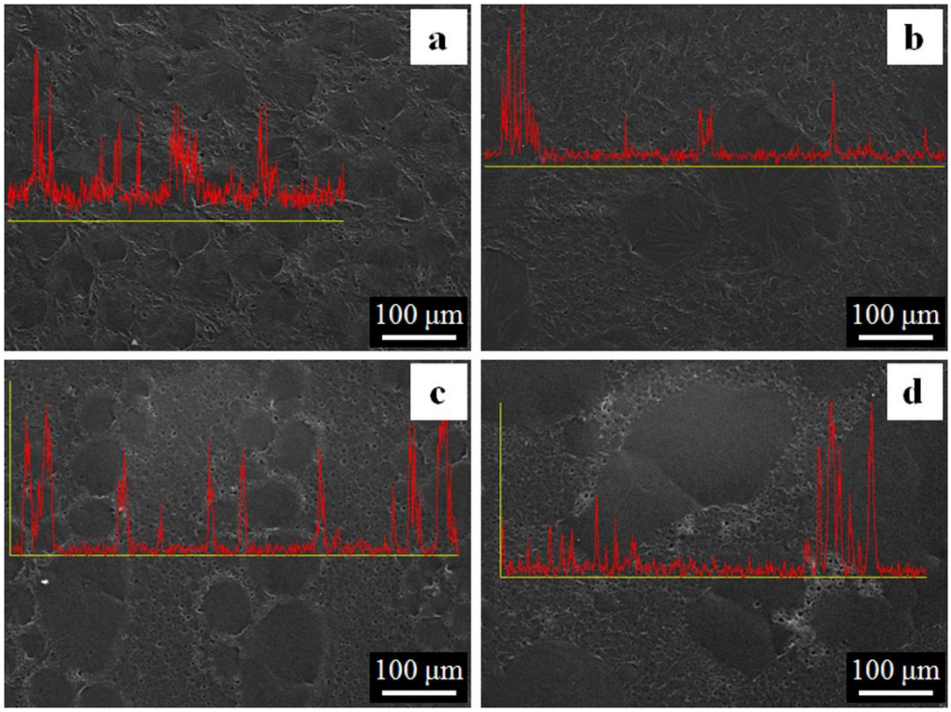

Figure 6.26 – SEM micrographs and linear spectra of the elemental mappings for the PCL/PEO blends filled with 3 wt% of (a) HA, (b) LDH, (c) P25 and (d) T805. The (yellow) lines along which the elemental analysis is performed cross both PCL- and PEO-rich zones.

A general remark that can be made from the results presented so far is that, when incorporating nanoparticles to the starting system, new complexities arise in the development of the morphology of a polymer blend from solvent casting. In particular, the space distribution of the filler is hardly predictable on the basis of those characteristics (such as particle surface chemistry, thermodynamic affinity with the different constituents and polymer molecular conformation) that have been successfully employed dealing with blends prepared trough melt mixing [Al-Saleh et al, 2013]. Due to the mobility of nanoparticles even in highly viscous mediums, the morphology of solvent-cast nanofilled polymer systems derives from a complex interplay among wetting, phase separation and solvent evaporation. If the filler is more affine to one of the components, wetting layers quickly form on the surface of the particles, which hence tend to be included in the more wettable phase and experience strong inter-particle attractions [Araki and Tanaka, 2006]. The uneven positioning of the filler is responsible for a reduction of the chain mobility and an

increase in the viscosity of the preferred phase, reducing the chain mobility. In the system characterized in this study, strong interactions among hydrophobic particles emerge at the very beginning of the casting process due to their low affinity with the polar polymer solution. In particular, spheroidal T805 paricles tend to form larger and less compact agglomerates in comparison with high-aspect- ratio LDH platelets [Hanemann, 2013]. Consequently, during phase separation the filler aggregates tend to sediment, acting as a solid obstacle to the evolution of the morphology of the blend. For instance, when coming into contact with drops of swollen PCL, these aggregates tend to anchor them and enclose smaller droplets in their cavities, arresting their growth because of the interfacial jamming. On the other hand, hydrophilic fillers exhibit better interactions with the host medium and a more regular evolution pattern during phase separation. Only flocculation phenomena of HA have been detected, while for P25 even a 3 wt% loading is enough to promote the further assembly of flocs into a space-filling superstructure. This results in a hindered evolution of the drops of swollen PCL, which are bridged into small PCL-rich crystalline domains once the solvent evaporation is completed. The selective confinement of P25 inside the fine and yet continuous PEO-rich phase corroborates the observation of a filler network bridging the domains of the dispersed constituent. Such arrangement is evidenced in the SEM micrographs of Figure 6.27, where the bright zones correspond to the regions where the particles are localized.

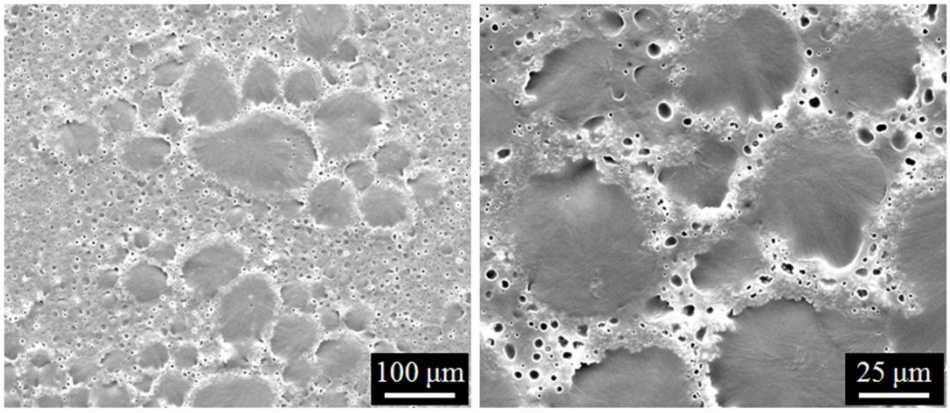

Figure 6.27 – SEM micrographs at different magnifications of the PCL/PEO blend filled with 3 wt% of P25 particles.

To summarize, fillers with different functionalities show a significantly different degree of dispersion in polymeric solutions. As a consequence, the filled systems experience different structural evolutions of the phases, resulting in different final distribution of the particles and surface morphologies. In particular, fillers that are scarcely chemically affine to the host polymer solution tend to aggregate and coarsen the final film microstructure, while particles that guarantee a good initial dispersion are more effective in refining the blend morphologies. The results reported so far, despite being focused on a specific polymer blend, provide useful guidelines for the control of relevant parameters, such as polymer composition and filler characteristics, to tune the morphological and textural features of multiphase polymer films.

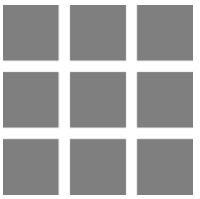

PART III

Perspectives and conclusions

7

Supercritical antisolvent precipitation: a promising route to manipulate the morphology of polymer systems

Apart from the use of nanoparticles, which is the core topic of the present thesis, the performed research activity has also envisaged the exploration of other routes to manipulate the morphology and properties of polymer systems. Supercritical fluids, and especially CO_2, have recently emerged as environmentally and economically valuable aids for the melt and solution processing of polymers. The supercritical CO_2 assisted precipitation of biodegradable polymers is hereinafter discussed and compared with the solvent casting route described in Chapter 6. After introducing the reader to the use of supercritical CO_2 in polymer processing and illustrating the experimental set-up employed (§7.1), meaningful results on homopolymer-based systems and a preliminary investigation on polymer blends are presented (§7.2). The use of CO_2 offers the opportunity to tune the solid-state morphology of the final materials by adjusting the composition of the starting polymer solution and the operating conditions (§7.3).

7.1 Prefatory notes

In the last decades, the exploration by both academia and industry of routes for obtaining polymeric materials with tailored structure and performances has gone along with an increasing interest in overcoming the environmental issues associated with polymer processing. A class of compounds whose usage has proven to be promising in both these senses is that of supercritical fluids.

A supercritical fluid is a substance for which the temperature and pressure are above their critical values, respectively T_c and P_c, and the density is close to, or higher than the critical density ρ_c [Walker et al., 2008]. The supercritical state is characterized, on a characteristic scale of 10-100 Å, by the presence of statistical

clusters with liquid-like structure, surrounded by less dense and more chaotic regions of compressed gas. The number and dimensions of these clusters vary significantly with temperature and pressure, resulting in high compressibility near the critical point. Supercritical fluids can be employed for a wide range of purposes due to their versatility: indeed, their properties, above all density and diffusivity, can be tuned from liquid-like to gas-like or vice versa by slight changes in temperature and pressure.

In the last two decades, the interest in supercritical CO_2 ($scCO_2$) and its potential use for enhancing polymer processing has significantly increased. CO_2 is particularly attractive for being nontoxic, nonflammable, relatively inexpensive, and easily recoverable after processing. Moreover, $scCO_2$ has an easily accessible critical point (T_c = 31.1 °C, P_c = 7.38 MPa, ρ_c = 0.47 g cm^{-3}) [Walker et al., 2008]. Being able to increase the free volume and chain mobility of polymers, $scCO_2$ has proven to affect several key properties such as viscosity, glass-transition and melting points, as well as to drive polymer crystallization [Kazarian, 2000]. Taking advantage of these characteristics, $scCO_2$ has been explored for polymer synthesis and modification, micronization, foaming, blending, and production of polymer nanocomposites [Nalawade et al., 2006]. Concerning polymer blends, morphological refinements can be obtained relying on the different sorption of $scCO_2$ in the phases, which allows to tune the ratio between their viscosities. Indeed, if the solubility of is higher in the more viscous component, the latter will undergo a remarkable viscosity decrease, as reported for PS/PMMA and PS/PE systems [Elkovitch et al., 1999; Lee et al., 2000].

The gas-like viscosity and liquid-like density that ensue from the peculiar molecular structure of $scCO_2$ result in simultaneous high diffusion rates and solvent power [Yeo and Kiran, 2005; Yoganathan et al., 2008]. These features are commonly exploited in the so-called antisolvent precipitation process, which can be carried out in either batch or continuous mode [Elvassore et al., 2001]. In this process, a polymeric solution is brought into contact with $scCO_2$; the latter causes the saturation of the liquid solvent and the consequent precipitation of the solute. Supercritical CO_2 is characterized by a two-order higher diffusivity than liquids, which makes it able to fast diffuse into the solvent. As a result, high solute supersaturation can be reached and, ultimately, polymeric materials with length-scale resolution down to the nanometric scale, hardly achievable using traditional liquid antisolvent processes, can be produced [Hernández et al., 2010].

The potentialities of $scCO_2$ as a polymer processing aid can be exploited in the fabrication of polymeric devices for pharmaceutical and biomedical applications, in

which the possibility of dealing with different solid-state forms is highly desirable in order to tailor the stability and efficiency of the related products as well as their safety. Among the various structures suitable as biomaterials, micron- and submicron-sized polymer particles are commonly used as carriers for cell and drug delivery, while films and foams are employed as scaffolds in tissue engineering [Tang et al., 2004; Salerno et al., 2012]. The use of $scCO_2$ as an antisolvent for polymer/drug precipitation has been widely investigated, as this process allows to obtain several polymer morphologies, such as nano- and micro-particles [Reverchon, 1999; Wu and Li, 2008; Bakhbakhi et al., 2013], fibers [Dixon and Johnston, 1993; Luna-Bárcenas et al., 1995; García-González et al., 2009b], membranes [Cao et al., 2005] and porous scaffolds [Tsivintzelis et al., Fanovich and Jaeger, 2012].

Heat-labile polymers, such as the PCL and PEO used in the activity described in Chapter 6, are among the various biodegradable polymers for which the use of $scCO_2$ could be strategic. Indeed, the $scCO_2$ antisolvent technology requires moderate operating temperatures, which prevent the occurrence of undesired degradation phenomena [Salerno et al., 2014]. Ghaderi and co-workers have investigated the $scCO_2$ antisolvent precipitation of PCL from solution in a mixture of acetone, dichloromethane and isopropanol at 35–40 °C; they have found that tuning the composition of the solvent system and the operating pressure is crucial in order to produce discrete and regularly shaped polymer microparticles [Ghaderi et al., 1999]. Martín and co-workers have reported the co-precipitation of PEO and antioxidants, namely β-carotene and lutein, from solution in dichloromethane by means of compressed CO_2 as antisolvent, observing that different polymer morphologies (particles and films) can be obtained mainly depending on the operating temperature in the range 15-40 °C [Martín et al., 2007]. In these studies, hazardous organic solvents are used, and their substitution with benign alternatives would be highly desirable.

Based on the previous considerations, the $scCO_2$-assisted precipitation of PCL and PEO has been investigated starting from EL and EA solutions has been investigated downline of the activity described in Chapter 6. The effect of several processing parameters (composition of the starting polymer solution, operating temperature and pressure) on the structure of the final materials has been systematically assessed. Even though these investigations fall outside the main topic of this thesis, they are oriented towards the manipulation of the morphology and properties of polymer systems, similarly to the use of nanoparticles discussed so far. Hence, it is believed that presenting the obtained results, and comparing

them with those reported in Chapter 6 for systems produced via conventional solvent casting, would be meaningful in the perspective of drawing guidelines to produce polymeric materials with prescribed structure.

For polymer precipitation, a batch antisolvent process has been conducted in the high-pressure equipment schematized in Figure 7.1. It consists of an autoclave (Thar Design, Pittsburgh, USA), with a cylindrical section and a total volume of about 100 mL, equipped with two sapphire windows for the on-time monitoring of the process, and four electrical resistances located inside the wall of the vessel.

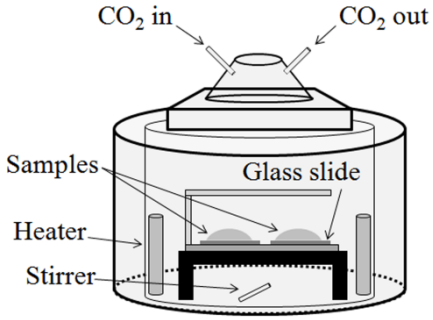

Figure 7.1 – Scheme of the laboratory equipment employed for the scCO_2-aided antisolvent precipitation of PCL, PEO and their blend.

A schematization of the entire apparatus is shown in Figure 7.2: CO_2 is liquefied through a cooling unit, compressed up to the operating pressure by a syringe pump (Teledyne ISCO-260D, Lincoln, USA) and then conveyed to the autoclave to perform the experiments. The flux of CO_2 along the systems is regulated by a number of valves (V1, V2 and V3).

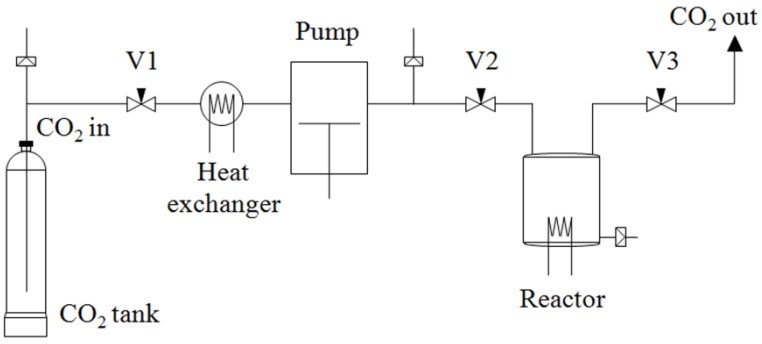

Figure 7.2 – Scheme of the whole high-pressure apparatus used in the scCO_2-aided tests.

The starting polymer solutions have been prepared as described in §6.1. In each test, a drop of solution has been pipetted onto glass slides previously placed onto a teflon support. The latter, provided with an aluminium roofing to prevent the undesired fall of liquid CO_2 onto the specimens, has been subsequently placed inside the vessel, on the top of a metallic support to allow the placement of a magnetic stirrer at the bottom of the vessel (Figure 7.1a). This set-up improves fluids mixing and reduces equilibrium time. After loading and sealing the reactor, the temperature has been raised up to the operating value (either 40 or 50 °C) and CO_2 has been concomitantly pumped inside the vessel up to the operating pressure (either 10 or 20 MPa). The system has then been mantained at the selected operating conditions for 15 minutes; finally, the vessel has been slowly vented to the atmosphere in order to prevent CO_2 from passing through the liquid state and avoid possible foaming of the samples. It is important to point out that, at the selected operating temperature and pressure, the molar fraction of the solvent is in the range of $10^{-3} \div 10^{-4}$ with respect to CO_2. In these conditions, the solvent and CO_2 form a supercritical mixture. Taking into account these aspects, even if the amount of residual solvent in the samples has not been assessed we may consider that, after vessel venting, the eventual solvent residue is negligible and should not induce significant changes in the morphology of the samples.

The solubility of $scCO_2$ in PCL and PEO has been evaluated by assessing the weight gain of the polymers at selected processing conditions. The samples in powder form have been weighed and placed in a home-made high pressure system consisting of a 25 mL vessel (112S, Headline Filters, Aylesford, UK) with a high-pressure valve (SW4071, Autoclave Engineers, USA). The system has been immersed in a thermostatic bath set to either 40 or 50 ºC and pressurized with $scCO_2$ at either 10 or 20 MPa. The solubilization step has lasted for 60 min, then the vessel has been rapidly cooled at 0 °C and kept at this temperature for 5 min. Finally, the vessel has been vented by opening the valve and the samples have been weighted in a high-precision balance (CPA225D, Sartorius, Gottingen, Germany) to record the weight gain. The reported data are the average of 3 specimens.

The morphological and textural features of the final samples have been characterized by means of optical, confocal and scanning electron microscopy as described in §6.1.

7.2 Supercritical CO_2 induced morphologies of mono- and biphasic polymer systems

The solubility of $scCO_2$ in both PCL and PEO is significantly affected by the operating conditions, as inferable from the results of carbon dioxide sorption experiments reported in Table 7.1. In summary, the solubility of $scCO_2$ increases with pressure and decreases with temperature, being higher in PCL rather than in PEO materials. Regarding the state of the samples at the end of the tests, single PCL bulks have been found under all the experimental conditions; on the contrary,

PEO has been found in the form of fine particles after the tests at 40 °C, while blocks of partially fused particles have been recovered after processing the material at 50 °C. These results are in good agreement with those reported for PCL [Tsivintzelis et al., 2007; Salerno et al., 2014] and PEO [Champeau et al., 2014].

Table 7.1 – Solubility of $scCO_2$ in PCL and PEO at different operating conditions.

Operating conditions	**$scCO_2$ sorption concentration [wt%]**	
	PCL	PEO
40 °C, 10 MPa	25.4 ± 1.2	17.5 ± 2.5
40 °C, 20 MPa	28.1 ± 1.4	21.6 ± 3.4
50 °C, 10 MPa	23.3 ± 1.1	10.1 ± 1.1

The morphology of PCL samples obtained from EL solutions via $scCO_2$ antisolvent precipitation at 40 °C and either 10 or 20 MPa is shown in Figure 7.3. At low polymer concentration, separated drop-shaped precipitates can be noticed irrespective of the operating pressure. With increasing polymer content, at 10 MPa the average size of the domains increases, while at 20 MPa the droplets coalesce, eventually forming a continuous and yet pierced film. Similar structures (not shown) have been obtained from EA solutions.

As shown in Figure 7.4, the morphology of the precipitates completely changes when the drying temperature is increased up to 50 °C while keeping the pressure equal to 10 MPa. Indeed, continuous films form except from EL solution at the lowest polymer concentration, for which macroscopic holes are noticed (Figure 7.4d). Differently from the samples obtained through conventional solvent casting (cf. Figure 6.7), the antisolvent-precipitated films exhibit a bimodal size distribution of the crystallites.

Analyzing the optical images has allowed to quantify the size of the spherulites; the results are summarized in Figure 7.5. While increasing the polymer concentration from 2 to 10 wt/vol% halves the average spherulite size in both the EL and EA cast films (cf. Table 6.1), weaker and generally less clear trends are recorded for both the small and large domains observed in the antisolvent-precipitated samples. The larger spherulites are comparable in size with the crystallites of the solvent-cast films; a marked difference is detected in the EA systems at the highest polymer concentration.

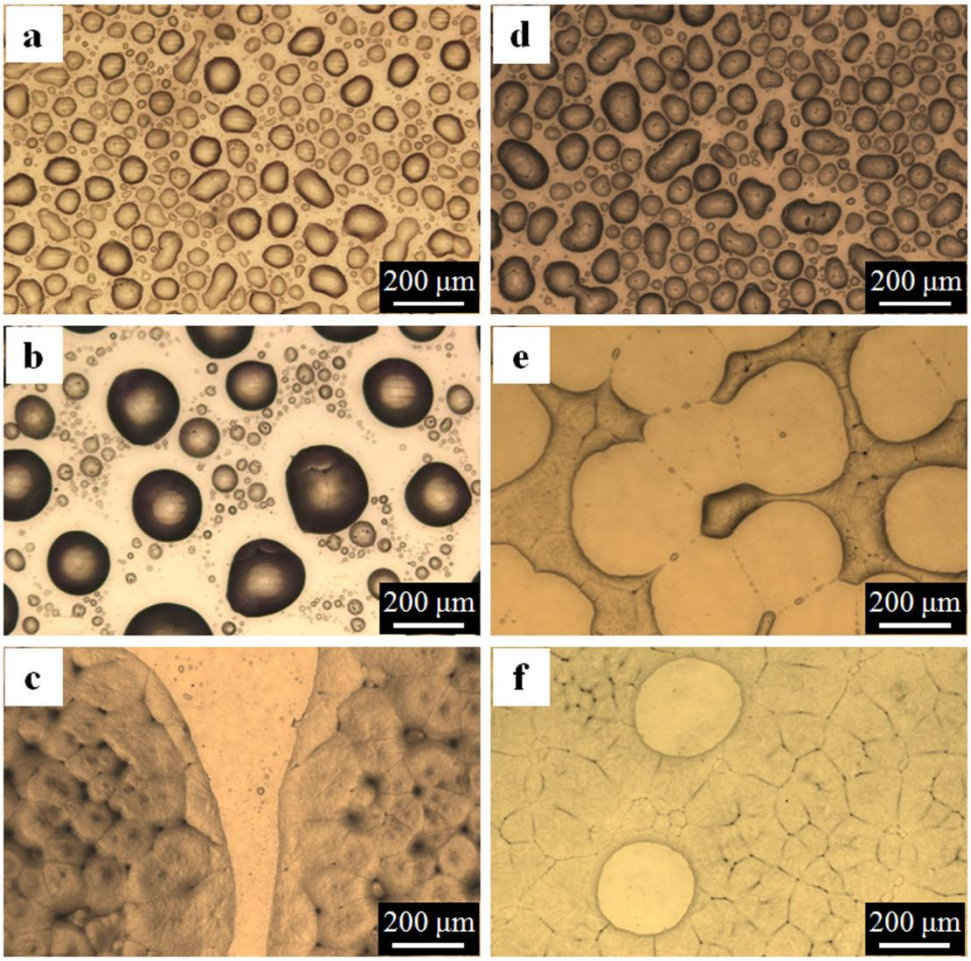

Figure 7.3 – Optical micrographs of PCL samples prepared from EL solutions by $scCO_2$ antisolvent precipitation at (a-c) 40 °C and 10 MPa and (d-f) 40 °C and 20 MPa (polymer concentrations: 2, 5, 10 wt/vol%). The images acquired in transmission mode are reported in Appendix A.5.

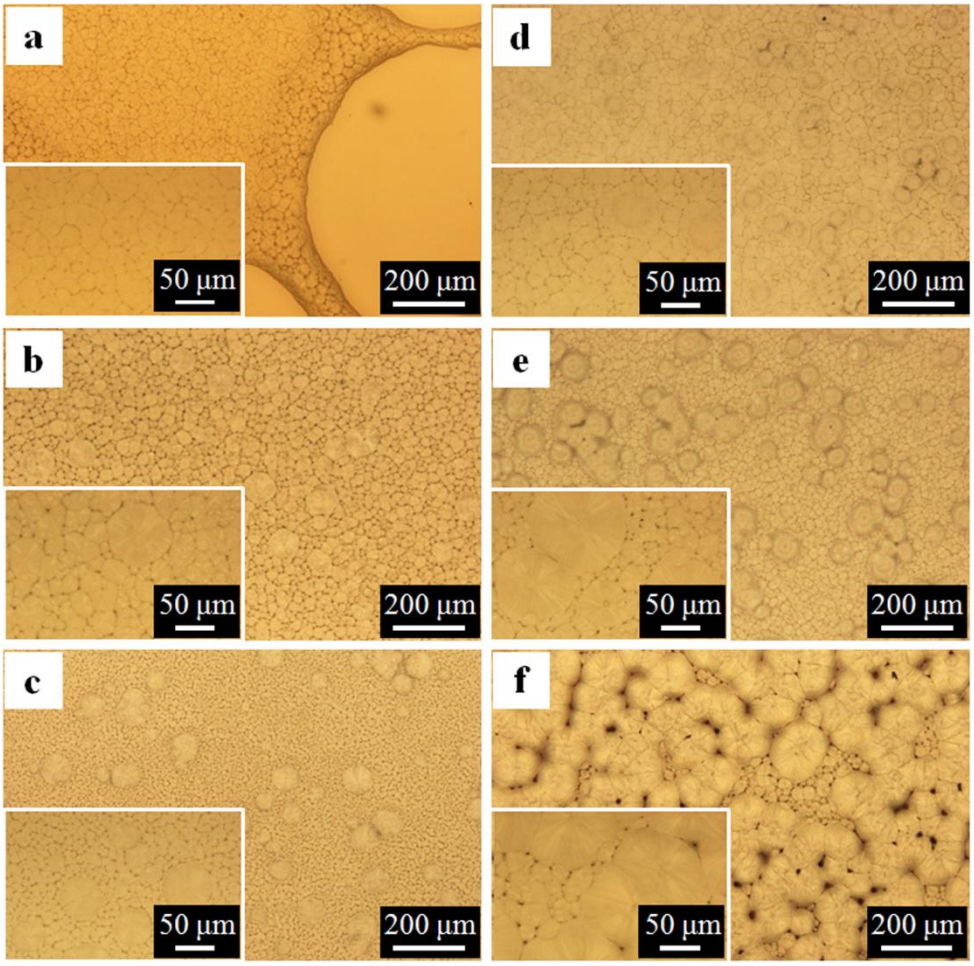

Figure 7.4 – Optical micrographs of PCL samples prepared at 50 °C and 10 MPa from (a-c) EL solutions and (d-f) EA solutions (polymer concentrations: 2, 5, 10 wt/vol%). The images acquired in transmission mode are reported in Appendix A.5.

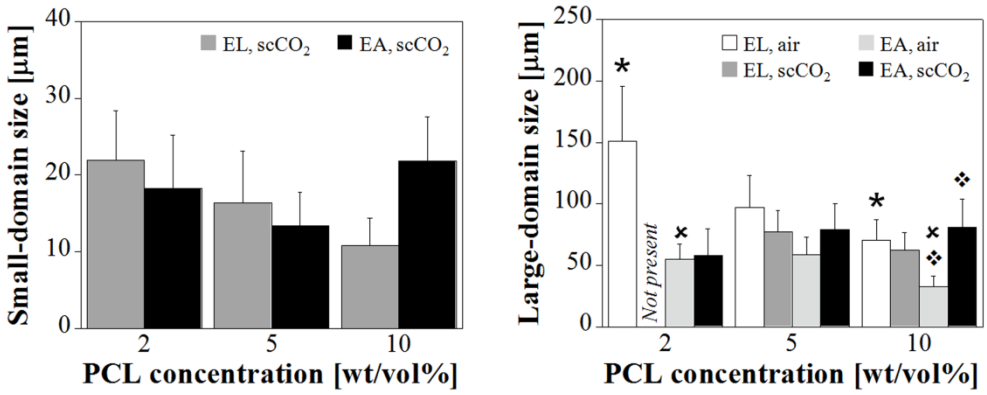

Figure 7.5 – Average spherulite size for the solvent-cast and antisolvent-precipitated PCL samples prepared from EL and EA solutions. The symbols (asterisks, crosses and diamonds) above the histogram bars designate sets of statistically significant data (p<0.01).

Concerning PEO, the morphology of samples prepared by $scCO_2$ drying from a 10 wt/vol% solution in EL is shown by the SEM micrographs of Figure 7.6. For all the samples, the formation of continuous films with surface features that resemble those of the air-dried counterparts is observed (cf. Figure 6.8a-c).

Very peculiar morphologies, reported in Figure 7.7, are observed for the antisolvent-precipitated samples from EA solutions. In particular, when the process is carried out at 40 °C the PEO precipitates in the form of porous particles irrespective of the operating pressure. The characteristic size of such particles is in the range 10^1-10^2 µm, as reported in Table 7.2. The increase of PEO concentration in the pristine solution generally results in the formation of particles of bigger size; the trend with pressure is instead less regular. At 50 °C and 10 MPa, the formation of continuous films is systematically observed (Figure 7.8), as in the case of PCL-containing solutions. The spherulitic morphology that develops at 10 wt/vol% of PEO is similar to that of its EL counterpart.

Promising results have also been obtained for multiphase polymer systems. Figure 7.9 shows optical images of PCL/PEO blend films with weight composition 60/40, obtained from EL solutions by supercritical antisolvent precipitation at 50 °C and 10 MPa. Using supercritical CO_2 to assist the formation of the blend seems to have a relevant effect of the structure of the system. Indeed, the PCL-rich phase is finer, and apparently interpenetrated with the PEO-rich one, compared with its counterpart in the sample obtained via conventional solvent casting (cf. Figure 6.13d). The study of multiphase systems, however, is currently at an early stage.

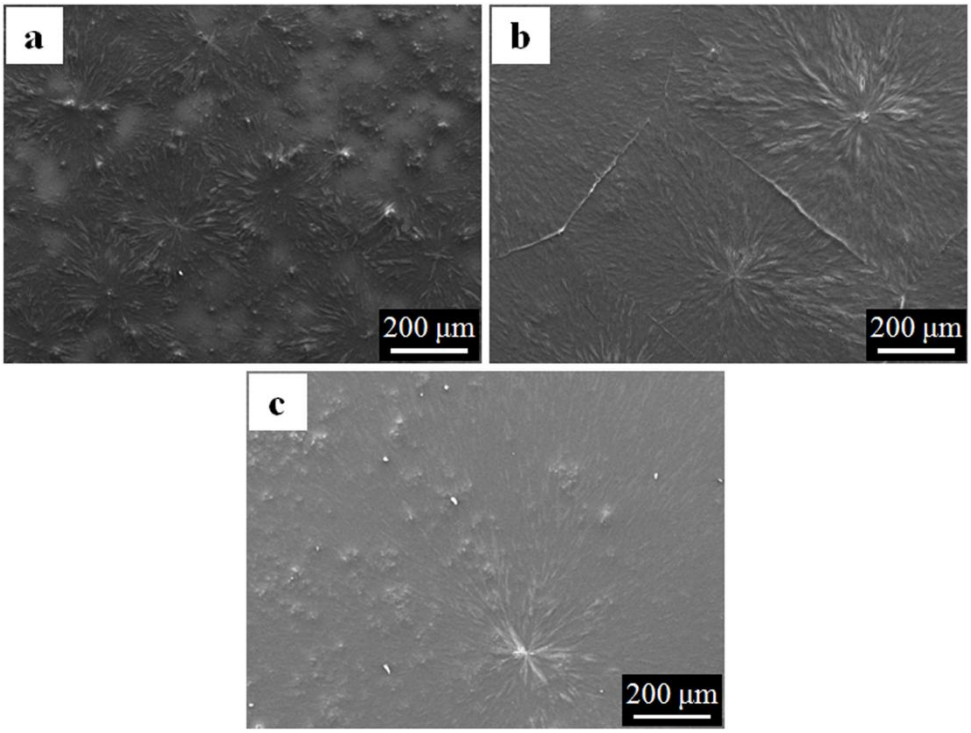

Figure 7.6 – SEM images of PEO samples prepared from EL solutions by antisolvent precipitation at (a) 40 °C and 10 MPa, (b) 40 °C and 20 MPa and (c) 50 °C and 10 MPa.

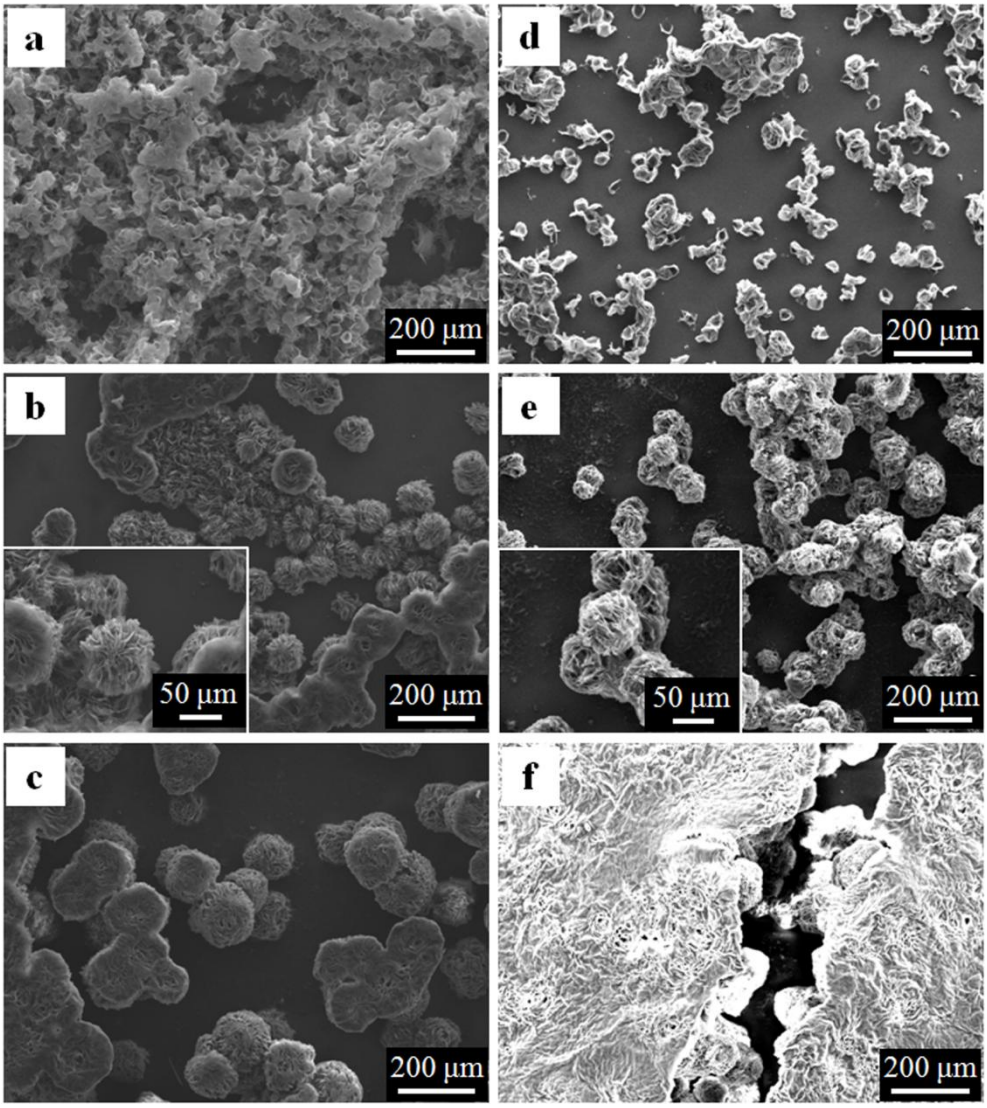

Figure 7.7 – SEM micrographs of PEO samples prepared from EA solutions by supercritical antisolvent precipitation at (a-c) 40 °C and 10 MPa and (d-f) 40 °C and 20 MPa (polymer concentrations: 2, 5, 10 wt/vol%).

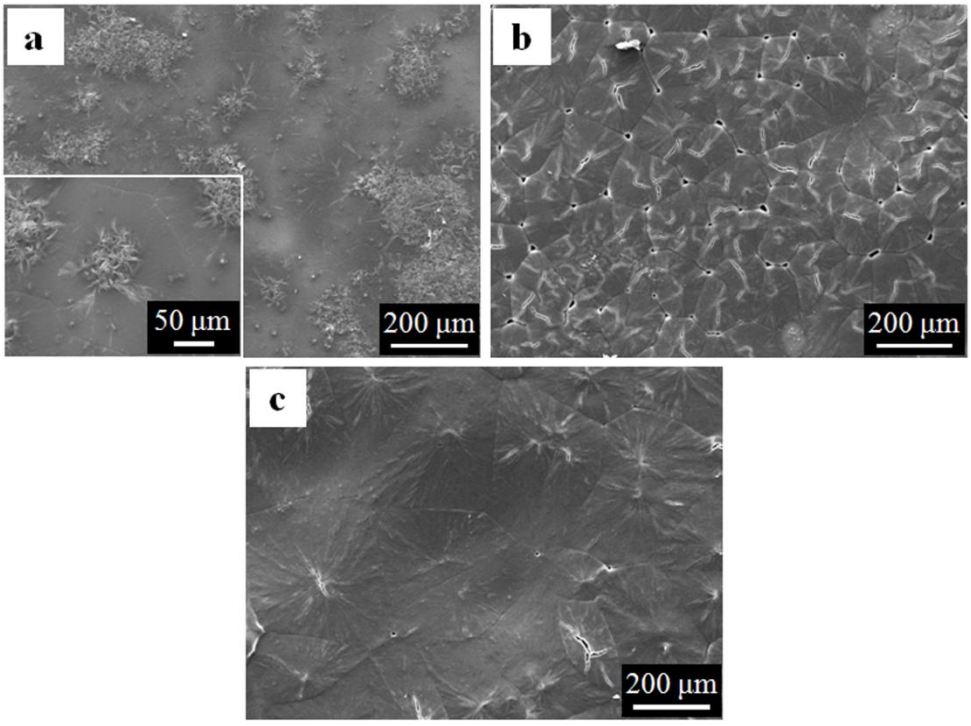

Figure 7.8 – SEM micrographs of antisolvent-precipitated PEO samples prepared at 50 °C and 10 MPa from EA solutions (polymer concentrations: 2, 5, 10 wt/vol%).

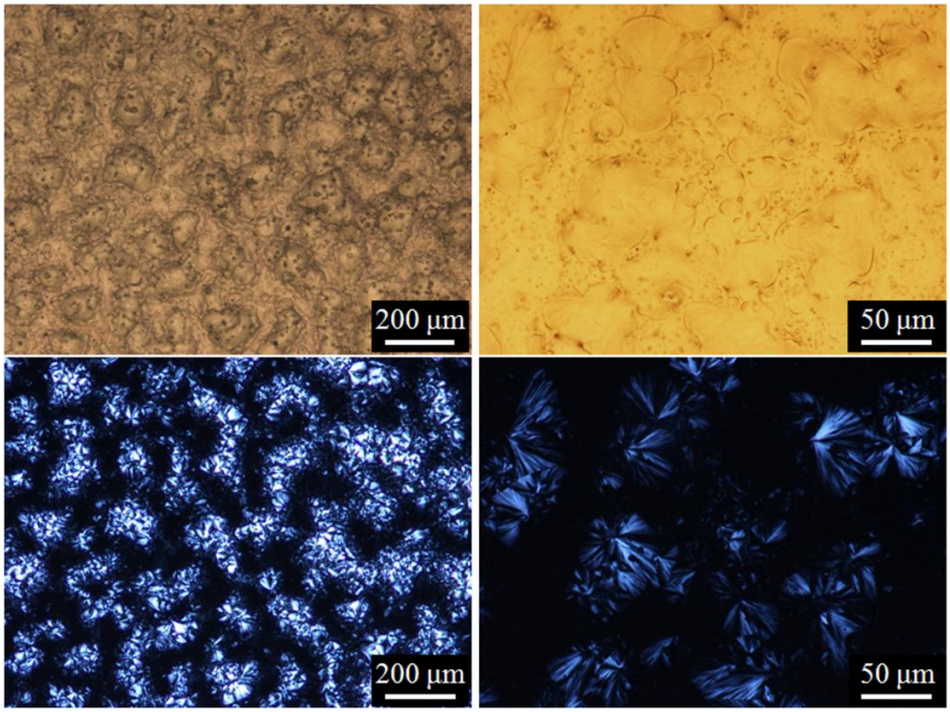

Figure 7.9 – Optical micrographs (in direct and transmission mode and different magnifications) of a PCL/PEO blend with weight composition 60/40, obtained from an EL solution (polymer concentration 5 wt/vol%) through supercritical antisolvent precipitation at 50 °C and 10 MPa.

7.3 Insight into supercritical antisolvent precipitation: effect of material- and process-related parameters

Before discussing the reported results, it is worth describing in detail the different steps of the antisolvent precipitation batch process conducted here. A drop of polymer solution deposited onto a glass substrate is put into contact with CO_2 which gradually passes from gaseous to supercritical state. In the pressurization step, solvent extraction and phase separation progressively occur in the solution. Indeed, the organic solvent, being miscible with CO_2, gradually loses its density and solvation power, causing supersaturation and subsequent precipitation of the polymer, which is instead insoluble in CO_2 [Wu and Li, 2008]. In the case of semi-crystalline materials such as PCL and PEO, the precipitates are crystal nuclei which are able to grow further incorporating solute molecules as the removal of the

solvent proceeds. Besides mixing with the organic solvent, CO_2 is able to concomitantly diffuse into the polymer phase; as a result, the free volume of the polymer increases and its melting temperature decreases, finally leading to polymer plasticization [Salerno et al., 2014]. Such plasticization effect may promote partial or complete melting and subsequent recrystallization of the crystalline domains formed during the precipitation process. Under certain processing conditions, coalescence of the precipitates is also observable, with relevant implications on the microstructure of the resulting polymer systems. In the light of the previous considerations, it is clear that the $scCO_2$ antisolvent precipitation of semi-crystalline polymers is a highly complex process in which many phenomena are involved, such as two-way mass transfer (solvent extraction and antisolvent sorption in the polymer), crystal nucleation and growth, and possible recrystallization [Luna-Bárcenas et al., 1995].

Aiming to assess the process-structure-property relationship of semicrystalline PCL and PEO systems prepared using $scCO_2$ antisolvent precipitation, the working conditions have been selected within a moderate range of the supercritical zone. In particular, the 40÷50 ºC operating temperature range is lower than the melting points of the pure polymers, while the selected pressure range is easily accessible for both laboratory and large-scale production equipments. The selected experimental design allows to highlight the differences between solvent-cast (cf. §6.2) and antisolvent-precipitated polymer samples and to assess how their morphology and structure is affected by the processing parameters, namely type of solvent, polymer concentration, operating temperature and pressure.

The first key parameter to discuss is the nature of the solvent. The results of the $scCO_2$-assisted experiments demonstrate that the choice of the organic solvent is crucial in dictating the way the polymer precipitates during phase separation, and the subsequent morphological evolution. In particular, solvent polarity, a measure of which is given by the relative dielectric constant ε_r, is believed to be a relevant parameter [Sacha et al., 2006]. EA is less polar than EL and, hence, more chemically affine to the CO_2 molecule, which does not have a molecular dipole moment but only a quadrupole moment. Such enhanced affinity accelerates the removal of EA from the the liquid solution and the subsequent precipitation of crystalline nuclei. The interactions between the polymer and the solvent-antisolvent mixture which gradually forms during the process also affect the kinetics of polymer precipitation [Reverchon, 1999]. The effect of the used solvent does not clearly emerge when considering the hydrophobic PCL samples produced at the operating temperature of 40 °C. In this case, the similar final morphologies (either

discrete or continuous depending on polymer concentration; see Figure 7.3 and 7.4) could be ascribed to the occurrence of partial melting and recrystallization of the spherulites that might level off the structural differences deriving from the use of different solvents. On the other hand, when dealing with the samples processed at 50 °C, i.e. about 10 °C below the melting temperature of PCL at atmospheric pressure, the films manufactured from EA systems exhibit a higher number of large crystals with respect to their EL-based counterparts (Figure 7.4). It can be reasonably assumed that larger PCL spherulites are present in the EA samples before the CO_2-induced melting and recrystallization as a consequence of the high solvent-antisolvent affinity and enhanced crystal growth. Concerning PEO, which is a hydrophilic polymer, the effect of the type of solvent is even more pronounced. A white discontinuous precipitate has been noted in the EA solutions already during the pressurization step. Such a fast phase separation is ascribable to the low affinity between the water-soluble polymer and the almost apolar solvent-antisolvent mixture, which leads to the rapid formation of microparticles that only undergo minor modifications during the remaining part of the process. Continuous PEO structures are possible when considering a high polymer concentration or high operating temperatures (Figure 7.6 and 7.8). On the other hand, the time required for the extraction of the more polar EL is much higher due to a greater polymer-solvent affinity, eventually leading to the merging of the precipitate into continuous films (see Figure 7.6). Concerning the PCL/PEO blend films, the peculiar morphology obtained via supercritical antisolvent precipitation can be ascribed to the different affinities of PCL and PEO with the solvent-antisolvent mixture.

In a further step, the influence of the concentration of polymer in the pristine solution on the antisolvent precipitation process is considered. The role played by this parameter has been assessed in works which deal with different semicrystalline polymer structures, such as particles [Elvassore et al., 2001] and fibres [Luna-Bárcenas et al., 1995]. With increasing polymer concentration in the solution, Dixon and Johnston have found a transition from discrete to continuous polyacrylonitrile morphologies, while Bakhbakhi et al. have recently noticed an increase of the dimensions of polylactic acid particles [Dixon and Johnston, 1993; Bakhbakhi et al., 2013]. The time required for the precipitation process is proposed to play a dominant role in determining the final polymer structure. In particular, supersaturation is achieved faster at high solute concentrations, resulting in increased time for crystal growth. Regarding samples studied here, the dimensions of the discrete PCL crystalline domains formed at 40 °C increase with increasing polymer concentration, ultimately leading to quasi-continuous structures at 10

wt/vol% (see Figure 7.3). The greater propensity to precipitate in the form of large crystals also emerges when the operating temperature is raised up to 50 °C, that is closer to the melting point of PCL (see Figure 7.4). Specifically, the fraction of large spherulites increases with polymer concentration, which is indicative of the aforementioned prevalence of growth over nucleation phenomena. It is worth noting that such a trend is opposite with respect to the samples produced via conventional solvent casting, for which a decrease in spherulite size with increasing PCL concentration has been ascribed to the viscosity-limited growth of the crystalline nuclei during solvent evaporation (cf. §6.1.2). As far as PEO is concerned, morphological variations in the samples obtained by $scCO_2$ antisolvent precipitation from EL solutions are hardly detectable due to the large crystal dimensions, whereas a significant effect is noticed in the EA systems. Indeed, the size of the microparticles obtained at the operating temperature of 40 °C increase with increasing polymer concentration (Figure 7.7). This can be explained by considering again that supersaturation is reached faster at high solute concentration, hence, the precipitated nuclei have more time to grow and give rise to large particles [Bakhbakhi et al., 2013].

Next, the effect of the temperature and pressure conditions at which the $scCO_2$-assisted precipitation process is carried out is discussed. These two operating parameters are important factors to take into account as they affect the solubility of the compressed antisolvent into the polymer phase. In general, $scCO_2$ sorption in polymers increases at high pressure, due to the enhanced driving force for $scCO_2$ diffusion, and decreases with increasing temperature as a consequence of the lower $scCO_2$ density [Fanovich and Jaeger, 2012]. For semi-crystalline polymers, such as those used in this work, CO_2 molecules can easily penetrate in the amorphous regions but are less soluble in the crystalline domains due to the packed chain configuration [Salerno et al., 2014]. Favorable interactions between carbon dioxide and polymers containing carbonyl groups, such as PCL, have been shown in various papers [Reverchon et al., 2000; Shieh and Yang, 2005]. Lower $scCO_2$ sorption values characterize PEO, although it shares with PCL comparable thermal properties and crystalline fraction amounts. In spite of its relatively low solubility in both polymers, $scCO_2$ exhibits a pronounced plasticizing effect, especially at the operating temperature of 50 °C. Indeed, high precipitation temperature results in a fast expansion of the liquid solution, and therefore an early precipitation of crystal nuclei, which have more time to grow and possibly to coalesce, eventually giving rise to continuous structures [Bakhbakhi et al., 2013]. As far as PCL is concerned, increasing the temperature from 40 to 50 °C marks the transition from generally

discrete to continuous flat structures in both the EL and EA systems. Another peculiarity of the PCL samples processed at 50 °C is the bimodal spherulite size distribution. The sorption of $scCO_2$ in PCL at 50 °C brings about a substantial melting of the precipitated crystals. The small spherulites are believed to derive from both $scCO_2$-induced crystallization of the amorphous phase and recrystallization of the melted domains, while the large crystals probably ensue from domains not completely melted during the process. Conversely, at 40 °C the less pronounced plasticizing power of CO_2, coupled with the smaller dimensions of the precipitates, is not sufficient to promote the coalescence of the domains into continuous structures, or alternatively the effects of $scCO_2$ are less evident. Regarding PEO, a slight enlargement of the spherulites in the samples precipitated from EL solutions is detected by increasing the temperature (Figure 7.6). On the other hand, the particles resulting from the treatments at 40 °C in EA merge at 50 °C, that is well below the PEO melting point of ~ 65 °C, giving rise to continuous films (Figure 7.8). Hence, $scCO_2$ is able to depress the melting point of both PCL and PEO below the operating temperature of 50 °C, thereby promoting partial melting and recrystallization phenomena. However, the rather limited sorption of $scCO_2$ in the two polymers studied in this work is not sufficient to induce noticeable plasticization at 40 °C.

As a final point, the influence of the operating pressure is discussed. The main effect inferred from the $scCO_2$-assisted tests is an increase of the size of the PEO microparticles obtained from EA solutions when passing from 10 (Figure 7.7a-c) to 20 MPa (Figure 7.7d-f). Such a result is not unprecedented, since moderate enlargements of micronic and submicronic biocompatible polymer particles by increasing pressure have been highlighted by Randolph and co-workers as well as by Reverchon and co-workers [Randolph et al., 1993; Reverchon et al., 2000]. According to them, conducting the polymer precipitation process in pressure conditions close to the critical point of CO_2 results in rapid mass transfer; accordingly, high degrees of supersaturation are reached, together with high nucleation rates and short times for the nuclei to grow. Negligible morphological changes are found in the PCL samples, probably because of the too low operating temperature. The implications related to the pressurization and depressurization times are expected to be minor, since both steps have been conducted slowly in order to minimize the pressure and temperature change rates and to avoid samples foaming.

To sum up, in comparison with conventional solvent casting, through which a through which a limited number of polymer structures can be achieved, the use of

scCO2 as an antisolvent to assist polymer precipitation offers the opportunity to tune the solid-state morphology of the material. The latter may assume the form of continuous films, discrete precipitates or porous microparticles, possibly passing from one to other by adjusting the temperature, pressure and solution composition. Depending on the operating conditions, $scCO_2$ is able to plasticize the polymer, promoting partial or complete recrystallization phenomena and eventually giving rise to bimodal spherulite size distributions. Being the first focused report on the $scCO_2$ antiolvent precipitation from the selected polymer/solvent systems, the study presented in this chapter represent a promising starting point for the implementation of a continuous and sustainable $scCO_2$-assisted process for biodegradable mono- and multiphase polymer systems.

8

Concluding remarks

The principal aim of the present thesis is the investigation, from both a fundamental and technological point of view, of the possibility of using nanoscale fillers as clever means to manipulate the morphology and the performances of multiphase polymer systems. The study is focused on two categories of immiscible polymer blends: (*i*) melt-compounded systems and (*ii*) solvent-cast systems, characterized in terms of bulk and surface morphology and properties, respectively.

The first part of the research consists in a fundamental study conducted to shed light on the physical mechanisms that govern the melt-state morphology evolutions of immiscible polymer blends in the presence of nanofillers. Specifically, the assembly of plate-like nanoparticles in a biphasic polymer system has been investigated through the combination of microscopy techniques, rheological measurements and selective extraction experiments. The comparison with a monophasic reference system has allowed to elucidate the bulk morphological implications deriving from the presence of polymer/polymer interfaces where the filler is inclined to locate. Thermodynamic equilibrium considerations well predict the preferential localization of the particles at the polymer/polymer interface in a blend with drop-matrix morphology. Such interfacial anchoring hinders the mobility of the filler and inhibits flocculation phenomena; as a consequence, the viscoelastic behavior of the blends at low filler content is not affected by the particles. Once the available polymer/polymer interface has been saturated, any further addition of particles causes an increase of elasticity during time, which reflects the enabled rearrangement of the platelets in the melt and their eventual assembly in a space-spanning network. The marked elastic connotation of such a superstructure exceeds the interfacial contribution of the drops, and the viscoelasticity of the filled blend can hence be described irrespective of the presence of the dispersed polymer phase. The filler percolation threshold in the biphasic matrix is found to be slightly higher than in the monophasic one and to coincide with the filler content above which the elasticity of the system starts to increase over time, confirming the absence of flocculation of the particles trapped

at the drop surface. The filler network in the blend exhibits a peculiar structure, embedding and connecting single and clustered particle-coated drops. Such clustering phenomena of polymer domains are also claimed to play a role in altering the onset of co-continuity of the blend, as emerged from the characterization of systems with different polymer compositions. The highlight of the activity described so far is the elucidation of the mutual interactions among the different phases of nanoparticle-containing polymer blends. On one hand, the fluids dictate the space arrangement of the filler, eventually frustrating its peculiar mobility in molten polymers in the case of preferential interfacial localization. Even so, the particles are able to drive the morphology of the blend without the need of complete saturation of the interface.

The second part of the research is focused on the development of the surface morphology of polymer films during casting from a polymeric solution. Fundamental investigations have been carried out aiming to assess the effect of the interactions among the different constituents (casting substrate, solvent, polymers and filler) on the formation of the films and their surface features. The attention has been initially directed towards monophasic polymer films, and then on multiphase systems. The selected materials are biodegradable, semi-crystalline polymers and benign solvents. The characterization of homopolymer-based systems has pointed out that the formation of polymer films by drop casting onto a glass substrate strongly depends on the competition between drop spreading and solvent evaporation and, ultimately, on solvent choice and polymer concentration. Specifically, large spreading areas and low film thicknesses ensue from a high chemical affinity between solvent and substrate and/or a low solvent evaporation rate. For semi-crystalline polymers, increasing polymer concentration or using a rapidly evaporating solvent leads to a pronounced crystal nucleation and the consequent formation of small spherulites. Both the inner structure and the space arrangement of the crystalline domains contribute in determining the textural features of the films and the related properties, such as surface hydrophilicity. When two or more polymers are present in the pristine solution, their incompatibility results in a multi-step phase separation process which is driven by both solvent evaporation and solubility of each of the polymers in the common solvent, leading to the formation of final segregated morphologies with different characteristic length scales. Similarly to bulk multiphase systems, the morphology of polymer blend films can be tuned by adjusting the blend composition and/or adding small amounts of nanoparticles. The latter, indeed, are able to affect the phase separation process, and their dynamics are in turn influenced by the changes

in polarity and viscosity of the suspending medium during solvent evaporation. As a result of this interplay, the final film structure may deviate from that predicted by thermodynamic equilibrium considerations. Depending on the affinity between the particles and the fluid phases, different degrees of dispersion and filler structures (large aggregates, isolated micron-sized flocs and space-filling networks) can be attained, with notable morphological implications. A high particle/solvent affinity results in a uniform filler distribution and the promotion of fine surface morphologies. On the other hand, the prevalence of inter-particle attractions leads to a marked tendency of the filler to agglomerate in the suspending medium and, coarsen the microstructure of the resulting film. Ultimately, the surface texture of the polymer blends is strictly related to their segregated morphology, being essentially dictated by the topography of the continuous phase.

Alongside the activity on solvent-cast systems, the final part of the research has been devoted to explore the potential of using supercritical CO_2 as a "green" antisolvent for polymer precipitation. This technique allows to tune the solid-state morphology of both mono- and multiphase materials, which assume different forms (continuous films, discrete precipitates, porous microparticles), possibly passing from one to other by adjusting the temperature, pressure and solution composition. Under certain conditions, supercritical CO_2 plasticizes the polymers, promoting partial or complete recrystallization phenomena and eventually giving rise to multimodal crystallite size distributions.

In conclusion, the results reported in the present work provide experimental evidences that a clever manipulation of the morphology of immiscible polymer blends through the use of nanoparticles (or other processing aids, such as supercritical fluids), together with a judicious selection of the blend constituents and the processing techniques, represents a viable and general strategy to obtain "genuine polymer nanocomposites" with tailored structure and properties. Among the promising applications of this approach, the production of heat-resistant formulations based on recycled polymers and of biodegradable and biocompatible films with prescribed topography and texture have been successfully explored.

Appendices

A.1 WAXD analyses on clay-filled PS, PMMA and their blend

With reference to the activity described in Chapter 3, Figure A.1 shows the WAXD spectra for the neat clay filler and representative as-extruded polymer nanocomposites: a PS/clay, a PMMA/clay, and a PS/PMMA/clay sample (at 15 wt% of PMMA), all having a filler content $\Phi \approx 0.93\%$. The interlayer spacing between the silicate layers, d_{001}, is estimated by applying the Bragg's condition to the low-angle peak ($2° < 2\theta < 4°$) of the scattering intensity, which corresponds to the {001} basal reflection of the montmorillonite aluminosilicate.

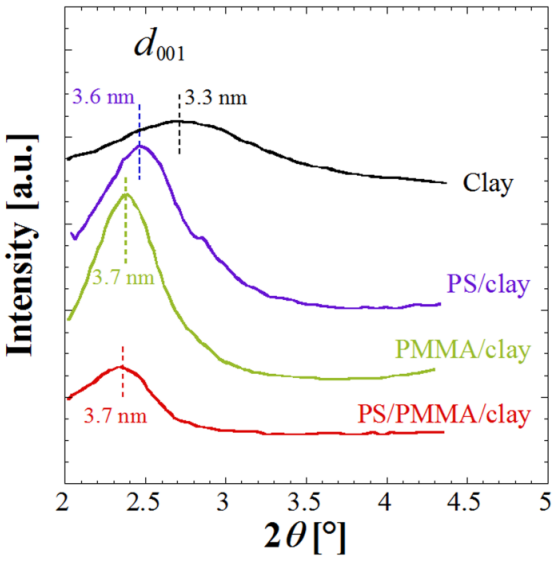

Figure A.1 – WAXD patterns for neat organoclay, PS/clay, PMMA/clay and PS/PMMA/clay samples at $\Phi \approx 0.93\%$. The interlayer spacing computed from the Bragg's condition are reported as well. Adapted by [Filippone et al., 2014] with permission from the Royal Society of Chemistry.

Although PMMA exhibits slightly better interactions with the clay, the diffraction peaks of the three polymer nanocomposites are too wide and too close to each other to draw unambiguous conclusions about which polymer preferentially intercalates the filler. The most reasonable deductions are the existence of both PS- and PMMA-intercalated tactoids, as well as of clay stacks located at the PS/PMMA interface and simultaneously intercalated by both polymers. These conclusions exactly reflect the criterion adopted to select the materials: since the rationale is to promote the localization of the filler at the polymer/polymer interface, clay particles that do not exhibit preferential interactions with a specific blend component have been chosen.

A.2 Predictions of the Palierne model for the unfilled PS/PMMA blend

The frequency-dependent values of G' and G'' measured for the unfilled PS/PMMA blend have been compared with the expectations of the Palierne model, which predicts the linear viscoelastic moduli of a blend with drop-matrix morphology once the interfacial tension (σ) and the radius of the dispersed phase (R) are known [Palierne, 1990].

A value σ = 1.16 mN m^{-1} has been taken from the literature for the pair PS-PMMA [Carriere et al., 2000]. The size of the PMMA drops has been estimated by analyzing SEM micrographs of the PS/PMMA blend, according to the procedure described below. SEM analyses have been performed on the cryo-fractured surface of a sample previously etched with formic acid to selectively remove the PMMA phase. About 10^3 holes, corresponding to the removed PMMA drops, have been manually selected from several micrographs (see Figure A.2).

The so-obtained binary images have then been analyzed by means of the ImageJ® software. The radius of the i-th inclusion has been evaluated as

$$R_i = \sqrt{\frac{\bar{A}_i}{\pi}} \tag{A.1}$$

where is the measured inclusion area amplified by a factor $4/\pi$ in order to account for the systematic underestimation of the dimensions of an object from its print on a flat surface. The number-average and volume-average drop radius, R_n, has been then estimated as

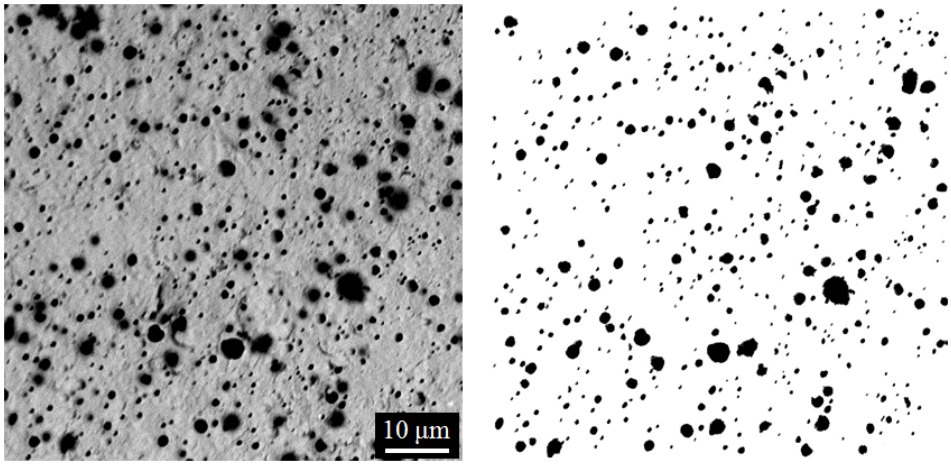

Figure A.2 – Original SEM micrograph of a PS/PMMA blend (left) and binary image obtained by manually detecting the PMMA inclusions (right). Adapted from [Filippone et al., 2014] with permission from the Royal Society of Chemistry.

$$R_n = \sum_i \left(\frac{n_i}{n_{tot}} \right) R_i \tag{A.2}$$

while the volume-average drop radius has been estimated as

$$R_v = \sum_i \left(\frac{V_i}{V_{tot}} \right) R_i \tag{A.3}$$

where n_i/n_{tot} and V_i/V_{tot} are the numerical and volumetric fractions of drops with radius R_i, respectively. The image analysis leads to $R_v = 0.895$ µm and $R_v/R_n = 1.94$. Being the polydispersity lower than 2, the volume-average radius can be used as representative size of the PMMA drops. Figure A.3 shows the comparison between predicted and measured moduli of the unfilled blend: the good agreement between the values supports the reliability of the viscoelastic measurements performed.

A.3 Pre-processing of TEM images and fractal analysis

Before performing the fractal analysis, the TEM micrographs have been preprocessed to isolate the dark pixels associated with the clay particles. First, the images have been adjusted and equalized to their basic tones. Then, the position of

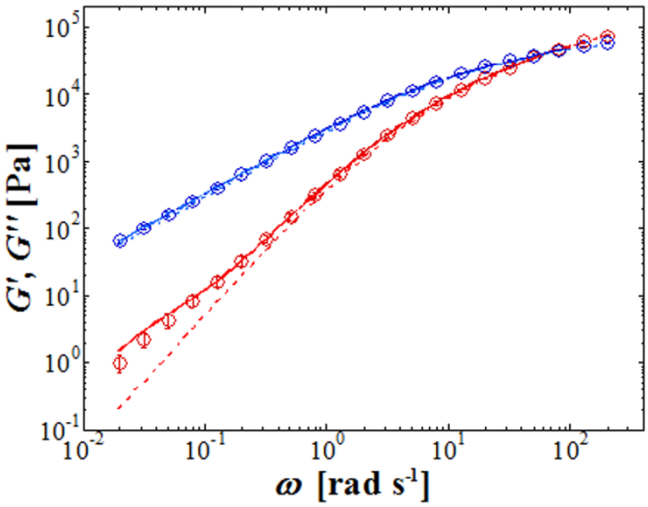

Figure A.3 – Comparison between the elastic (red) and viscous moduli (blue) measured (circles) and predicted by the Palierne model (solid lines). The error bars represent standard deviations over three independent measurements. The dashed lines are the moduli of the neat PS. Adapted from [Filippone et al., 2014] with permission from the Royal Society of Chemistry.

the dark pixels has been obtained through the indices of the low tone image. The preprocessing step are summarized by the montage reported as Figure A.4.

The following step has been the identification of the flocs. It has been assumed that two clay tactoids belong to the same floc if their minimum distance is smaller than 100 nm, i.e. about one tenth of the average lateral dimension of the tactoids. An example of outcome of the floc identification step is shown in Figure A.5.

Each identified floc has been isolated, extracted from the image and subjected to fractal analysis. The 2D box counting fractal dimension D_f has been estimated through the counting boxes algorithm. The algorithm divides the image into equal-sized square blocks, and then it tests each block to check if it meets some user-selected criterion. In the analysis here described, the presence in the box of a fraction of black pixels higher than 25% is considered a positive correspondence. This procedure is repeated for all possible image tessellation, collecting the total number of positive correspondences, generally named as counts.

The result of the box counting algorithm is shown in Figure A.6. The 2D box counting fractal dimension corresponds to the linear regression of the log-log plot reporting the total counts (N_{BOX}) versus box length (L_{BOX}).

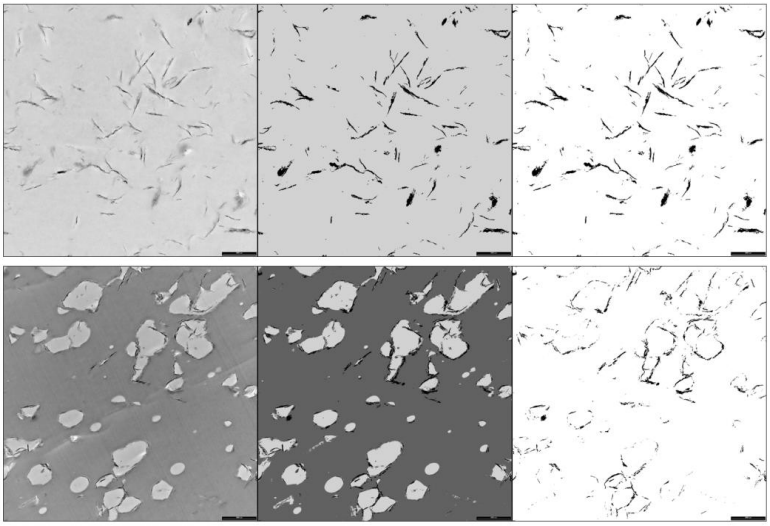

Figure A.4 – Example of the preprocessing step for two representative samples at Φ = 1.32% (top row: PS/PMMA/clay; bottom row PS/clay). The original micrographs (left) have been adjusted and discretized to the most frequent tones according to the image histogram (center). The resulting channel of dark pixels is shown on the right. Adapted from [Filippone et al., 2014] with permission from the Royal Society of Chemistry.

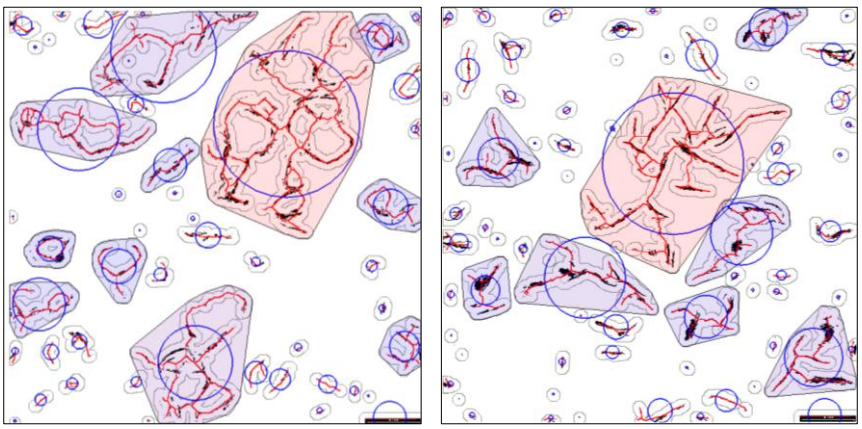

Figure A.5 – Identification of the flocs and image segmentation. The shaded areas display the convex circumscribing the floc, which also represents the mask used to extract the objects from the image. Note that small objects have not been considered in the fractal analyses. Adapted from [Filippone et al., 2014] with permission from the Royal Society of Chemistry.

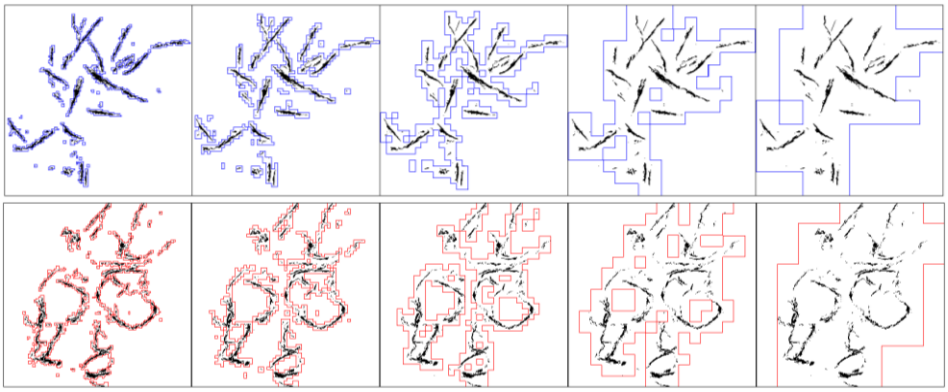

Figure A.6 – Counting box snapshots for PS/clay (top row) and PS/PMMA/clay systems (bottom row) at several box lengths (from left to right: 8, 16, 32, 64, and 128 pixels). The size of the region of interest is 1024 × 1024 pixels wide. Only the boxes containing a fraction of dark pixels greater than the overall content of the image are shown. Adapted from [Filippone et al., 2014] with permission from the Royal Society of Chemistry.

A.4 Optical micrographs analysis of solvent-cast films

The optical micrographs of the solvent-cast PCL and PCL/PEO samples have been analyzed in order to estimate the average size and the size distribution of spherulites and phase domains. A manual detection of the entities has been performed in order to minimize the errors which may ensue from an automatic recognition procedure.

As an example, an original optical micrograph is compared with the image processed after manual selection of the spherulites in Figure A.7. More than 100 crystals per sample, taken from different micrographs made over different regions of independent specimens, have been selected and the binary images have been analyzed using the ImageJ® software. The crystal size measurements have been performed approximating the PCL spherulites as round objects and calculating their diameter from the area values resulted from image analysis.

In Figure A.8, original POM micrographs of a PCL/PEO blend film at weight ratio 70/30 sample are compared with the images processed after manual selection of the domains. The low-magnification images have been analyzed to determine the fraction areas occupied by the PCL- and PEO-rich phases and the size (diameter) of the dispersed domains. The high-magnification images have instead

been used to estimate the fraction area of the small-scale PCL entities contained in the PEO-rich regions.

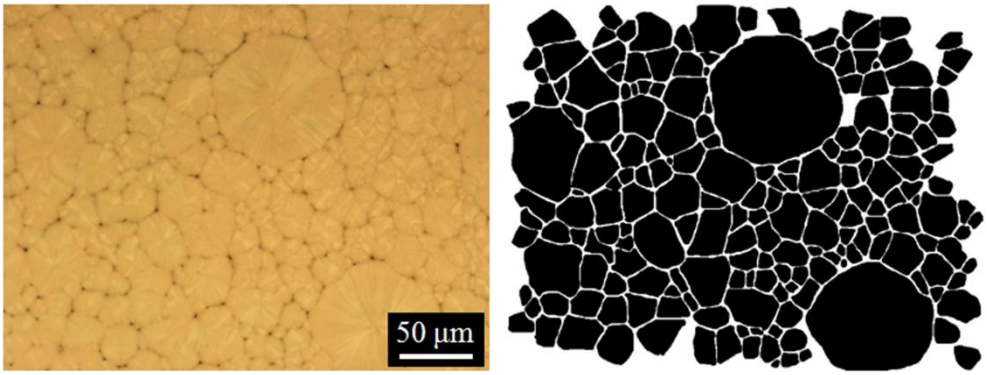

Figure A.7 - Original micrograph of a PCL film and corresponding binary image obtained after manual selection of the spherulites.

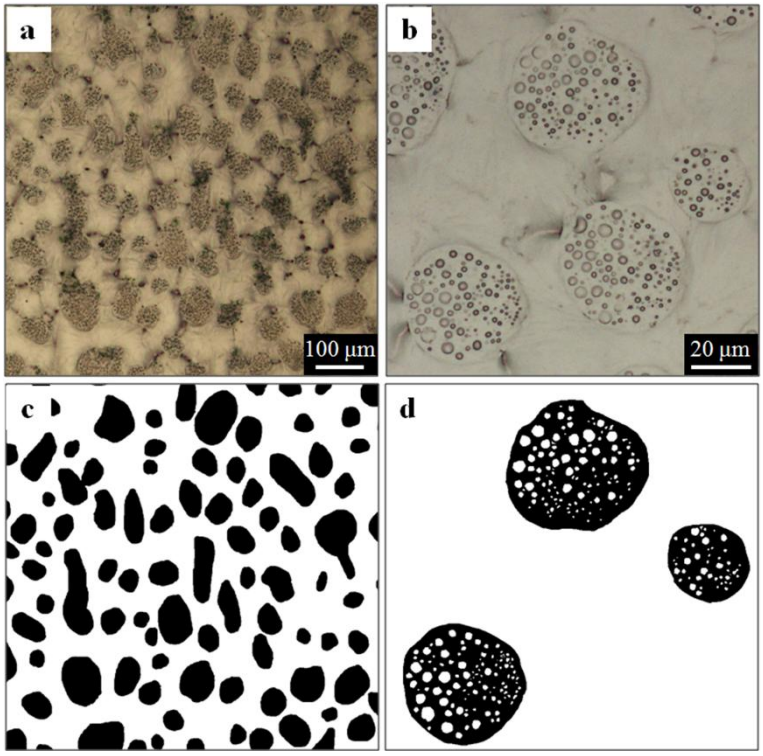

Figure A.8 - Original micrographs of a PCL/PEO film at weight ratio 70/30 (a, b) and corresponding binary images (c, d) obtained after manual selection of the phase domains.

A.5 Polarized optical micrographs of antisolvent-precipitated samples

Figure A.9 and A.10 show polarized optical micrographs of PCL samples obtained through supercritical antisolvent precipitation. The images exactly correspond to those of Figure 7.3 and 7.4, acquired in direct mode.

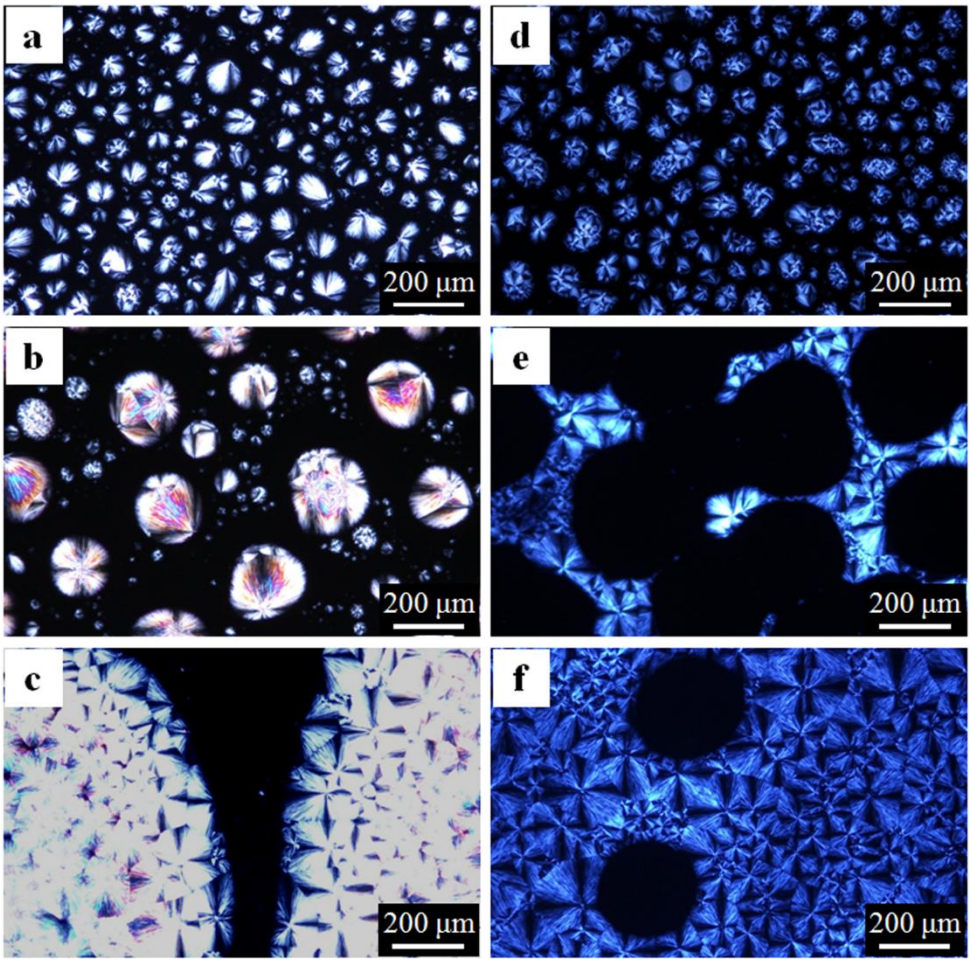

Figure A.9 – Polarized optical micrographs (cf. Figure 7.3) of PCL samples prepared from EL solutions by $scCO_2$ antisolvent precipitation at (a-c) 40 °C and 10 MPa and (d-f) 40 °C and 20 MPa (polymer concentrations: 2, 5, 10 wt/vol%).

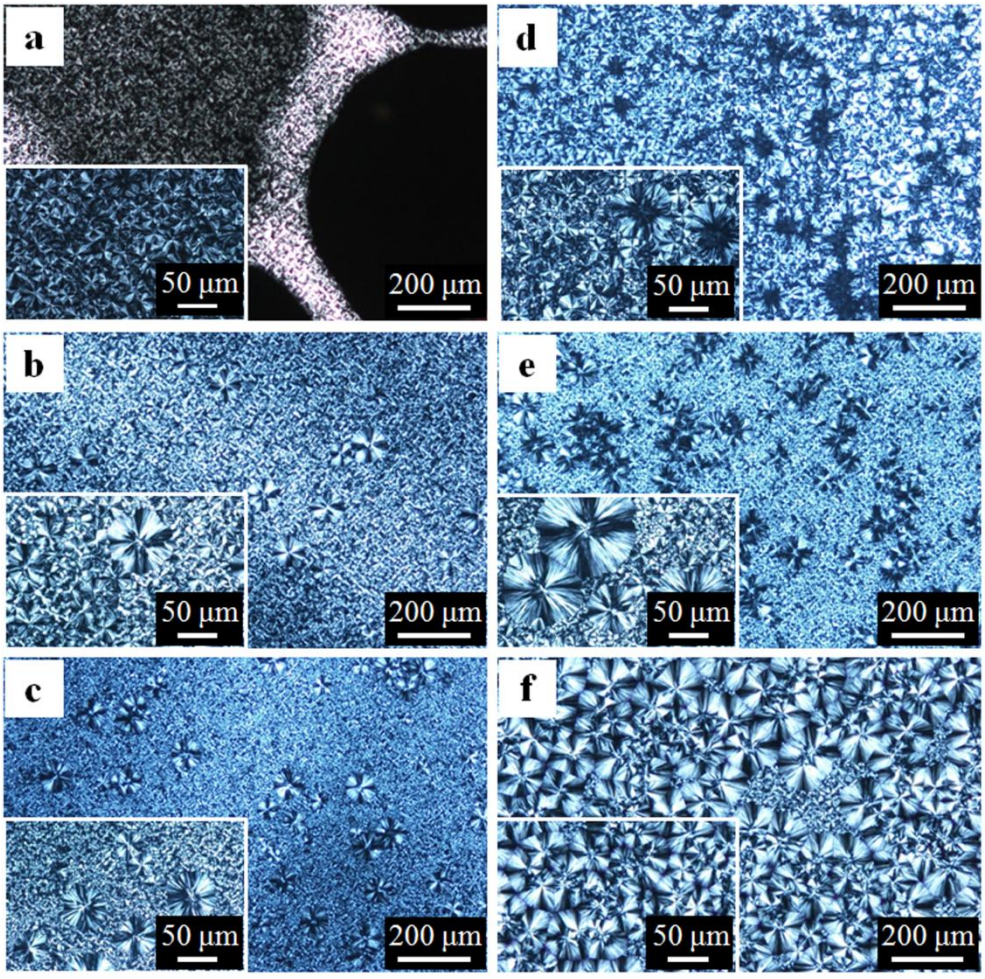

Figure A.10 – Polarize optical micrographs (cf. Figure 7.4) of PCL samples prepared at 50 °C and 10 MPa from (a-c) EL solutions and (d-f) EA solutions (polymer concentrations: 2, 5, 10 wt/vol%). The images acquired in transmission mode are reported in Appendix A.5.

References

Ahn DU, Wang Z, Campbell IP, Stoykovich MP, Ding Y, "Morphological evolution of thin PS/PMMA films: Effects of surface energy and blend composition", Polymer 53, 4187–4194 (2012).

Ajji A, Utracki LA, "Interphase and compatibilization of polymer blends", Polym. Eng. Sci. 36, 1574–1585 (1996).

Al-Saleh MH, Al-Anid HK, Hussain YA, "Electrical double percolation and carbon nanotubes distribution in solution processed immiscible polymer blend", Synthetic Met. 175, 75–80 (2013).

Aparicio S and Alcalde R, "The green solvent ethyl lactate: an experimental and theoretical characterization", Green Chem. 11, 65–78 (2009).

Araki T and Tanaka H, "Wetting-induced depletion interaction between particles in a phase-separating liquid mixture", Phys. Rev. E 73, 061506 (2006).

Arias AC, Corcoran N, Banach M, Friend RH, MacKenzie JD, Huck WTS, "Vertically segregated polymer-blend photovoltaic thin-film structures through surface-mediated solution processing", Appl. Phys. Lett. 80, 1695–1697 (2002).

Aronov D, Rosen R, Ron EZ, Rosenman G, "Tunable hydroxyapatite wettability: Effect on adhesion of biological molecules", Process Biochem. 41, 2367–2372 (2006).

Aveyard R, Binks BP, Clint JH, "Emulsions stabilised solely by colloidal particles", Adv. Colloid. Interf. Sci. 100-102, 503–546 (2003).

Bakhbakhi Y, Asif M, Chafidz A, Ajbar A, "Formation of biodegradable polymeric fine particles by supercritical antisolvent precipitation process, Polym. Eng. Sci. 53, 564–570 (2013).

Barton AFM, "Handbook of solubility parameters and other cohesion parameters", 2nd edition, CRC Press LLC, Boca Raton, 1991.

Bentley BJ and Leal LG, “An experimental investigation of drop deformation and breakup in steady, two-dimensional linear flows”, J. Fluid Mech. 167, 241–283 (1986).

Bertola V, “Dynamic wetting of dilute polymer solutions: the case of impacting droplets”, Adv. Colloid Interf. Sci. 193-194, 1–11 (2013).

Binks BP, “Particles as surfactants – similarities and differences”, Curr. Opin. Colloid. Interf. Sci. 7, 21–41 (2002).

Bitinis N, Verdejo R, Maya EM, Espuche E, Cassagnau P, Lopez-Manchado MA, “Physicochemical properties of organoclay filled polylactic acid/natural rubber blend bionanocomposites”, Compos. Sci. Technol. 72, 305–313 (2012).

Bockstaller MR, Mickiewicz RA, Thomas, EL, “Block copolymer nanocomposites: perspectives for tailored functional materials” Adv. Mater. 17, 1331–1349 (2005).

Böltau M, Walheim S, Mlynek J, Krausch G, Steiner U, “Surface-induced structure formation of polymer blends on patterned substrates”, Nature 391, 877–879 (1998).

Borah JS, Karak N, Chaki TK, “Effect of organoclay platelets on morphology and properties of LLDPE/EMA blends”, Mater. Sci. Eng. A 528, 2820–2830 (2011).

Bordes C, Fréville V, Ruffin E, Marote P, Gauvrit JY, Briançon S, Lantéri P, “Determination of poly(ε-caprolactone) solubility parameters: Application to solvent substitution in a microencapsulation process”; Int. J. Pharm. 383, 236–243 (2010).

Cai X, Li B, Pan Y, Wu G, “Morphology evolution of immiscible polymer blends as directed by nanoparticle self-agglomeration”, Polymer 53, 259–266 (2012).

Cao J, Zhu B, Ji G, Xu Y, Preparation and characterization of PVDF–HFP microporous flat membranes by supercritical CO_2 induced phase separation, J. Membrane Sci. 266, 102–109 (2005).

Carriere CJ, Biresaw G, Sammler RL, “Temperature dependence of the interfacial tension of PS/PMMA, PS/PE and PMMA/PE blends”, Rheol. Acta 29, 476–482 (2000).

Causa A, Filippone G, Acierno D, Domingo C, Salerno A, “Surface morphology, crystallinity, and hydrophilicity of poly(ε-caprolactone) films prepared via casting of ethyl lactate and ethyl acetate solutions”, Macromol. Chem. Phys. 216, 49–58 (2015).

Champeau M, Thomassin JM, Jérôme C, Tassaing T, “In situ FTIR micro-spectroscopy to investigate polymeric fibers under supercritical carbon dioxide: CO_2 sorption and swelling measurements”, J. Supercrit. Fluid. 90, 44–52 (2014).

Chappell J, Lidzey DG, Jukes PC, Higgins AM, Thompson RL, O’Connor S, Grizzi I, Fletcher R, O’Brien J, Geoghegan M, Jones RAL, “Correlating structure with fluorescence emission in phase-separated conjugated-polymer blends”, Nature Mater. 2, 616–621 (2003).

Cheng HL, Ph.D. Thesis, University of Pittsburgh (2009).

Cheng HL and Velankar SS, “Interfacial jamming of particle-laden interfaces studied in a spinning drop tensiometer”, Langmuir 25, 4412–4420 (2009).

Chesters AK, “The modelling of coalescence processes in fluid-liquid dispersions: a review of current understanding”, Chem. Eng. Res. Des. 69, 259–270 (1991).

Chiu F, Yen H and Lee C, “Characterization of PP/HDPE blend-based nanocomposites using different maleated polyolefins as compatibilizers”, Polym. Test. 29, 397–406 (2010).

Chung HJ, Taubert A, Deshmukh RD, Composto RJ, “Mobile nanoparticles and their effect on phase separation dynamics in thin-film polymer blends”, Europhys. Lett. 68, 219–225 (2004).

Chung HJ, Ohno K, Fukuda T, Composto RJ, “Self-regulated structures in nanocomposites by directed nanoparticle assembly”, Nano Lett. 5, 1878–1882 (2005).

Clegg PS, “Fluid-bicontinuous gels stabilized by interfacial colloids: low and high molecular weight fluids”, J. Phys. Condens. Matter 20, 113101 (2008).

Cole DH, Shull KR, Baldo P, Rehn L, “Dynamic properties of a model polymer/metal nanocomposite: gold particles in poly(tert-butyl acrylate)”, Macromolecules 32, 771–779 (1999).

Corcoran N, Arias AC, Kim JS, MacKenzie JD, Friend RH, "Increased efficiency in vertically segregated thin-film conjugated polymer blends for light-emitting diodes", Appl. Phys. Lett. 82, 299–301 (2003).

Dasari A, Yu ZZ, Mai YW, "Effect of blending sequence on microstructure of ternary nanocomposites", Polymer 46, 5986–5991 (2005).

Dean JA, "Lange's Handbook of Chemistry", 15th edition, McGraw-Hill, New York (1998).

Deegan RD, Bakajin O, Dupont TF, Huber G, Nagel SR, Witten TA, "Capillary flow as the cause of ring stains from dried liquid drops", Nature 1997, 389, 827–829.

Dekeyser CM, Biltresse S, Marchand-Brynaert J, Rouxhet PG, Dupont-Gillain CC, "Submicrometer-scale heterogeneous surfaces by PS-PMMA demixing", Polymer 45, 2211–2219 (2004).

Dintcheva NTz, Filippone G, La Mantia FP, Acierno D, "Photo-oxidation behaviour of polyethylene/polyamide 6 blends filled with organomodified clay: Improvement of the photo-resistance through morphology modification", Polym. Degrad. Stabil. 95, 527–535 (2010).

Dixon DJ and Johnston KP, "Formation of microporous polymer fibers and oriented fibrils by precipitation with a compressed fluid antisolvent", J. Appl. Polym. Sci. 50, 1929–1942 (1993).

Durmus A, Kasgoz A, Macosko CW, "Linear low density polyethylene (LLDPE)/clay nanocomposites. Part I: Structural characterization and quantifying clay dispersion by melt rheology", Polymer 48, 4492–4502 (2007).

Elias L, Fenouillot F, Majeste JC, Cassagnau P, "Morphology and rheology of immiscible polymer blends filled with silica nanoparticles", Polymer 48, 6029–6040 (2007).

Elias L, Fenouillot F, Majeste JC, Martin G, Cassagnau P, "Migration of nanosilica particles in polymer blends", J. Polym. Sci. Part B: Polym. Phys. 46, 1976–1983 (2008).

Elkovitch MD, Tomasko DL, Lee LJ, "Supercritical carbon dioxide assisted blending of polystyrene and poly (methyl methyacrylate)", Polym. Eng. Sci. 39, 2075–2084 (1999).

Elvassore N, Baggio M, Pallado P, Bertucco A, “Production of different morphologies of biocompatible polymeric materials by supercritical CO_2 antisolvent techniques”, Biotechnol. Bioeng. 73, 449–457 (2001).

Entezam M, Khonakdar HA, Yousefi AA, “On the flame resistance behavior of PP/PET blends in the presence of nanoclay and a halogen-free flame retardant”, Macromol. Mater. Eng. 298, 1074–1084 (2013).

Fang C, Nie L, Liu S, Yu R, An N, Li S, “Characterization of polypropylene-polyethylene blends made of waste materials with compatibilizer and nano-filler”, Composites: Part B 55, 498–505 (2013).

Fang Z, Harrats C, Moussaif N, Groeninckx G, “Location of a nanoclay at the interface in an immiscible poly(e-caprolactone)/poly(ethylene oxide) blend and its effect on the compatibility of the components”, J. Appl. Polym. Sci. 106, 3125–3135 (2007).

Fanovich MA and Jaeger P, “Sorption and diffusion of compressed carbon dioxide in polycaprolactone for the development of porous scaffolds”, Mat. Sci. Eng. C 32, 961–968 (2012).

Feng J, Chan QCM, “Carbon black-filled immiscible blends of poly(viny1idene fluoride) and high density polyethylene: electrical properties and morphology”, Polym. Eng. Sci. 38, 1649–1657 (1998).

Feng J, Chan CM, Li JX, “A method to control the dispersion of carbon black in an immiscible polymer blend”, Polym. Eng. Sci. 43, 1058–1063 (2003).

Feng M, Gong F, Zhao C, Chen G, Zhang S, Yang M, “Effect of clay on the morphology of blends of poly(propylene) and polyamide 6/clay nanocomposites”, Polym. Int. 53, 1529–37 (2004).

Fenouillot F, Cassagnau P, Majeste JC, “Uneven distribution of nanoparticles in immiscible fluids: Morphology development in polymer blends,” Polymer 50, 1333–1350 (2009).

Ferreiro V, Douglas JF, Warren J, Karim A, “Growth pulsations in symmetric dendritic crystallization in thin polymer blend films”, Phys. Rev. E 65, 051606 (2002a).

Ferreiro V, Douglas JF, Warren JA, Karim A, “Nonequilibrium pattern formation in the crystallization of polymer blend films”, Phys. Rev. E 65, 042802 (2002).

Filippone G., Dintcheva NTz, Acierno D, La Mantia FP, “The role of organoclay in promoting co-continuous morphologies in high density poly(ethylene)/poly(amide) 6 blends”, Polymer 49, 1312–1322 (2008).

Filippone G., Dintcheva NTz, La Mantia FP, Acierno D, “Using organoclay to promote morphology refinement and co-continuity in high-density polyethylene/polyamide 6 blends e Effect of filler content and polymer matrix composition”, Polymer 51, 3956–3965 (2010a).

Filippone G., Dintcheva NTz, La Mantia FP, Acierno D, “Selective localization of organoclay and effects on the morphology and mechanical properties of LDPE/PA11 blends with distributed and co-continuous morphology”, J. Polym. Sci Pol. Phys. 48, 600–609 (2010b).

Filippone G, Romeo G, Acierno D, “Viscoelasticity and structure of polystyrene/fumed silica nanocomposites: filler network and hydrodynamic contributions”, Langmuir 26, 2714–2720 (2010c).

Filippone G and Acierno D, “Altering the onset of cocontinuity in nanocomposite immiscible blends by acting on the melt-compounding procedure”, J. Appl. Polym. Sci. 122, 3712–3719 (2011a).

Filippone G, Romeo G, Acierno D, “Role of interface rheology in altering the onset of co-continuity in nanoparticle-filled polymer blends”, Macromol. Mater. Eng. 296, 658–665 (2011b).

Filippone G and Acierno D, “clustering of coated droplets in clay-filled polymer blends”, Macromol. Mater. Eng. 2012, 923–928 (2012).

Filippone G, Salzano de Luna M, Acierno D, Russo P, “Elasticity and structure of weak graphite nanoplatelet (GNP) networks in polymer matrices through viscoelastic analyses”, Polymer 53, 2699–2704 (2012).

Filippone G and Salzano de Luna M, “A unifying approach for the linear viscoelasticity of polymer nanocomposites”, Macromolecules 45, 8853–8860 (2012).

Filippone G, Causa A, Salzano de Luna M, Sanguigno L, Acierno D, “Assembly of plate-like nanoparticles in immiscible polymer blends – Effect of the presence of a preferred liquid–liquid interface”, Soft Matter 10, 3183–3191 (2014).

Fukai J, Ishizuka H, Sakai Y, Kaneda M, Morita M, Takahara A, “Effects of droplet size and solute concentration on drying process of polymer solution

droplets deposited on homogeneous surfaces", Int. J. Heat Mass Tran. 49, 3561–3567 (2006).

Galloway JA and Macosko CW, "Comparison of methods for the detection of cocontinuity in poly(ethylene oxide)/polystyrene blends", Polym. Eng. Sci. 44, 714–727 (2004).

Galloway JA, Koester KJ, Paasch BJ, Macosko CW, "Effect of sample size on solvent extraction for detecting cocontinuity in polymer blends", Polymer 45, 423–428 (2004).

Gam S, Corlu A, Chung HJ, Ohno K, Hore MJA, Composto RJ, "A jamming morphology map of polymer blend nanocomposite films", Soft Matter 7, 7262–7268 (2011).

Gao JL, Liu YH, Li DM, "Preparation and properties of recycled polypropylene/carbon nanotube composites", Adv. Mater. Res. 279, 106–110 (2011).

García-González CA, Fraile J, López-Periago A and Domingo C, "Preparation of silane-coated TiO_2 nanoparticles in supercritical CO_2", J. Colloid Interf. Sci. 338, 491–499 (2009a).

García-González CA, Vega-González A, López-Periago AM, Subra-Paternault P, Domingo C, "Composite fibrous biomaterials for tissue engineering obtained using a supercritical CO_2 antisolvent process", Acta Biomater. 5, 1094–1103 (2009b).

Geoghegan M and Krausch G, "Wetting at polymer surfaces and interfaces", Prog. Polym. Sci. 28, 261–302 (2003).

Ghaderi R, Artursson P, Carlfors J, "Preparation of biodegradable microparticles using solution-enhanced dispersion by supercritical fluids (SEDS)", Pharm. Res. 16, 676–681 (1999).

Gleissle W and Hochstein B, "Validity of the Cox-Merz rule for concentrated suspensions", J. Rheol. 47, 897–910 (2003).

Göldel A, Kasaliwal G, Potschke P, "Selective localization and migration of multiwalled carbon nanotubes in blends of polycarbonate and poly(styrene-acrylonitrile)", Macromol. Rapid Commun. 30, 423–429 (2009).

Göldel A, Kasaliwal G, Potschke P, Heinrich G, “The kinetics of CNT transfer between immiscible blend phases during melt mixing”, Polymer 53, 411–421 (2012).

Gong Y and Leal LG, “Role of symmetric grafting copolymer on suppression of drop coalescence”, J. Rheol. 56, 397–433 (2012).

Grace HP, “Dispersion phenomena in high viscosity immiscible fluid systems and application of static mixers as dispersion devices in such systems”, Chem. Eng. Commun. 14, 225–277 (1982).

Graebling D and Muller R, “Rheological behaviour of polydimethylsiloxane/ polyoxyethylene blends in the melt – Experimental results for PDMS/POE-DO, PS/PMMA and PS/PEMA blends”, Eur. Polym. J. 30, 301–308 (1990).

Granström M, Petritsch K, Arias AC, Lux A, Andersson MR, Friend RH, “Laminated fabrication of polymeric photovoltaic diodes”, Nature 395, 257–260 (1998).

Greenman K, Bauer A, Kool D, Liu J, Li B, “Morphological regimes of poly(ε-caprolactone)/octaisobutyl polyhedral oligosilsesquioxane composite films in relation to film composition and thickness”, Colloid Polym. Sci. 292, 2227–2240 (2014).

Gubbels F, Blacher E, Vanlathem R, Jerome R, Deltour R, Brouers F, Teyssie P, “Design of electrical conductive composites: key role of the morphology on the electrical properties of carbon black filled polymer blends”, Macromolecules 28, 1559–66 (1995).

Gubbels F, Jerome R, Vanlathem E, Deltour R, Blacher S, Brouers F, “Kinetic and thermodynamic control of the selective localization of carbon black at the interface of immiscible polymer blends”, Chem. Mater. 10, 1227–1235 (1998).

Halls JJM, Walsh CA, Greenham NC, Marseglia EA, Friend RH, Moratti SC, Holmes AB, “Efficient photodiodes from interpenetrating polymer networks”, Nature 376**,** 498–500 (1995).

Hamzehlou S and Katbab A, “Bottle-to-bottle recycling of PET via nanostructure formation by melt intercalation in twin screw compounder: Improved thermal, barrier, and microbiological properties”, J. Appl. Polym. Sci. 106, 1375–1382 (2007).

Hanemann T, “Nanoparticle surface polarity influence on the flow behavior of polymer matrix composites”, Polym. Compos. 34, 1425–1432 (2013).

Härth M and Schubert DW, “Simple approach for spreading dynamics of polymeric fluids”, Macromol. Chem. Phys. 213, 654–665 (2012).

Heriot SY and Jones RAL, “An interfacial instability in a transient wetting layer leads to lateral phase separation in thin spin-cast polymer-blend films”, Nat. Mater. 4, 782–786 (2005).

Hernández RM, Orive G, Murua A, Pedraz JL, “Microcapsules and microcarriers for in situ cell delivery”, Adv. Drug Deliver. Rev., 62, 711–730 (2010).

Hong JS, Namkung H, Ahn KH, Lee SJ, Kim C, “The role of organically modified layered silicate in the breakup and coalescence of droplets in PBT/PE blends”, Polymer 47, 3967–3975 (2006).

Hou WM, Zhou JJ, Gan ZH, Shi AC, Chan CM, Li L, “The crystallization morphology and melting behavior of polymer crystals in nano-sized domains”, Polymer 48, 4926–4931 (2007).

Huo H, Guo C, Zhou J, Zhao X, “The combination of fluctuation-assisted crystallization and interface-assisted crystallization in a crystalline/crystalline blend of poly(ethylene oxide) and poly(ε-caprolactone)”, Colloid. Polym. Sci. 292, 971–983 (2014).

Huitric J, Ville J, Mederic P, Moan M, Aubry T, “Rheological, morphological and structural properties of PE/PA/nanoclay ternary blends: effect of clay weight fraction”, J. Rheol. 53, 1101–1119 (2009).

Hwang TY, Yoo Y, Lee JW, “Electrical conductivity, phase behavior, and rheology of polypropylene/polystyrene blends with multiwalled carbon nanotube”, Rheol. Acta 51, 623–636 (2012).

Israelachvili J, “Intermolecular and Surface Forces”, 2nd edition, Academic Press, London (1991).

Jones RAL, “Polymer interfaces and the molecular basis of adhesion”, Curr. Opin. Solid State Mater. Sci. 2, 673–677 (1997).

Jordhamo GM, Manson JA, Sperling LH, “Phase continuity and inversion in polymer blends and simultaneous interpenetrating networks”, Polym. Eng. Sci. 26, 517–524 (1986).

Kamal MR, Calderon JU, Lennox BR, “Surface energy of modified nanoclays and its effect on polymer/clay nanocomposites”, J. Adhes. Sci. Technol. 23, 663–688 (2009).

Kajiya T, Nishitami E, Yamaue T, Doi M, “Piling-to-buckling transition in the drying process of polymer solution drop on substrate having a large contact angle”, Phys. Rev. E 73, 011601 (2006).

Kazarian SG, “Polymer processing with supercritical fluids”, Polym. Sci. C 42, 78–101 (2000).

Kelnar I, Kotek J, Kapralkova L, Hromadkova J, Kratochvil J, “Effect of elastomer type and functionality on the behavior of toughened polyamide nanocomposites”, J. Appl. Polym. Sci. 100, 1571–1576 (2006).

Kelnar I, Khunova V, Kotek J, Kapralkova L, “Effect of clay treatment on structure and mechanical behavior of elastomer-containing polyamide 6 nanocomposite”, Polymer 48, 5332–5339 (2007).

Kerboua N, Cinausero N, Sadoun T, Lopez-Cuesta J, “Effect of organoclay in an immiscible poly (ethylene terephthalate) waste/poly (methyl methacrylate) blend”, J. Appl. Polym. Sci. 117, 129–137 (2010).

Khatua BB, Lee DJ, Kim HY, Kim JK, “Effect of organoclay platelets on morphology of nylon-6 and poly(ethylene-ran-propylene) rubber blends”, Macromolecules 37, 2454–2459 (2004).

Kim, BJ, Bang J, Hawker CJ, Kramer EJ, “Effect of areal chain density on the location of polymer-modified gold nanoparticles in a block copolymer template”, Macromolecules 39, 4108–4114 (2006).

Kim JS, Ho PKH, Murphy CE, Friend RH, “Phase separation in polyfluorene-based conjugated polymer blends: Lateral and vertical analysis of blend spin-cast thin films”, Macromolecules 37, 2861–2871 (2004).

Kim DH, Fasulo PD, Rodgers WR, Paul DR, “Effect of the ratio of maleated polypropylene to organoclay on the structure and properties of TPO-based nanocomposites. Part I. Morphology and mechanical properties”, Polymer 48, 5960-5978 (2007).

Kim H and Macosko CW, “Processing-property relationships of polycarbonate/ graphene composites”, Polymer 50, 3797–3809 (2009).

Koerner H, Price G, Pearce NA, Alexander M, Vaia RA, “Remotely actuated polymer nanocomposites - Stress-recovery of carbon-nanotube-filled thermoplastic elastomers”, Nature Mater. 3, 115–120 (2004).

Le Corroller P and Favis BD, “Droplet-in-droplet polymer blend microstructures: a potential route toward the recycling of co-mingled plastics”,Macromol. Chem. Phys. 213, 2062–2074 (2012).

Lee M, Tzoganakis C, Park CB, “Effect of supercritical CO_2 on the viscosity and morphology of polymer blending” Adv. Polym. Tech. 19, 300–311 (2000).

Lee MN, Chan HK, Mohraz A, “Characteristics of Pickering emulsion gels formed by droplet bridging”, Langmuir 28, 3085–3091 (2012).

Li Y, Wei GX, Sue HJ, “Morphology and toughening mechanisms in clay-modified styrene-butadiene-styrene rubber-toughened polypropylene”, J. Mater. Sci. 37, 2447–2459 (2002).

Li L, Miesch C, Sudeep PK, Balasz AC, Emrick T, Russell TP, Hayward RC, “Kinetically trapped co-continuous morphologies through intraphase gelation of nanoparticles”, Nano Lett. 11, 1997–2003 (2011).

Liu T, Ozisik R, Siegel RW, “Phase separation and surface morphology of spin-coated films of polyetherimide/polycaprolactone immiscible polymer blends”, Thin Solid Films 515, 2965–2973 (2007).

Luna-Bárcenas G, Kanakia SK, Sanchez IC, Johnston KP, “Semicrystalline microfibrils and hollow fibers by precipitation with a compressed-fluid antisolvent”, Polymer 36, 3173–3182 (1995).

Luzuriaga SE, Kovarova J and Fortelny I, “Stability of model recycled mixed plastic waste compatibilised with a cooperative compatibilisation system”, Polym. Degrad. Stabil. 96, 751–755 (2011).

Lv X, Bala H, Li M, Ma X, Ma S, Gao Y, Tang L, Zhao J, Guo Y, Zhao X, Wang Z, “In situ synthesis of nanolamellas of hydrophobic magnesium hydroxide”, Colloid. Surface. A 296, 97–103 (2007).

Lyons JG, Blackie P, Higginbotham CL, “The significance of variation in extrusion speeds and temperatures on a PEO/PCL blend based matrix for oral drug delivery”, Int. J. Pharm. 351, 201–208 (2008).

Ma W, Zhang J, Wang X, “Effect of initial polymer concentration on the crystallization of poly(vinylidene fluoride)/poly (methyl methacrylate) blend from solution casting”, J. Macromol. Sci. Phys. 47, 139–149 (2008).

Manias E., “Nanocomposites: stiffer by design”, Nature Mater. 6, 9–11 (2007).

Martín A, Mattea F, Gutiérrez L, Miguel F, Cocero MJ, “Co-precipitation of carotenoids and bio-polymers with the supercritical anti-solvent process”, J. Supercrit. Fluid. 41, 138–147 (2007).

Martin JD and Velankar SS, “Effects of compatibilizer on immiscible polymer blends near phaseinversion”, J. Rheol. 51, 669–692 (2007).

Martinelli E, Galli G, Cwikel D, Marmur A, “Wettability and surface tension of amphiphilic polymer films: time-dependent measurements of the most stable contact angle”, Macromol. Chem. Phys. 213, 1448–1456 (2012).

Massa MV, Dalnoki-Veress K, Forrest JA, “Crystallization kinetics and crystal morphology in thin poly(ethylene oxide) films, Eur. Phys. J. E 11, 191–198 (2003).

Miles IS and Zurek A, “Preparation, structure, and properties of two-phase co-continuous polymer blends”, Polym. Eng. Sci. 28, 796–805 (1988).

Minelli C, Geissbuehler I, Eckert R, Vogel H, Heinzelmann H, Liley M, “Organization of nanoscale objects via polymer demixing”, Colloid. Polym. Sci. 282, 1274–1278 (2004).

Minelli C, Frommen C, Hinderling C, Pugin R, Heinzelmann H, Liley M, “The influence of nanoparticle fillers on the morphology of a spin-cast thin film polymer blend”, Colloid. Polym. Sci. 284, 482–488 (2006).

Mokarian-Tabari P, Geoghegan M, Howse JR, Heriot SY, Thompson RL, Jones RAL, “Quantitative evaluation of evaporation rate during spin-coating of polymer blend films: control of film structure through defined-atmosphere solvent-casting”, Eur. Phys. J. E 33, 283–289 (2010).

Moons E, “Conjugated polymer blends: linking film morphology to performance of light emitting diodes and photodiodes”, J. Phys. C 14, 12235–12260 (2002).

Morteani AC, Dhoot AS, Kim JS, Silva C, Greenham NC, Murphy C, Moons E, Ciná S, Burroughes JH, Friend RH, "Barrier-free electron-hole capture in polymer blend heterojunction light-emitting diodes", Adv. Mater. 15, 1708–1712 (2003).

Mudgal S, Lyons L, Bain J, Dias D, Faninger T, Johansson L, Dolley P, Shields L, Bowyer C, "Plastic waste in the environment – Final Report*"* (2011).

Murakami R and Bismarck A, "Particle-stabilized materials: dry oils and (polymerized) non-aqueous foams", Adv. Funct. Mater. 20, 732–737 (2010).

Nagarkar SP and Velankar SS, "Morphology and rheology of ternary fluid-fluid-solid systems", Soft Matter 8, 8464–8477 (2012).

Nalawade SP, Picchioni F, Jansen LPBM, "Supercritical carbon dioxide as a green solvent for processing polymer melts: Processing aspects and applications" Prog. Polym. Sci. 31, 19–43 (2006).

Narula GK and Pillai PKC, "Effect of substrate on the crystallization of polyvinylidene fluoride/poly(methyl methacrylate) polyblend from solution", J. Mater. Sci. Lett. 9, 130–132 (1990).

Neogi P, "Contact line instability in spontaneous spreading of a drop on a solid surface", J. Fluid Mech. 428, 171–183 (2001).

Nieh SY, Ybarra RM, Neogi P, "Wetting kinetics of polymer solutions. Experimental observations", Macromolecules 29, 320–325 (1996).

Nuzzo A, Coiai S, Carroccio SC, Dintcheva NTz, Gambarotti C, Filippone G, "Heat-resistant fully bio-based nanocomposite blends based on poly(lactic acid)", Macromol. Mater. Eng., 299, 31–40 (2014a).

Nuzzo A, Bilotti E, Peijs T, Acierno D, Filippone G, "Nanoparticle-induced co-continuity in immiscible polymer blends e A comparative study on bio-based PLA-PA11 blends filled with organoclay, sepiolite, and carbon nanotubes", Polymer 55, 4908–4919 (2014b).

Okuzono T, Kobayashi M, Doi M, "Final shape of a drying thin film", Phys. Rev. E 80, 021603 (2009).

Oldroyd JG, "The elasic and viscous properties of emulsion and suspensions", Proc. Roy. Soc. Lond. Ser. A 218, 122–132 (1953).

Owens DK and Wendt RC, "Estimation of the surface free energy of polymers", J. Appl. Polym. Sci. 13, 1741–1747 (1969).

Pack S, Si M, Koo J, Sokolov JC, Koga T, Kashiwagi T, Rafailovich MH, “Mode-of-action of self-extinguishing polymer blends containing organoclays”, Polym. Degrad. Stab. 94, 306–326 (2009).

Palierne JF, “Linear rheology of viscoelastic emulsions with interfacial tension”, Rheol. Acta 29, 204–214 (1990).

Park SJ, Kim KS and Kim SH, “Effect of poly(ethylene oxide) on the release behaviors of poly(ε-caprolactone) microcapsules containing erythromycin”, Colloids Surf. B, 43, 238–244 (2005).

Payne AR, “Reinforcement of elastomers”, Interscience, New York (1965).

Pawar AB, Caggioni M, Ergun R, Hartel RW, Spicer PT, “Arrested coalescence in Pickering emulsions”, Soft Matter 7, 7710–7716 (2011).

Pawar AB, Caggioni M, Hartel RW, Spicer PT, “Arrested coalescence of viscoelastic droplets with internal microstructure”, Faraday Discuss. 158, 341–350 (2012).

Peumans P, Uchida S, Forrest SR, “Efficient bulk heterojunction photovoltaic cells using small-molecular-weight organic thin films”, Nature 425, 158–162 (2003).

Picard E, Gauthier H, Gérard JF, Espuche E, “Influence of the intercalated cations on the surface energy of montmorillonites: Consequences for the morphology and gas barrier properties of polyethylene/montmorillonites nanocomposites”, J. Colloid Interface Sci. 307, 364–376 (2007).

Pickering SU, “Emulsions”, J. Chem. Soc. Abstr. 91–92, 2001–2021 (1908).

Pötschke P and Paul DR, “Formation of co-continuous structures in melt-mixed immiscible polymer blends”, J. Macromol. Sci. Part C Polym. Rev. 43, 87–141 (2003).

Poulard C and Damman P, “Control of spreading and drying of a polymer solution from Marangoni flows”, Europhys. Lett. 80, 64001 (2007).

Qiu Z, Ikehara T and Nishi T, “Miscibility and crystallization of poly(ethylene oxide) and poly(ε-caprolactone) blends”, Polymer 44, 3101-3106 (2003).

Ramanathan M and Darling SB, “Mesoscale morphologies in polymer thin films”, Prog. Polym. Sci. 36, 793–812 (2011).

Ramsden W, “Separation of solids in the surface-layers of solutions and ‘suspensions’ (observations on surface-membranes, bubbles, emulsions, and mechanical coagulation)”, Proc. R. Soc. London A 72, 156–164 (1903).

Randolph TW, Randolph AD, Mebes M, Yeung S, “Sub-micrometer sized biodegradable particles of poly(L-lactic acid) via the gas antisolvent spray precipitation process”, Biotechnol. Progr. 9, 429–435 (1993).

Ray SS, Okamoto K, Okamoto M, “Structure-property relationship in biodegradable poly (butylene succinate)/layered silicate nanocomposites”, Macromolecules 36, 2355–2367 (2003).

Reverchon E, “Supercritical antisolvent precipitation of micro- and nano-particles”, J. Supercrit. Fluid. 15, 1–21 (1999).

Reverchon E, Della Porta G, De Rosa I, Subra P, Letorneur D, “Supercritical antisolvent micronization of some biopolymers”, J. Supercrit. Fluid. 18, 239–245 (2000).

Romeo G, Filippone G, Russo P, Acierno D, “Effects of particle dimension and matrix viscosity on the colloidal aggregation in weakly interacting polymer-nanoparticle composites: a linear viscoelastic analysis”, Polym. Bull. 63, 883–895 (2009).

Sacha GA, Schmitt WJ, Nail SL, “Identification of physical-chemical variables affecting particle size following precipitation using a supercritical fluid”, Pharm. dev. technol. 11, 195–205 (2006).

Salerno A, Oliviero M, Di Maio E, Netti PA, Rofani C, Colosimo A, Guida V, Dallapiccola B, Palma P, Procaccini E, Berardi AC, Velardi F, Teti A, Iannace S, “Design of novel three-phase PCL/TZ–HA biomaterials for use in bone regeneration applications”, J. Mater. Sci.-Mater. M., 21, 2569–2581 (2010).

Salerno A, Clerici U, Domingo C, “Solid-state foaming of biodegradable polyesters by means of supercritical CO_2/ethyl lactate mixtures: Towards designing advanced materials by means of sustainable processes”, Eur. Polym. J. 51, 1–11 (2014).

Salerno A, Zeppetelli S, Di Maio E, Iannace S, Netti PA, “Architecture and properties of bi-modal porous scaffolds for bone regeneration prepared via supercritical CO2 foaming and porogen leaching combined process”, J. Supercrit. Fluid. 67 114–122 (2012).

Saritha S, Neogi P, Wang JC, “Wetting by polymer solutions”, Polymer 47, 6263–6266 (2006).

Shieh YT, Yang HS, “Morphological changes of polycaprolactone with high-pressure CO_2 treatment”, J. Supercrit. Fluid. 33, 183–192 (2005).

Shih WH, Shih WY, Kim SI, Liu J, Aksay IA, “Scaling behavior of the elastic properties of colloidal gels”, Phys. Rev. A 42, 4772–4779 (1990).

Si M, Araki T, Ade H, Kilcoyne ALD, Fisher R, Sokolov JC, Rafailovich MH, “Compatibilizing bulk polymer blends by using organoclays,” Macromolecules 39, 4793–4801 (2006).

Simon D, Holland A, Shanks R, “Poly(caprolactone) thin film preparation, morphology, and surface texture”, J. Appl. Polym. Sci. 103, 1287–1294 (2007).

Snaith HJ and Friend RH, “Morphological dependence of charge generation and transport in blended polyfluorene photovoltaic devices”, Thin Solid Films 451, 567–571 (2004).

Stauffer D and Aharony A, “Introduction to Percolation Theory”, 2nd edition, Taylor & Francis, London (1992).

Steinmann S, Gronski W, Friedrich C, “Influence of selective filling on rheological properties and phase inversion of two-phase polymer blends”, Polymer 43, 4467–4477 (2002).

Stratford K, Adhikari R, Pagonabarraga I, Desplat JC, Cates ME, “Colloidal jamming at interfaces: a route to fluid-bicontinuous gels”, Science 309, 2198–2201 (2005).

Strawhecker KE, Kumar SK, Douglas JF, Karim A, “The critical role of solvent evaporation on the roughness of spin-cast polymer films”, Macromolecules 24, 4669–4672 (2001).

Sumita M, Sakata K, Asai S, Miyasaka K, Nakagawa H, “Dispersion of fillers and the electrical conductivity of polymer blends filled with carbon black”, Polym. Test. 25, 265–271 (1991).

Sumita M, Sakata K, Hayakawa Y, Asai S, Miyasaka K, Tanemura M, “Double percolation effect on the electrical conductivity of conductive particles filled polymer blends” Colloid. Polym. Sci. 270, 134–139 (1992).

Sundararaj U and Macosko CW, “Drop breakup and coalescence in polymer blends: The effects of concentration and compatibilization”, Macromolecules 28, 2647–2657 (1995).

Taguet A, Cassagnau P, Lopez-Cuesta JM, “Structuration, selective dispersion and compatibilizing effect of (nano)fillers in polymer blends”, Prog. Polym. Sci. 39, 1526–1563 (2014).

Tang ZG, Black RA, Curran JM, Hunt JA, Rhodes NP, Williams DF, “Surface properties and biocompatibility of solvent-cast poly(ε-caprolactone) films”, Biomaterials 25, 4741–4748 (2004).

Taylor GI, “The viscosity of a fluid containing small drops of another fluid”, Proc. Roy. Soc. Lond. A Mat. 138, 41–48 (1932).

Thareja P and Velankar S, “Particle-induced bridging in immiscible polymer blends”, Rheol. Acta 46, 405–412 (2007).

Thareja P. and Velankar S, “Rheology of immiscible blends with particle-induced drop clusters”, Rheol. Acta 47, 189–200 (2008).

Thareja P, Ising BP, Kingston SJ, Velankar SS, “Polymer foams stabilized by particles adsorbed at the air/polymer interface”, Macromol. Rapid Comm. 29, 1329–1334 (2008).

Thareja P, Moritz K, Velankar SS, “Interfacially active particles in droplet/matrix blends of model immiscible homopolymers: Particles can increase or decrease drop size”, Rheol. Acta 49, 285–298 (2010).

Tsivintzelis I, Pavlidou E, Panayiotou C, “Porous scaffolds prepared by phase inversion using supercritical CO_2 as antisolvent: I. Poly(l-lactic acid)”, J. Supercrit. Fluid. 40, 317–322 (2007).

Tucker III CL and Moldenaers P, “Microstructural evolution in polymer blends”, Annu. Rev. Fluid Mech. 34, 177–210 (2002).

Utracki LA and Shi ZH, “Development of polymer blend morphology during compounding in a twin-screw extruder. Part I: Droplet dispersion and coalescence - a review,” Polym. Eng. Sci. 32, 1824–1833 (1992).

Vacatello M, “Monte Carlo simulations of polymer melts filled with solid nanoparticles”, Macromolecules 34, 1946–1952 (2001).

Vandebril S, Vermant J, Moldenaers P, “Efficiently suppressing coalescence in polymer blends using nanoparticles: role of interfacial rheology”, Soft Matter 6, 3353–3362 (2010).

Van Hemelrijck E, Van Puyvelde P, Velankar S, Macosko CW, Moldenaers P, “Interfacial elasticity and coalescence suppression in compatibilized polymer blends”, J. Rheol. 48, 143–158 (2004).

Van Puyvelde P, Velankar S, Moldenaers P, “Rheology and morphology of compatibilized polymer blends,” Curr. Opin. Colloid In. 6, 457–463 (2001).

Vermant J, Ceccia S, Dolgovskij MK, Maffettone PL, Macosko CW, “Quantifying dispersion of layered nanocomposites via melt rheology”. J. Rheol. 51, 429–450 (2007).

Vermant J, Cioccolo G, Golapan Nair K, Moldenaers P, “Coalescence suppression in model immiscible polymer blends by nano-sized colloidal particles”, Rheol. Acta 43, 529–538 (2004).

Vermant J, Vandebril S, Dewitte C, Moldenaers P, “Particle-stabilized polymer blends”, Rheol. Acta 47, 835–839 (2008).

Walheim S, Böltau M, Mlynek G, Krausch G, Steiner U, “Structure formation via polymer demixing in spin-cast films”, Macromolecules 30, 4995-5003 (1997).

Walheim S, Ramstein M, Steiner U, “Morphologies in ternary polymer blends after spin-coating”, Langmuir 15, 4828–4836 (1999).

Walker TA, Frankowski DJ, Spontak RJ, “Thermodynamics and kinetic processes of polymer blends and block copolymers in the presence of pressurized carbon dioxide”, Adv. Mater. 20, 879–898 (2008).

Wang M and Pan N, “Predictions of effective physical properties of complex multiphase materials”, Mater. Sci. Eng. R 63, 1–30 (2008).

Washburn NR, Simon CG, Tona A, Elgendy HM, Karim A, Amis EJ, J. Biomed. Mater. Res. 60, 20–29 (2002).

Willemse RC, Postuma de Boer A, Van Dam J, Gotsis AD, “Co-continuous morphologies in polymer blends: a new model”, Polymer 39, 5879–5887 (1998).

Willemse RC, Ramaker EJJ, Van Dam J, Postuma de Boer A, “Coarsening in molten quiescent polymer blends: the role of the initial morphology”, Polym. Eng. Sci. 39, 1717–1725 (1999).

Wu D, Lin D, Zhang J, Zhou W, Zhang M, Zhang Y, Wang D, Lin B, “Selective localization of nanofillers: effect on morphology and crystallization of PLA/PCL blends”, Macromol. Chem. Phys. 212, 613–626 (2011).

Wu G, Li B, Jiang J, “Carbon black self-networking induced co-continuity of immiscible polymer blends”, Polymer 51, 2077–2083 (2010a).

Wu G, Cai X, Lin X, Yui H, “Heterogeneous distribution of magnetic nanoparticles in reactive polymer blends”; React. Funct. Polym. 70, 732–737 (2010b).

Wu H and Morbidelli M, “A model relating structure of colloidal gels to their elastic properties”, Langmuir 17, 1030–1036 (2001).

Wu K and Li J, “Precipitation of a biodegradable polymer using compressed carbon dioxide as antisolvent”, J. Supercrit. Fluid. 46, 211–216 (2008).

Wu S, “Formation of dispersed phase in incompatible polymer blends: Interfacial and rheological effects”, Polym. Eng. Sci. 27, 335–343 (1987).

Xiang F, Shi Y, Li X, Huang T, Chen C, Peng Y, Wang Y, “Cocontinuous morphology of immiscible high density polyethylene/polyamide 6 blend induced by multiwalled carbon nanotubes network”, Eur. Polym. J. 48, 350–361 (2012).

Xue L, Zhang J, Han Y, “Phase separation induced ordered patterns in thin polymer blend films”, Prog. Polym. Sci., 37, 564–594 (2012).

Yeo S and Kiran E, “Formation of polymer particles with supercritical fluids: A review”, J. Supercrit Fluid. 34, 287–308 (2005).

Yilgor I, Bilgin S, Isik M, Yilgor E, “Facile preparation of superhydrophobic polymer surfaces”, Polymer 53, 1180–1188 (2012).

Yoganathan RB, Mammuccari R, Foster NR, “Dense gas processing of polymers”, Polym. Rev. 50, 144–177 (2010).

Young TH, Huang JH, Chuang WY, “Effect of evaporation temperature on the formation of particulate membranes from crystalline polymers by dry-cast process”, Eur. Polym. J. 38, 63–72 (2002).

Zanetti M, Kashiwagi T, Falqui L, Camino G, “Cone calorimeter combustion and gasification studies of polymer layered silicate nanocomposites”, Chem. Mater. 14, 881–887 (2002).

Zare Y, “Recent progress on preparation and properties of nanocomposites from recycled polymers: A review”, Waste Manage. 33, 598–604 (2013).

Zhang Q, Yang H, Fu Q, “Kinetics-controlled compatibilization of immiscible polypropylene/polystyrene blends using nano-SiO_2 particles”, Polymer 45, 1913–1922 (2004).

Zhou P, Yu W, Zhou C, Liu F, Hou L, Wang J, “Morphology and electrical properties of carbon black filled LLDPE/EMA composites”, J. Appl. Polym. Sci. 103, 497–502 (2007).

Zonder L, Ophir A, Kenig S, McCarthy S, “The effect of carbon nanotubes on the rheology and electrical resistivity of polyamide 12/high density polyethylene blends”, Polymer 52, 5085–5091 (2011).